Experimental study of active and passive blade pitch control strategies for axial-flow marine current turbines

Katherine D. Van Ness

A dissertation
submitted in partial fulfillment of the
requirements for the degree of

Doctor of Philosophy

University of Washington

2022

Reading Committee:

Brian Polagye, Chair

Alberto Aliseda, Chair

Michael Motley

Program Authorized to Offer Degree:
Mechanical Engineering

University of Washington

Abstract

Experimental study of active and passive blade pitch control strategies for axial-flow marine current turbines

Katherine D. Van Ness

Co-Chairs of the Supervisory Committee:
Brian Polagye
Mechanical Engineering

Alberto Aliseda
Mechanical Engineering

Cost and reliability remain among the main barriers limiting widespread adoption of riverine, estuarine, or ocean current turbine power generation. In particular, structural loads are significantly greater than for wind turbines with equivalent power output, which contributes to higher costs. Compounded with uncertainties about hydrodynamic loads, this can contribute to structural failure or excessive and expensive safety factors. Consequently, control strategies to mitigate structural loads and reduce cost are of considerable importance.

Load reduction is of particular interest when currents exceed a certain threshold (i.e., the turbine-specific “rated speed”), and a control strategy is implemented to maintain a constant power output. Most fixed-pitch turbines will use a speed control strategy, increasing or decreasing the rotation rate to achieve the efficiency required for power regulation. However, these “overspeed” and “underspeed” control strategies correspond to large increases in thrust or torque, respectively, that require overdesigning the turbine blades or generator. Blade pitch control circumvents this trade-off, as decreased angles of attack simultaneously reduce thrust and torque. This does, however, require actuators to change blade pitch. While active pitch control is the conventional standard for wind turbines in these above-rated conditions, similar variable blade pitch mechanisms have not yet been uniformly adopted by marine

current technology developers due to the higher cost of inspection, maintenance, and repairs relative to wind turbines. For this reason, passive adaptive blade pitch control, in which blades are designed to elastically deform under load without an actuator, sensor, or control logic, is conceptually attractive. Improved understanding of the loading associated with both speed and pitch control strategies is critical to optimizing a design for minimal cost and maximal reliability. Therefore, the overarching goal of this work is to experimentally investigate active and passive pitch control methods, characterize their potential for load reduction, and establish appropriate scaling relations for passive adaptive blades. The three underlying objectives supporting this goal are outlined below.

The first objective is to demonstrate active blade pitch control in above-rated flow conditions and compare the measured turbine loads to those observed with overspeed and underspeed control in order to develop our understanding of the trade-offs associated with each. To this end, we experimentally characterized power performance and turbine loading over a range of blade pitch settings and tip-speed ratios for a three-bladed axial-flow turbine. We then implemented a control strategy to maintain power output in time-varying currents using blade pitch control and compared the turbine performance under this control strategy to overspeed and underspeed control strategies for a fixed pitch turbine. The experiments were conducted with a laboratory-scale 0.45-m diameter turbine in an open channel flume with a 35% blockage ratio. During pitch characterization experiments, inflow velocity was maintained at 0.8 m/s with 4% turbulence intensity. During time-varying inflow experiments, currents varied from 0.7-0.8 m/s over a 20-minute period, while a proportional controller regulated either blade pitch or rotor speed, and we recorded turbine power output and turbine loads. In this velocity range, where turbine performance is independent of Reynolds number, we demonstrate that pitch control substantially reduces torque requirements relative to underspeed control and streamwise turbine loads relative to overspeed control. Additional tests were conducted for underspeed control and pitch control in a

Reynolds-dependent regime with time-varying inflow between 0.4-0.5 m/s and 0.5-0.6 m/s. These cases suggest that blade pitch control could provide even greater benefits relative to speed control in small-scale applications.

The second objective is to develop our understanding of passive adaptive blade fabrication and the effect of fiber orientation to inform a passive pitch control design. By tailoring the ply angle in a unidirectional carbon fiber blade, a desired twist can be induced in response to bending of the blade under load. In developing this form of passive adaptive control, a fundamental question is how to non-dimensionalize the fluid-structure interaction to make laboratory-scale experiments relevant to full-scale applications. To address these questions, we first conducted an experimental investigation into the effect of fiber angle on blade performance and blade deformation during turbine operation. The composite blades were fabricated with 0°, 2.5°, 5°, and 10° fiber orientations, where a positive fiber orientation results in a reduced angle of attack as load increases (i.e., a "pitch-to-feather" control strategy). Blades were tested in a recirculating flume at 0.7 m/s ($Re_c = 5.3 \cdot 10^4 - 2.0 \cdot 10^5$) while measuring force and torque on the rotor. Simultaneously, a high-speed camera observed *in-situ* deflection and twist at the blade tip. Results show a greater reduction in C_P and C_T for blades with larger fiber orientations relative to the neutral blade set, while even small fiber orientations were observed to limit thrust at high tip-speed ratios. To explore the correct non-dimensional scaling for this physical process, we performed a set of Cauchy-scaled experiments using blades with identical bend-twist couplings but different bending stiffness. These results demonstrate that the Cauchy number is a meaningful parameter for scaling passive adaptive current turbine blades and to model steady-state hydrodynamic and hydroelastic behavior.

The third and final objective is to implement passive pitch control to develop our understanding of the trade-offs between speed, active pitch, and passive pitch control methods. Two passive blade pitch control strategies for the same lab-scale turbine were developed and tested experimentally in a recirculating flume. The goal of the control is to regulate mechanical power, while minimizing rotor loads, when flow conditions exceed the rated condition. Both strategies used the 5° fiber blade set from the aforementioned study. One control strategy combined passive adaptive blades with overspeed control (actuating rotational speed above the tip-speed ratio corresponding to peak efficiency) while the other combined passive adaptive blades with active pitch control (actuating blade pitch using motors at the blade root). Both strategies were implemented in linearly increasing inflow from 0.7 m/s to 0.8 m/s and compared to control strategies using rigid, aluminum blades under the same flow conditions. The passive adaptive blades combined with active pitch control show no improvement in steady-state load reductions relative to rigid blades used with active pitch control. However, the passive adaptive blades combined with overspeed control show reduced torque and only a 12% increase in thrust relative to the rated flow condition. This indicates that passive adaptive blades combined with overspeed control can be an effective strategy in currents above the rated flow speed, removing the need for an active pitch mechanism in some applications. In addition to measuring turbine loads, deflection and twist of the passive adaptive blades during experimental testing were observed using a high-speed camera to support our understanding of the bend-twist behavior during turbine operation over a range of flow speeds, rotation rates, and preset pitch angles.

Overall, active and passive pitch control strategies for Region III are shown to offer significant load reductions in thrust and torque relative to rigid blade speed control strategies. While controller selection is discussed primarily relative to their associated loads, we discuss additional considerations including blade design, channel blockage, range and frequency of flow variation, and Reynolds-number. These discussions underline the value of future investigations into active and passive pitch control for smoothing high-frequency loads and scaling between lab- and full-scale passive adaptive rotors, among other work.

TABLE OF CONTENTS

Page

List of Figures . . . iv

List of Tables . . . ix

Chapter 1: Introduction . . . 1
- 1.1 Turbine Control Regions . . . 1
- 1.2 Active Pitch Control . . . 4
- 1.3 Passive Pitch Control . . . 4
- 1.4 Dissertation Objectives . . . 8

Chapter 2: Methods . . . 10
- 2.1 Turbine Instrumentation . . . 10
- 2.2 Experimental Facility . . . 11
- 2.3 Performance Characterization . . . 13

Chapter 3: Active Blade Pitch Control . . . 16
- 3.1 Methods . . . 16
  - 3.1.1 Pitch Characterization . . . 16
  - 3.1.2 Region III Control: Reynolds-number Independent Conditions . . . 18
  - 3.1.3 Region III Control: Reynolds-number Dependent Conditions . . . 22
- 3.2 Results . . . 23
  - 3.2.1 Characteristic Turbine Performance . . . 23
  - 3.2.2 Region III Control: Reynolds-number Independent Regime . . . 23
  - 3.2.3 Region III Control: Reynolds-number Dependent Regime . . . 27
- 3.3 Discussion . . . 28
  - 3.3.1 Reynolds Number Effects . . . 28
  - 3.3.2 Blockage Effects . . . 31

3.3.3 Turbulence Effects 33
3.4 Conclusion 33

Chapter 4: Passive Adaptive Blade Characterization & Cauchy-Scaling 35
4.1 Non-dimensional Scaling Laws 35
4.2 Methods 37
4.2.1 Blade Fabrication 37
4.2.2 Blade Deformation 38
4.2.3 Cauchy Scaling 40
4.3 Results & Discussion 44
4.3.1 Turbine Performance and Deformation Response for Blades of Varying Fiber Orientation 44
4.3.2 Cauchy Scaling 48
4.4 Conclusion 50

Chapter 5: Passive Blade Pitch Control 53
5.1 Methods 53
5.1.1 Controllers 53
5.2 Results 55
5.2.1 Comparison of Turbine Loads Between Controllers 55
5.2.2 Comparison of Blade Deformation Between Controllers 58
5.3 Discussion 58
5.3.1 Passive Adaptive Blades with Overspeed Control 58
5.3.2 Passive Adaptive Blades with Active Pitch Control 62
5.3.3 Effects of Reynolds Number 63
5.3.4 Effects of Blockage 64
5.3.5 Blade Variability 66
5.4 Conclusion 67

Chapter 6: Conclusions & Future Work 69
6.1 Conclusions 69
6.2 Future Work 72

Appendix A: Performance contour maps 83

Appendix B: Step-by-step blade fabrication 85

Appendix C: Composite Blade Geometry 89

Appendix D: Static mechanical testing 91

Appendix E: Calculation of bending stiffness matrix and bend-twist coupling 94

Appendix F: Comparison of rigid, aluminum blades with neutral, composite blades . 96

LIST OF FIGURES

Figure Number Page

1.1 (a) Canonical power curve and (b) efficiency for a variable-speed current turbine as a function of inflow speed. Region I corresponds to inflow speeds below the cut-in required for net power generation. Region II corresponds to inflow speeds between the cut-in and rated speed. Region III corresponds to inflow speeds above the rated speed. 2

1.2 Mechanical efficiency (ratio of shaft mechanical power to kinetic power in inflow) as a function of tip-speed ratio (tangential velocity of rotor tip to inflow velocity). Underspeed, overspeed, or blade pitch control can be used for power regulation in Region III. Underspeed and overspeed control reduce efficiency by actuating rotation rate above or below the tip-speed ratio corresponding to peak efficiency, while blade pitch control reduces efficiency by effectively changing blade geometry to a design with a lower peak efficiency. Note that the tip-speed ratio changes for pitch control, but not as significantly as for overspeed or underspeed control, because the inflow velocity changes while rotation rate is held constant. 3

1.3 (a) Unidirectional, off-axis fibers result in anisotropic blade properties and (b) a coupling between flapwise deflection and spanwise twisting. 5

2.1 CAD model of turbine and instrumentation. 11

2.2 Data acquisition system block diagram for turbine instrumentation. 12

2.3 Blade and driveshaft load cell coordinate systems. 12

2.4 To account for azimuthally-varying static force and torque, (a) tare measurements were taken at 12 equally-spaced positions and (b) a spline interpolation was used to calculate dynamic loads and torques for instantaneous data. . . 15

3.1 Coefficients of (a) performance and (b) thrust as a function of tip-speed ratio, λ, for various blade pitch settings at 0.8 m/s inflow velocity. $-2°$ is the optimal pitch angle. Note that the $-2°$ performance curves describe the control space for a fixed-pitch turbine operating with speed control. 17

3.2 Blade pitch schematic showing that positive blade pitch angles correspond to blade rotation towards the feathered position (i.e., decreasing the angle of attack). Pitch is measured at the blade tip, so a blade pitch of 0° indicates that the blade chord line at the tip is parallel to the plane of rotation. 18

3.3 Proportional controller block diagram. 19

3.4 Representative time series from the ADV during oscillating inflow between 0.7 and 0.8 m/s with a 20 minute time period. Orange dashed line shows the one-minute moving average. 20

3.5 Contour lines of constant Reynolds number, $Re_c = c\sqrt{U_\infty^2 + (\omega r)^2}/\nu$, as a function of inflow velocity and tip-speed ratio. Lines of constant Re_c are in grey while each colored line corresponds to the range of Reynolds numbers for a particular combination of control strategy and range of inflow velocities. Reynolds-independence was observed above $9 \cdot 10^4$, as denoted by the dashed black line. 21

3.6 (a) C_P and (b) C_T contour maps as a function of tip-speed ratio (λ) and blade pitch (β) in 0.8 m/s flow. (c) indicates operating points where experimental data was collected. 24

3.7 Time series for (a) free stream velocity, (b) rotor speed (left axis) for speed control or blade pitch (right axis) for pitch control, (c) power output relative to the rated power (d) normalized rotor thrust, and (e) normalized rotor torque for overspeed, underspeed, and pitch control. The overspeed case is a synthetic output based on the measured free stream velocity during the pitch control case and the performance characterization from Fig. 3.1. For both under- and overspeed control, blade pitch was maintained at −2°. For pitch control, rotor speed was maintained at 3.2 rps. 26

3.8 Normalized (a) rotor thrust and (b) rotor torque using underspeed and pitch control, simulated in oscillating inflow ranges of 0.4-0.5 m/s, 0.5-0.6 m/s, and 0.7-0.8 m/s. 29

3.9 Coefficients of (a) performance and (b) thrust as a function of tip-speed ratio, λ, for the turbine in confined flow (35% blockage) and unconfined flow. The confined flow result is based on experimental measurements in 0.8 m/s flow with a pitch angle of −2°, while the unconfined flow result is estimated using a blockage correction based on the model presented by [62]. 32

4.1 Flexible, composite blades composed of a carbon fiber spar (black), to provide the desired bend-twist coupling, and a semi-rigid polyurethane outer (translucent white-grey) to provide the desired blade geometry and hydrodynamic behavior. 38

4.2 High-speed video of the rotor plane during flume testing was used to calculate tip deflection and twist by (a) identifying a high-contrast object as the blade, (b) binarizing the frame to segment the blade tip from the background, and (c) measuring the position of the centroid and orientation of the major axis in order to calculate tip deflection and twist relative to the unloaded blade. . 39

4.3 For the in-water static test, deflection and twist are determined from photographs taken in the (a) unloaded and (b) loaded states. 41

4.4 (a) Deflection and (b) twist as a function of applied load for a 7-ply and 5-ply passive adaptive blade with the same 10° fiber orientation. Similarity in (c), twist as a function of deflection, is representative of the matching bend-twist coupling between blades. 42

4.5 Coefficients of (a) performance and (b) thrust as a function of tip speed ratio in 0.7 m/s inflow for each blade set (0°, 2.5°, 5°, and 10° fiber orientation). High-speed video of the passing blades provided measurements of (c) deflection and (d) blade pitch at the tip as a function of tip speed ratio. Shaded regions in each figure represent the interquartile range of measurements. 46

4.6 Coefficients of (a) performance and (b) thrust as a function of tip speed ratio for a 7-ply and 5-ply composite blade in Cauchy-scaled flow conditions. The 7-ply blade is shown at both flow conditions to provide a reference. High-speed video of the passing blades provided measurements of (c) deflection and (d) blade pitch at the tip as a function of tip speed ratio. Shaded regions in (a,b) represent the interquartile range of measurements while the light orange and blue markers in (c,d) represent measurements from individual blade passages. 49

4.7 Coefficients of (a) performance and (b) thrust as a function of tip speed ratio for a rigid blade with the same unloaded geometry of the 5- and 7-ply composite blades. Shaded regions represent the interquartile range, which is smaller than the size of the markers in (b). 50

5.1 Coefficients of (a) performance and (b) thrust in 0.7 m/s flow for the flexible and rigid blades. The preset pitch angles of both blades sets were adjusted to achieve matching peaks in efficiency and power output. Pitch angle, β is given relative to the plane of rotation. 55

5.2 Four control strategies were implemented in linearly increasing inflow from the rated speed of 0.7 m/s to 0.8 m/s over 10 minutes. Shown for each controller is the time series of (a) free-stream velocity, U_∞, (b) change in tip-speed ratio from the tip-speed ratio corresponding to peak efficiency, $\Delta\lambda$, (c,d) change in blade pitch or rotation rate depending on whether active pitch or speed control is being used, (e) thrust normalized by the rated condition, and (f) torque normalized by the rated condition. The minor deviations in inflow velocity between the tests are associated with low-frequency resonance between the pumps and test section. 57

5.3 (a) Deflection and (b) twist of the composite blades observed when implementing passive adaptive blades with active pitch control and passive adaptive blades with overspeed control in linearly increasing inflow from the rated speed of 0.7 m/s to 0.8 m/s. Deflection and twist measurements from individual blade passages are plotted in light teal while the darker colored plots referenced in the legend indicate the average measurement. 59

5.4 As the overspeed controller (left) and active pitch controller (right) combined with passive adaptive blades are implemented in linearly increasing inflow from the rated speed of 0.7 m/s to 0.8 m/s, blade performance and deformation can be understood to shift between the characteristic curves corresponding to the initial and final operating conditions: (a,e) coefficient of performance, (b,f) coefficient of thrust, (c,g) tip deflection, and (d,h) tip twist as a function of tip-speed ratio. Deflection and twist measurements from individual blade passages are plotted in light blue and light teal while the darker colored plots referenced in the legend indicate the average measurement. Rigid blade performance, tested with $\beta = 4.4°$ to achieve equivalent peak performance, are shown in solid grey. Rigid blade performance is independent of velocity in the 0.7 m/s to 0.8 m/s range. 61

5.5 Blockage-corrected characteristic performance for (a) power and (b) thrust coefficients as a function of tip-speed ratio. 66

5.6 CT scans of three 0° fiber blades showing variations in spar placement within the polyurethane cast. 67

A.1 C_P (left column) and C_T (right column) contour maps as a function of tip-speed ratio (λ) and blade pitch (β) in (a,b) 0.4 m/s flow, (c,d) 0.5 m/s flow, and (e,f) 0.6 m/s flow. 84

B.1 Various steps of blade fabrication including the (a) layup of 7 plies (76mm by 178mm) of Hexcel AS4, 12K filament count carbon fiber onto a mold surface to be cured in an autoclave, (b) spar profile cut from the water jet, (c) titanium blade root adaptor to hold the carbon fiber spar, (d) spare mounted in the blade root, (e) aluminum blade mold to cast the spar in polyurethane, and (f) final composite blade consisting of a carbon fiber spar with a titanium root cast in polyurethane. The carbon fiber provides the desired bend-twist coupling while the polyurethane provides the desired blade geometry. 87

D.1 Top-view schematic of the static mechanical test, where x is the distance between the laser displacement sensors (63.5 mm) and d is the difference between the displacement measurements. The load applied by the actuator is measured by a load cell at the blade root. 92

D.2 (a) Deflection and (b) twist as a function of applied load for passive adaptive blades with 0°, 2.5°, 5°, and 10° fiber orientation. The resulting bend-twist coupling is reflected in (c) twist as a function of deflection. 93

F.1 Coefficients of (a) power and (b) thrust for the rigid, aluminum blades and neutral (0°), composite blades. 96

LIST OF TABLES

Table Number Page

2.1 Turbulence intensities calculated for inflow speeds 0.4-0.8 m/s. 14

3.1 Maximum changes in torque and thrust from the rated condition for each controller in 0.7-0.8 m/s oscillating inflow. Blade preset pitch angle is $-2°$. . 27

3.2 Maximum changes in torque and thrust from the rated condition for each controller, simulated for two oscillating inflow cases below Reynolds-independence (0.4-0.5 m/s and 0.5-0.6 m/s) and one case at Reynolds-independence (0.7-0.8 m/s). Blade present pitch angle is $+3°$. 28

4.1 Material properties for Hexcel AS4. 42

C.1 Blade geometry, where r is the local radius, R is the turbine radius, c is the local chord, and t is the local thickness. 90

ACKNOWLEDGMENTS

The work that went into this dissertation would not have been possible without the support of many people, and I am lucky and grateful to have had an incredible team of colleagues, friends, and mentors to get me here. First and foremost, I want to acknowledge my co-advisors, Brian Polagye and Alberto Aliseda. Brian has given me so many resources and opportunities to follow my passions and taught me what it means to be an effective mentor, leader, and educator. Alberto has always kept his door open to me, and I have learned so much from his trust and guidance.

I want to acknowledge my committee members, Craig Hill, Michael Motley, and Eli Livne. Their advice, resources, and questions have strengthened my research and broadened my perspective as a researcher. A special thanks to Craig Hill, who was a friend and mentor to me when I first joined UW and from whom I continue to learn and seek advice.

I want to thank Robynne Murray, my mentor at the National Renewable Energy Laboratory (NREL) for her support during my fellowship with the Oak Ridge Institute for Science and Education. She has always been available to lend an ear and offer advice during our time working together, and I have thoroughly enjoyed seeing my research through a new lens with everything I have learned from Robynne and other engineers at NREL.

The opportunity to pursue this research would be non-existent without the work of Justin Burnett and others at the UW Applied Physics Laboratory, whose design and fabrication of the lab-scale turbine used in my experiments jump-started my research career at UW. I recognize that not many graduate students have such expansive resources as those provided by APL, and Justin's continued support has been invaluable to this and upcoming project opportunities.

One of the highlights of my time at UW was having Zack Tully's support during the early stages of the passive adaptive blade research. The enthusiasm and creativity he brought to new problems breathed life into seemingly dead-end ideas. I could not have asked for a better co-collaborator during the time we worked together.

Many thanks to the Mechanical Engineering Department staff, past and present, for their technical advice on machining and composite fabrication throughout my research, including Bill Kuykendall, Michelle Hickner, Svenja Fleischer, Dzung Tran, Eamon McQuaide, and Reggie Rocamora. I also want to thank Wanwisa Kisalang , whose positivity and assurance carries our department's graduate students, including me, through many ups and downs.

My success is due, in part, to the technical support, advice, and good company of my colleagues at the Marine Renewable Energy Lab, both past and present. A special thanks to Corey Crisp for his seemingly endless knowledge on all things electrical and software-related that contributed to Harvey's data acquisition system. Working with such a collaborative team of people made the journey enjoyable and sustainable.

A huge thank you to all the students I have met and collaborated with through Mechanical Engineering Students Against Racism. Finding our shared commitment to student empowerment and breaking down oppressive structures in academia and beyond is what kept me engaged and committed to this field as a whole.

I want to also acknowledge Ramona Barber and Pavel Babuska for paving the way for the passive adaptive blade research presented in my dissertation. Additional thanks to Richard Wiebe and Miguel Gonzalez for your advice and support as I delved into this project.

Aside from the support I received throughout my PhD, I also want to acknowledge those whose guidance brought me to UW, in some way or another. Thank you, Michael Bait and Pam Thompson, who remain some of the best educators I have ever had the pleasure of learning under. Thank you, Coach Agosta, for demonstrating authentic leadership, for your holistic approach to coaching the athlete and the person, and for teaching me how to

recognize and develop my strengths. Thank you Charles Knisley, whose advice came at a pivotal time in my career. Lastly, I could not speak of former mentors without thanking Wendelin Wright. Working with her is largely what developed my desire to pursue graduate school. I will always be grateful for her support and advice through my earliest days as a researcher and through the graduate school application process.

Thank you to my family, especially my parents, Dan and Jennifer Van Ness, for supporting me in my studies, believing in me, and letting me find my own way.

Thank you to the many friends that kept me sane en route to my degree. Their companionship, food, music, and community-focused endeavors nourished and balanced me through it all. A special thanks to Bobby Azarbayejani for supporting me through some of the hardest moments and celebrating with me through the best.

This work was supported by the Department of Defense Naval Facilities Engineering Command and the Marine-Hydrokinetic Graduate Student Research Program, which was developed and funded by the Oak Ridge Institute for Science and Education and the Department of Energy. I also want to thank the Alice C. Tyler Charitable Trust for supporting the continued operation and development of the experimental facilities at the University of Washington.

Chapter 1

INTRODUCTION

Marine current energy presents many opportunities to expand access to reliable electricity for coastal communities, support off-shore ocean observation, strengthen energy security, and reduce greenhouse gas emissions. However, further technological development is needed to decrease costs and increase reliability of current turbines to make it a more viable option for power generation [1, 2]. Specifically, Walker and Thies [1] identified blade failure as the most common failure mode in tidal turbine deployments, followed by generator failure. An improved understanding of operating loads for current turbines is critical to successful turbine design and operation. Of particular interest are the maximum loads expected during turbine operation, which will vary significantly depending on the specific control strategy employed. Further research is needed to investigate trade-offs associated with these control strategies and, in turn, support marine current turbine technology evolution towards a more economic, reliable option for coastal communities.

1.1 Turbine Control Regions

In most applications, it is desirable to cap power output at a "rated" current speed to avoid the cost of sizing generation equipment for relatively infrequent currents. The rated flow condition delineates between two of the three general regions of turbine control shown in Figure 1.1. Region I corresponds to inflow speeds below cut-in speed, the minimum inflow speed required to start generating power. Consequently, no power generation occurs in Region I. Region II corresponds to inflow speeds between the cut-in speed and the rated speed, where the control objective is to maximize efficiency (ratio of mechanical shaft power to inflow kinetic power). Region III, the focus of this thesis, corresponds to inflow speeds

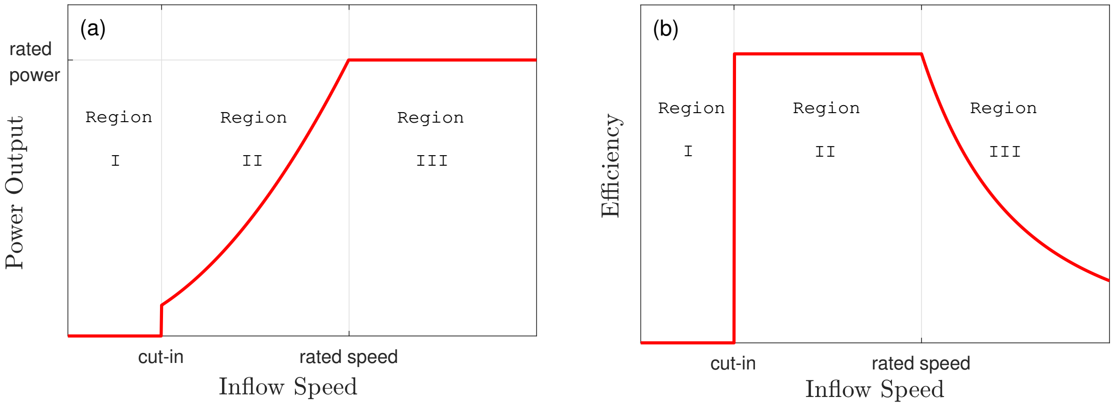

Figure 1.1: (a) Canonical power curve and (b) efficiency for a variable-speed current turbine as a function of inflow speed. Region I corresponds to inflow speeds below the cut-in required for net power generation. Region II corresponds to inflow speeds between the cut-in and rated speed. Region III corresponds to inflow speeds above the rated speed.

above the rated speed, where the control objective is to maintain a constant power output at the turbine's rated (i.e, maximum) power. In wind energy, Region IV is defined as extreme flow conditions, necessitating turbine shutdown for survivability. The relative predictability of tidal currents obviates the need for Region IV operation for tidal turbines unless wave loading is appreciable [3, 4, 5]. To meet the Region III control objective, efficiency must be precisely decreased as inflow increases, which can be achieved through changes in rotation rate, ω, or blade pitch, β, (Figs. 1.1(b), 1.2).

Variable speed control strategies are classified as "overspeed" or "underspeed" relative to the rotational speed corresponding to maximum efficiency. Overspeed control involves decreasing generator torque to increase the speed of the rotor, such that λ exceeds its optimal value. Since the thrust coefficient and number of operating cycles increases with λ, the drawback of this strategy is that it leads to high fatigue loads and higher material costs for blade manufacturing [6]. Furthermore, depending on the proximity to the water surface, there is also an increased risk of cavitation at high tip-speed ratios, as demonstrated in [7, 8,

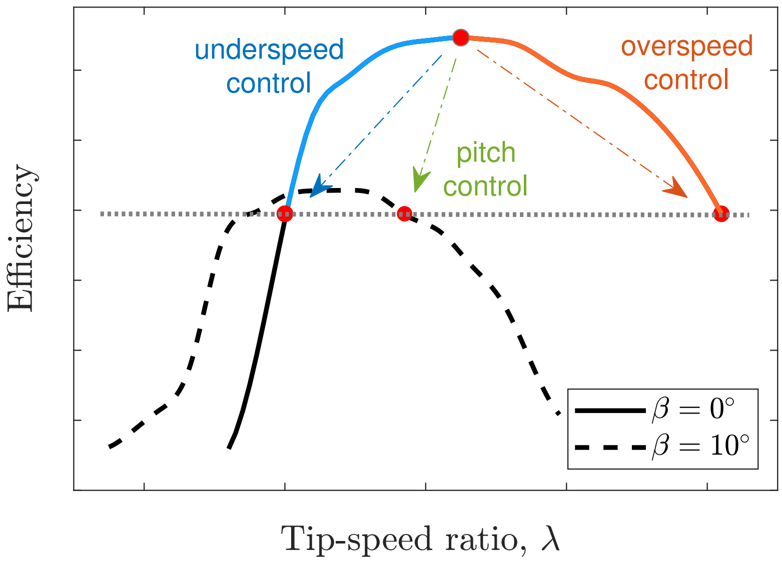

Figure 1.2: Mechanical efficiency (ratio of shaft mechanical power to kinetic power in inflow) as a function of tip-speed ratio (tangential velocity of rotor tip to inflow velocity). Underspeed, overspeed, or blade pitch control can be used for power regulation in Region III. Underspeed and overspeed control reduce efficiency by actuating rotation rate above or below the tip-speed ratio corresponding to peak efficiency, while blade pitch control reduces efficiency by effectively changing blade geometry to a design with a lower peak efficiency. Note that the tip-speed ratio changes for pitch control, but not as significantly as for overspeed or underspeed control, because the inflow velocity changes while rotation rate is held constant.

9]. Underspeed control involves increasing generator torque to decrease the speed of the rotor and bring λ below its optimal value. Lower λ corresponds to lower thrust on the turbine but requires a higher generator torque [10]. This can substantially increase the generator size and, below optimal λ, lift and drag forces can fluctuate rapidly due to blade stall [6]. Alternatively, a stall-regulated turbine uses blades tailored to progressively stall from root to tip as the inflow increases beyond the rated speed. However, this typically produces higher rates of fatigue failure from cyclic and stochastic loading [11].

1.2 Active Pitch Control

Active blade pitch control relies on changes in blade pitch to reduce C_P, which can avoid high thrust loads and generator torque [10]. However, installation of pitch actuators introduces additional modes of failure, and inspection, maintenance, and repairs are difficult and expensive for current turbines [12]. Consequently, variable blade pitch mechanisms have not been uniformly adopted by technology developers [13]. To date, blade pitch control performance for current turbines in Region III has been primarily evaluated in simulation [14, 15]. While established methods and new demonstrations of pitch control strategies for wind turbines [16, 17] can guide current turbine development, experimental studies using current turbines have been limited to fixed pitch tests for a relatively limited range of blade pitches as in [7].

1.3 Passive Pitch Control

Numerical [18, 19, 20, 21], experimental [22, 23, 24, 25, 26, 27, 28, 29], and theoretical [30] studies demonstrate the potential advantages of using flexible, passive adaptive blades for load mitigation in above-rated or unsteady flow conditions. By tailoring the off-axis orientation of the composite fibers of the blade, a passive adaptive blade can be designed with a "bend-twist coupling", such that deflection in the flapwise direction is coupled to twisting in the spanwise direction (Fig. 1.3).

Multiple studies [22, 27, 31, 18] have tested positive and negative fiber orientations, where a positive fiber orientation describes a "pitch-to-feather" strategy (i.e., loading decreases the

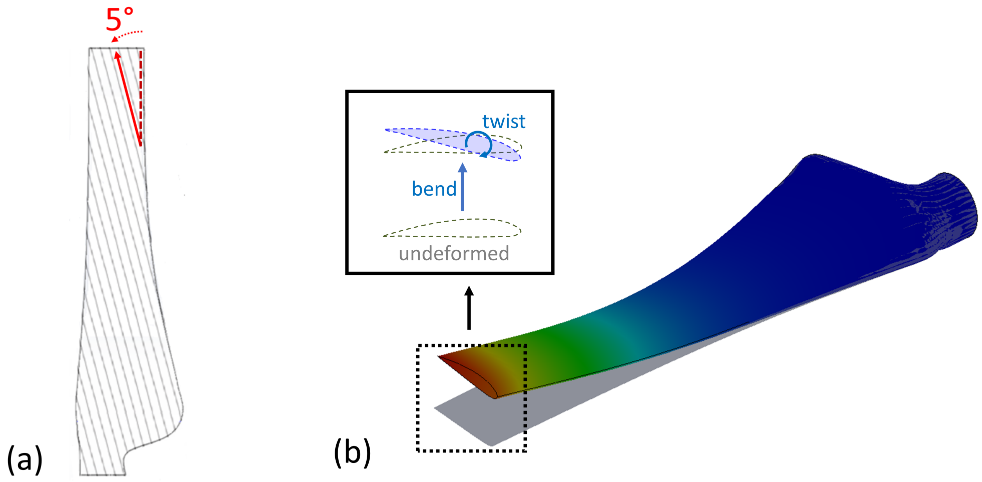

Figure 1.3: (a) Unidirectional, off-axis fibers result in anisotropic blade properties and (b) a coupling between flapwise deflection and spanwise twisting.

angle of attack) and a negative fiber orientation describes a "pitch-to-stall" strategy (i.e., loading increases the angle of attack). While both approaches reduce power output, it has been shown numerically [18, 32] and experimentally [27, 22] that pitch-to-feather designs will decrease blade loads while pitch-to-stall designs will increase blade loads. Consequently, positive fiber angle orientations are more suitable for operation in above-rated flow conditions when it is desirable to simultaneously decrease power output and blade loads. Several studies [21, 28, 24] have also tested pitch-to-feather designs against a neutral (0°) fiber angle or rigid blade and observed similar results. Since blade deformation increases with load, passive adaptive blades perform similarly to their rigid counterparts at lower inflow speeds [24]. Ideally, a bend-twist coupled blade should be designed to perform similarly to their rigid counterpart at lower or rated speeds, while alleviating loading at higher flow speeds. The feasibility of this approach has been demonstrated in prior work by Murray *et al.* [21] and Capellaro and Cheng [33].

The aforementioned studies investigating effects of fiber orientation focused on comparing a single positive and/or negative fiber orientation to a neutral or rigid blade. Given the suitability of pitch-to-feather strategies for marine current turbines, the next step is to implement these in blade design. Fluid-structural interaction (FSI) models combining a finite element model (FEM) with blade element momentum theory (BEMT) are often used for early stage blade design and provide the opportunity to study this effect numerically. For example, a numerical optimization by Barr [34] varied fiber orientation along the span of a passive adaptive wind turbine blade to maximize torque at various wind speeds, while a study by Bottasso *et al.* numerically tested 10°, 20°, and 30° fiber skins in combination with an active pitch controller to reduce fatigue in a composite wind turbine blades [35]. A simpler analysis using only a finite element model was used by Murray in [31] to analyze deformation and stress for blades built with different fiber orientations, thicknesses, and stacking sequences, and again in [36] to study the sensitivity of the FEM to inaccuracies in laminate thickness, material properties, and fiber orientation. While theoretical investigations of elastic tailoring provide insight into the effect of ply angle, thickness, material, and geometry on the bend-twist coupling of the blade [37] and FEM or static bench tests can provide insight into blade deformation given an applied load, neither produces information on turbine performance or accounts for the effects of rotation and induction. Models using FEM-BEMT or computational fluid dynamics and FEM can provide turbine performance and hydroelastic blade response, but come with common modeling challenges: tip losses, induction factors, correction for stall, obtaining appropriate foil data, turbulence, nonuniform inflow, and high computational costs.

Because of the added complexity in a variable-pitch design, passive pitch control, in which blades are designed to elastically deform under load without a servomotor, sensor, or control logic, is conceptually attractive. The bend-twist coupling allows for passive twisting of the blade towards the feathered position (i.e., decreased angles of attack) to shed power [18, 21, 22, 24], similar to an active pitch mechanism. Bend-twist coupled blades can also be designed to pitch towards stall (i.e., increased angles of attack) to shed power; however, this drastically increases thrust loads on the blades. Bend-twist coupled blades, or passive adaptive blades, have been researched in wind and propulsion for decades as a means to reduce structural loads [38, 39, 40, 41, 42, 43, 44, 45, 46, 35, 47, 48, 19, 49, 34, 37, 50, 51]. Conversely, despite the economic benefits of maintenance cost reduction and reliability improvement, passive adaptive blade research for current turbines is more limited.

Several studies have shown the feasibility of designing bend-twist coupled blades for tidal current turbines that perform similarly to rigid blades of the same geometry in Region II (i.e., at or below the rated speed) while alleviating loading in Region III [40, 21, 52], suggesting that passive adaptive blades could substitute for or augment an active Region III control strategy. A wind study by Lee and Flay [38] suggests passive pitch control alone is unlikely to regulate power successfully without being used in combination with another control strategy, due to the large twist angles required for adequate power shedding. Moreover, because the layup of composite blades has considerably more variability than machined blades [19] and submerged blades may experience varying material properties over time [18], combining active control and passive pitch strategies may be essential to compensate for performance variability due to imprecise or changing blade properties. Schottel Hydro, one of the few full-scale axial-flow current turbine developers using passive adaptive blades, uses combined passive pitch plus overspeed control in Region III, but their work is largely proprietary, and published results are limited to Region II performance [53, 25].

While a mix of recent experimental, computational, and theoretical work investigate the use of passive adaptive blades for tidal turbines, most studies to date have been focused on the following: validating simulations [36, 21, 54], blade design [21], modeling physical blade deformation [30], standalone hydrofoil testing and analysis [28, 27, 26], smoothing unsteady load fluctuations (e.g. from shear flow, turbulence, waves) [26], blade performance under combined wave and current loading [24], and/or characterizing passive adaptive blade performance and behavior for discrete operating conditions [22, 24, 54]. The aforementioned studies have greatly broadened our understanding of passive adaptive blades and their potential advantages for use in regulating power in marine current turbines, but there are no studies that offer an experimental implementation of passive pitch control and comparison of load reductions with rigid blade control strategies. This leaves some uncertainty around the effectiveness of passive pitch control as a Region III control strategy for current turbines. For example, a computational study by Motley and Barber [18] found that combining passive and active pitch control would not reduce structural loading or pitch actuation when compared to rigid blades with active pitch control, but there has been no experimental demonstration of this or other passive pitch control strategies, neither in isolation nor combined with an active control strategy. Furthermore, few studies offer experimental observation of physical blade response during turbine operation. Information about blade deformation during operation is important to characterize material stress and strain, as well as to understand the effectiveness of passive pitch control under a range of applications and flow conditions. Some deformation testing of standalone hydrofoils in a water channel has been conducted [28, 27], but this approach neglects the significant effects of rotation and induction. A single study by Wada *et al.* [29] presented preliminary results from experiments that captured blade deformation during turbine operation, but their methods and results were never translated to the archival literature.

1.4 Dissertation Objectives

The load reduction benefits of pitch control strategies for axial-flow turbines have been thoroughly demonstrated and adopted by the wind industry [11], but new research is necessary to explore the implications of active and passive pitch control for marine current turbines. As cost and inaccurate load estimates are still significant barriers to the adoption of marine current energy technology [12, 1, 2], experimental studies of pitch control can help move the field towards more economic and reliable technological designs. To this end, the overarching goal of this work is to experimentally investigate active and passive pitch control methods for axial-flow current turbines and assess their trade-offs with respect to load reduction.

Each chapter is this thesis supports an aspect of this investigation. Chapter 3 establishes a baseline understanding by, for the first time, experimentally demonstrating active blade pitch control alongside speed control strategies and comparing the measured turbine loads for each method. We discuss implications of the results on the choice of controller, taking into account the effect of Reynolds number, blockage, turbulence, and blade design. To inform the design of our passive pitch controller, we fabricate and test passive adaptive blades of varying fiber orientation, discussed in Chapter 4 along with appropriate scaling parameters for passive adaptive blades. The scaling discussion, important to the application of lab-scale research to full-scale systems, centers on two Cauchy-scaled turbine experiments that demonstrate similarity in blade deformation and non-dimensionalized thrust. Chapter 5 experimentally characterizes two passive adaptive blade pitch controllers and compares the measured turbine loads to that of previously tested control strategies. All tests conducted with the passive adaptive blades include high-speed video of blade deformation (deflection and twist) to develop our understanding of the hydroelastic, bend-twist behavior during turbine operation. The dissertation concludes with a summary and recommendations for future work in Ch. 6.

Chapter 2

METHODS

2.1 Turbine Instrumentation

The laboratory-scale, three-bladed horizontal-axis turbine used for these experiments was 0.45 meters in diameter and designed to allow variable speed and variable pitch. The drive train and instrumentation layout is detailed in Fig. 2.1. A six-axis load cell (Mini45, ATI Industrial Automation) was installed on the main shaft of the turbine, in the hub, to measure thrust and torque on the rotor. The turbine rotor was connected to a 5:1 gearbox (PV23, Parker Hannifin) and double-shaft stepper motor (LV233, Parker Hannifin), with an optical encoder (ZAA, Applied Motion) mounted on the rear shaft. The stepper motor allowed for precise control of the rotational speed, ω, verified by the encoder measurements. Additional stepper motors (208-13-01D, Lin Engineering), drives (EZHR17EN, All Motion), and optical encoders (E4P, US Digital) were installed in the hub to individually control the pitch angle, β, of each blade in increments of 0.125° via a worm gear and worm wheel. Power and communication signals were transmitted to the rotating hub through a slip ring (SR015 30050-1512-000, Rotary Systems), with the wiring passing through a hollow section of the main shaft. Because load cell measurements are sensitive to temperature, analog temperature sensors (TMP35, Analog Devices) were installed in the nose cone and hub cavity. As the motor was the primary heat source in the nacelle, copper wedges and conductive paste coupled the motor housing to the nacelle wall, increasing conductive heat transfer and minimizing the rise in nacelle air temperature. Further, the hollow section of the main shaft was potted to limit convective heat transfer between the hub and nacelle. Blade geometry, based on the NACA-44 airfoil series, is described in [22].

Data acquisition is shown schematically in Fig. 2.2. The data acquisition script was written using MATLAB and communicated in sequence with the load cell using CAN bus protocol and the stepper motor drives using RS485 protocol. Because of limited space within the hub, we prioritized frame size and torque rating in selecting the blade stepper motors, but the drives had a relatively slow communication rate. Consequently, the average sampling rate across all measurement channels was limited in most cases to $35 - 50$ Hz.

An additional six-axis load cell (Nano25, ATI Industrial Automation), installed at a blade root, measured thrust and torque on an individual blade (Fig. 2.3). Blade load cell measurements were used during single-bladed experiments, described in Ch. 4, since the loads from a single blade were too small to measure accurately with the driveshaft load cell.

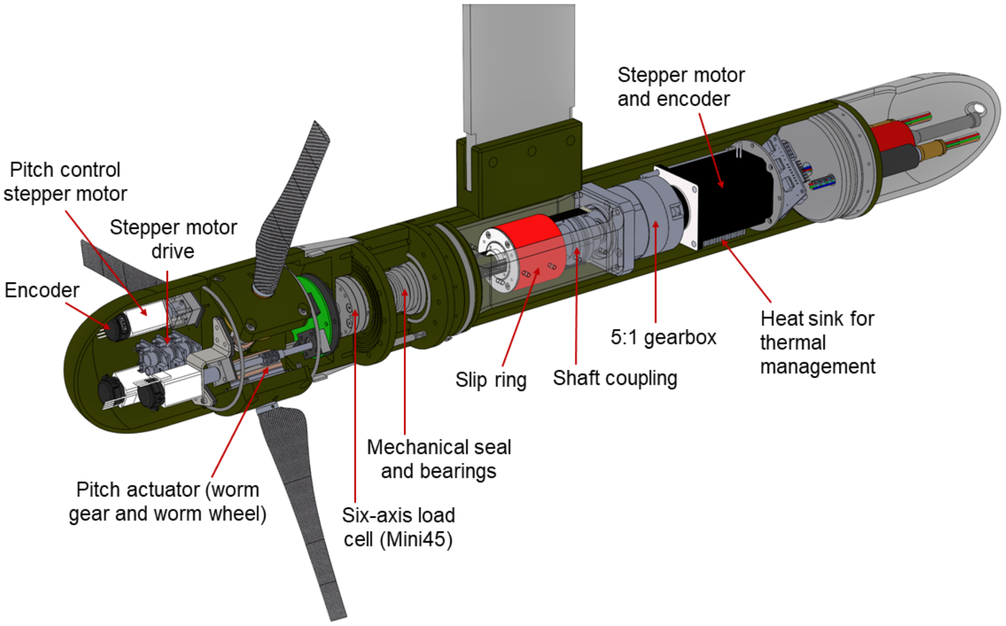

Figure 2.1: CAD model of turbine and instrumentation.

2.2 Experimental Facility

Experiments were conducted in the Alice. C. Tyler Flume at the University of Washington. Two pumps, controlled by a variable frequency drive, circulated water through a glass-walled,

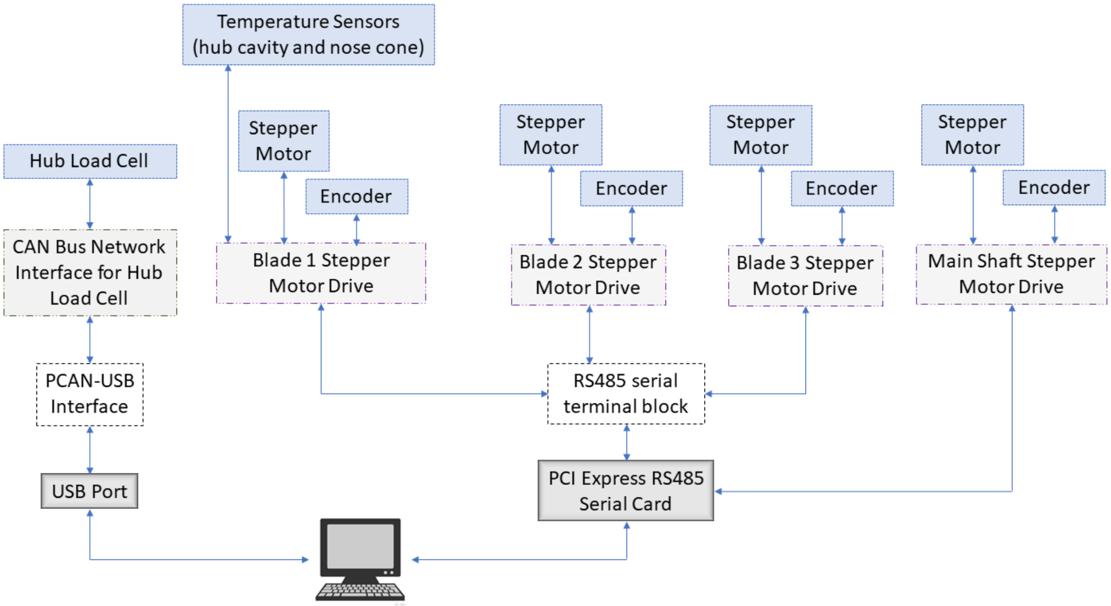

Figure 2.2: Data acquisition system block diagram for turbine instrumentation.

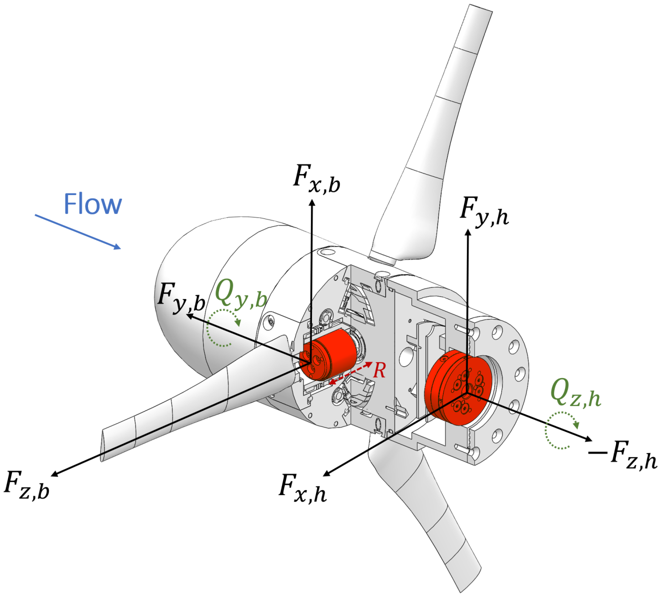

Figure 2.3: Blade and driveshaft load cell coordinate systems.

0.76-meter wide test section. Water fill height was adjusted to obtain a dynamic depth of 0.6 meters for all experiments. Pump frequencies were held constant during performance characterizations to maintain 0.7 m/s or 0.8 m/s inflow and varied during control strategy implementation to sinusoidally (Ch. 3) or linearly (Ch. 5) increase the flow. Depending on the inflow velocity, turbulence intensity, $I = \sqrt{u'^2}/\bar{u}$, ranged from from 2.0% to 4.4% (Table 2.1), where $\bar{u}$ is the mean inflow velocity and u' is the variation from the mean. Free-stream velocity, U_∞, was measured one meter downstream of the test section entry (3.4 turbine diameters or 154 cm upstream of the rotor plane) using an acoustic Doppler velocimeter (ADV, Nortek Vector) sampling at 64 Hz. Water temperature was maintained at $20°C$ for all experiments, unless otherwise specified.

We define the chord-based Reynolds number using the local chord length, c, at the 3/4 blade-span point (22.0 mm) as the characteristic length and the approximate relative velocity incident on the blade, neglecting induction, as the characteristic velocity:

$$Re_c = \frac{c\sqrt{U_\infty^2 + (\omega r_o)^2}}{\nu} = \frac{cU_\infty\sqrt{1+\lambda^2}}{\nu}, \tag{2.1}$$

where r_o is the the local turbine radius at the 3/4 blade-span point (183.5 mm) and ν is the kinematic viscosity at $20°C$. Specific ranges of Re_c for each experiment are specified in the corresponding chapter.

2.3 Performance Characterization

In Chapters 3-5, turbine performance is characterized as a function of tip-speed ratio, λ, which we define as the tangential speed of the blade tip relative to the free-stream velocity and calculated as

$$\lambda = \frac{\omega r}{U_\infty}, \tag{2.2}$$

where r is the radius of the turbine. Mechanical power output was calculated from the torque, Q, measured by the six-axis load cell on the driveshaft, and rotational speed, ω, from

Table 2.1: Turbulence intensities calculated for inflow speeds 0.4-0.8 m/s.

Inflow Speed (m/s)	Mean Turbulence Intensity
0.4	3.2%
0.5	2.2%
0.6	2.0%
0.7	3.4%
0.8	4.4%

the stepper motor, and non-dimensionalized as the coefficient of performance

$$C_P = \frac{\langle Q\omega \rangle}{0.5 \rho_f A \langle {U_\infty}^3 \rangle} \tag{2.3}$$

where A is the rotor swept area, ρ_f is the water density at $20°C$, and U_∞ is being measured upstream from the rotor plane by the ADV. The averages for the mechanical power and kinetic power are calculated separately due to asynchronous clocks. This approximation is acceptable given the low turbulence intensity in the flume. Thrust, T, measured by the load cell on the driveshaft, was used to calculate the coefficient of thrust

$$C_T = \frac{\langle T \rangle}{0.5 \rho_f A \langle {U_\infty}^2 \rangle} \tag{2.4}$$

Due to blade weight and imperfect weight distribution in the hub, there were azimuthal variations in static force and torque measured by the load cell. To account for this, at the beginning of each test, tare measurements were collected at 12 equidistant azimuthal positions (Fig. 2.4a). During post-processing, measured torque and thrust were adjusted by a spline interpolation of the azimuthally-dependent tare values taken in quiescent flow (Fig. 2.4b) or, in Chapters 4-5, an average of the tare values was used.

During tests in constant free-stream velocity, at each tip-speed ratio, C_P and C_T were

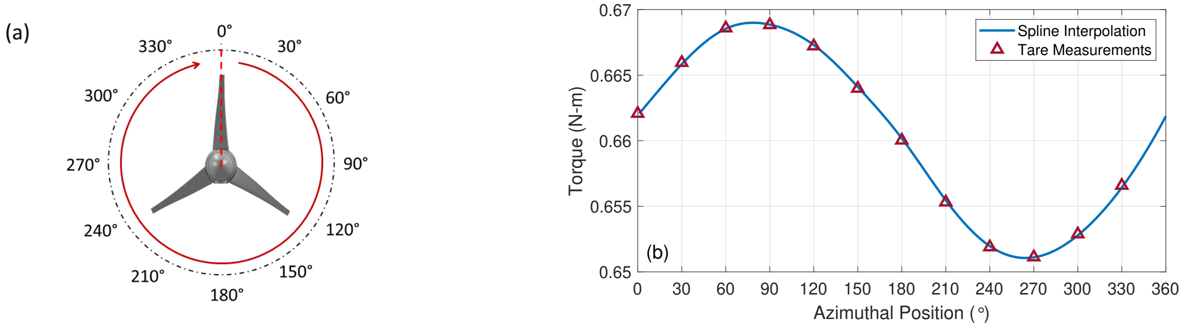

Figure 2.4: To account for azimuthally-varying static force and torque, (a) tare measurements were taken at 12 equally-spaced positions and (b) a spline interpolation was used to calculate dynamic loads and torques for instantaneous data.

calculated over 4500 or 9000 samples, or 50-380 revolutions depending on the rotational speed. Averaging over a whole number of rotations was confirmed to be inconsequential when averaging over such a high number of turbine rotations. For the use of flexible, composite blades, we considered adapting the calculation of swept area in Eqns. 2.3 and 2.4 to account for deflection, but the effect was small compared to experimental uncertainty. For example, the maximum observed deflection only changes the swept area by 1.4%.

For the single-bladed tests described in Ch. 4, C_T was calculated using Eqn. 2.4 but using the thrust, $F_{y,b}$, measured by the load cell located at the blade root, while C_P was calculated using Eqn. 2.3, adjusted to account for the distance between the blade load cell and the driveshaft axis of rotation:

$$C_{P,blade} = \frac{\langle (Q_{y,b} + F_{x,b} R)\omega \rangle}{0.5\rho_f A \langle {U_\infty}^3 \rangle}, \tag{2.5}$$

where $Q_{y,b}$ is the torque on the blade in the streamwise direction, $F_{x,b}$ is the force on the blade in the plane of rotation, and R is the distance from the sensor head to the rotor's driveshaft (3.57 cm) (Fig. 2.3).

Chapter 3

ACTIVE BLADE PITCH CONTROL

This chapter compares active blade pitch control and speed control methods experimentally and quantifies the trade-offs between variable-pitch and fixed-pitch turbine designs. Further, we explore the implications of control across turbine scale. This can be coarsely partitioned into regimes where characteristic performance varies or is independent of Reynolds number. Most utility-scale turbines will operate in the Reynolds-independent regime, but laboratory testing or Blue Economy applications [55] involve small rotor dimensions and/or low currents that put them in the Reynolds-dependent regime. The results presented in this chapter have been published in the Journal of Ocean Engineering and Marine Energy [10].

3.1 Methods

3.1.1 Pitch Characterization

Prior to control testing, we characterized the turbine performance as a function of blade pitch, β, and tip-speed ratio, λ, using the methods outlined in Sec. 2.3. Performance was characterized for blade pitch angles between $-7°$ and $+33°$ in increments of $5°$ at an inflow velocity of 0.8 m/s (Fig. 3.1). A positive blade pitch corresponds to a “pitch to feather” strategy (decreasing angle of attack) and negative blade pitch corresponds to a “pitch to stall” strategy (increasing angle of attack). This reference frame is labeled on the schematic in Fig. 3.2. Note that blade pitch, β, is measured at the blade tip, so a blade pitch of $0°$ indicates that the blade chord line at the tip is parallel to the plane of rotation.

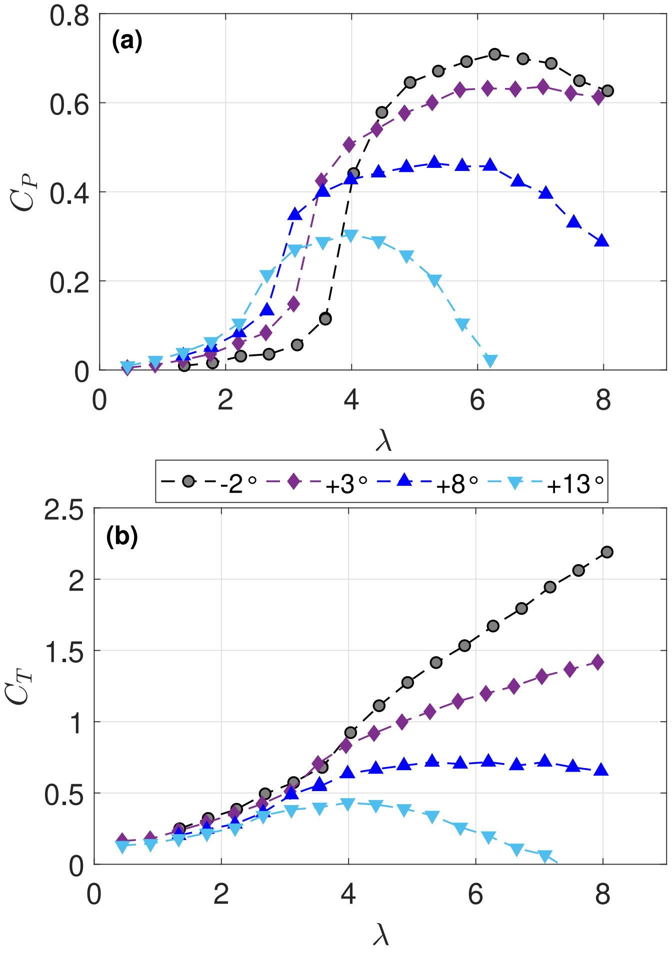

Figure 3.1: Coefficients of (a) performance and (b) thrust as a function of tip-speed ratio, λ, for various blade pitch settings at 0.8 m/s inflow velocity. -2° is the optimal pitch angle. Note that the -2° performance curves describe the control space for a fixed-pitch turbine operating with speed control.

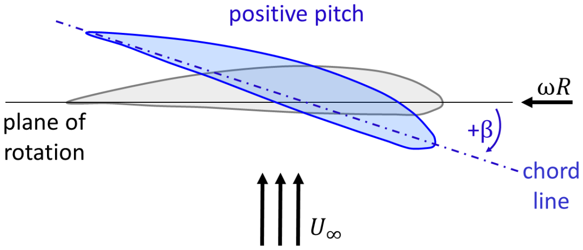

Figure 3.2: Blade pitch schematic showing that positive blade pitch angles correspond to blade rotation towards the feathered position (i.e., decreasing the angle of attack). Pitch is measured at the blade tip, so a blade pitch of 0° indicates that the blade chord line at the tip is parallel to the plane of rotation.

3.1.2 Region III Control: Reynolds-number Independent Conditions

First, we consider the case of Region III control when the turbine is operating in a regime where C_P and C_T are independent of Reynolds number. In our experiments, Re_c ranged from $1.3 \cdot 10^4$ at the lowest inflow velocity and tip-speed ratio (0.4 m/s, $\lambda = 1$) to $1.9 \cdot 10^5$ at the highest inflow velocity (0.84 m/s, $\lambda = 10$). Water temperature and, therefore, ν, was maintained by a chiller at $19°C$ for all experiments. Reynolds-independence was observed for $Re_c > 9 \cdot 10^4$, identified when power and thrust coefficients varied by $< 1\%$ when inflow velocity increased from 0.7 m/s to 0.9 m/s and tip-speed ratio and temperature were held constant ($\lambda = 6$, $19°C$). We also note that power and thrust coefficients were within 5% of the Reynolds-independent values for $Re_c > 8 \cdot 10^4$, identified similarly by increasing the inflow velocity from 0.6 to 0.9 m/s while tip-speed ratio and water temperature were held constant. Note that this chapter uses a slight variation of Eqn. 2.1 for Re_c where r_o is $0.75(D/2)$ rather than the 3/4 blade-span point.

Proportional controllers were used to maintain constant mechanical power by modulating rotational speed or blade pitch (Fig. 1.2). The “rated” operating condition was defined as the rotational speed corresponding to maximum efficiency for the -2° pitch case at a speed of 0.7 m/s. Pitch control actuated the blade pitch towards feather while holding rotation rate constant. Speed control actuated rotational speed while holding blade pitch constant. Controller gains for speed and pitch control were tuned in an *ad hoc* manner to yield acceptable performance (i.e., rise time, overshoot). This simplistic control was sufficient for our purposes and could be augmented by integral or derivative gain, or non-linear control [56]. To reduce noise in the input signal to the controller, a moving average filter of 300 samples (20-30 revolutions) was applied to the measured mechanical power. This relatively long averaging window was motivated by the relatively slow data acquisition rate of 35 Hz (limited by the update rate of the blade stepper motors). The controller implementation is shown schematically in Fig. 3.3. To compare the three control strategies, we oscillated the inflow from 0.7 to 0.8 m/s over a 20-minute period to emulate the low-frequency variation in tidal currents, as shown in Fig. 3.4. As shown in Fig. 3.5, turbine characteristic performance is independent of Reynolds number for most test conditions. However, the underspeed controller, does dip into the Reynolds-dependent regime. The implications of this are discussed further in Sections 3.3.1. We note that pitch control holds Re_c approximately constant while shedding power, underspeed control reduces Re_c, and overspeed control increases Re_c.

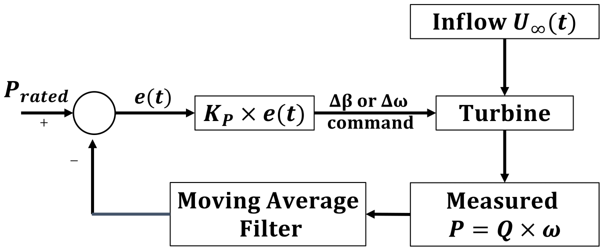

Figure 3.3: Proportional controller block diagram.

For underspeed and pitch control, controller performance was characterized by the stan-

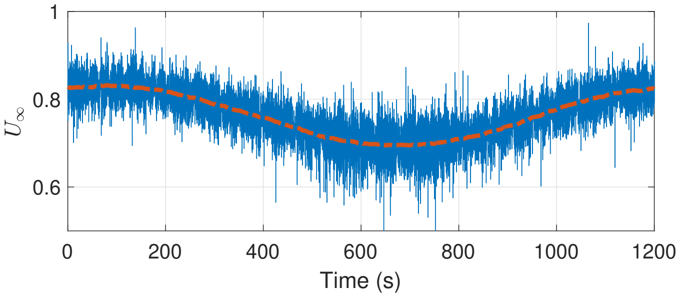

Figure 3.4: Representative time series from the ADV during oscillating inflow between 0.7 and 0.8 m/s with a 20 minute time period. Orange dashed line shows the one-minute moving average.

dard deviations of the measured power output relative to the rated power (i.e., control set point). Overspeed control was not implemented experimentally due to physical limitations of the setup. Specifically, at high rotation rates, the main stepper motor produced substantially more heat, causing the nacelle and hub temperatures to rise, which affected load cell accuracy. This was not a concern during the steady state inflow tests, which required only 90-100 seconds of data collection at each tip-speed ratio, such that temperature changes were limited. For this reason, a synthetic overspeed controller was compared to experimental pitch and underspeed controllers. The required efficiency to maintain constant power output was calculated at each point in the experimental inflow time series from the pitch control case and the corresponding thrust and torque values were determined from the performance curves in Fig. 3.1 for the $-2°$ case. To compare the effects of the controller type on the turbine loads in Region III, mechanical power was normalized by power at the rated operating condition (i.e., P_{rated}), and thrust and torque were similarly normalized by their values at the rated operating condition.

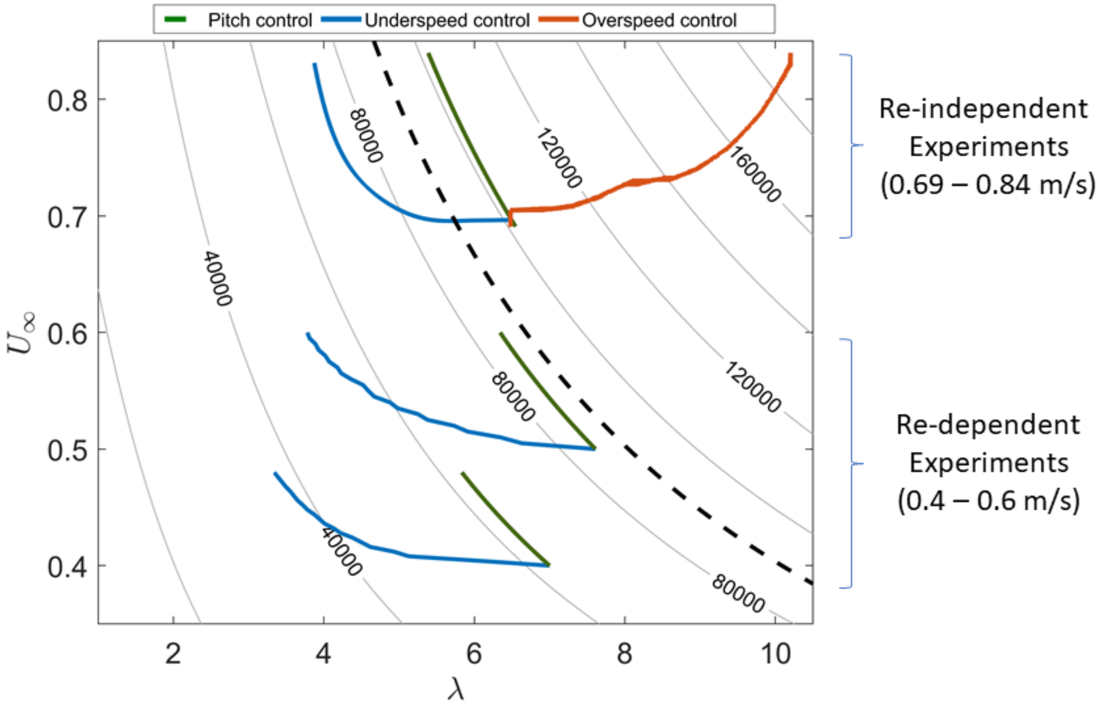

Figure 3.5: Contour lines of constant Reynolds number, $Re_c = c\sqrt{U_\infty^2 + (\omega r)^2}/\nu$, as a function of inflow velocity and tip-speed ratio. Lines of constant Re_c are in grey while each colored line corresponds to the range of Reynolds numbers for a particular combination of control strategy and range of inflow velocities. Reynolds-independence was observed above $9 \cdot 10^4$, as denoted by the dashed black line.

3.1.3 Region III Control: Reynolds-number Dependent Conditions

Second, to understand how trends in controller performance change with Reynolds number, we conducted a synthetic experiment using underspeed and pitch control for two Reynolds-number dependent flow regimes: oscillations from 0.4-0.5 m/s and 0.5-0.6 m/s. To do so, we linearly interpolated between the performance characterizations at constant velocity (included in Appendix A) to obtain C_P and C_T as a function of blade pitch, tip-speed ratio, and inflow velocity and prescribed a sinusoidal inflow velocity. The overspeed cases could not be evaluated in this manner since we could not achieve sufficiently high tip-speed ratios to achieve the required C_P reductions to hold power constant. It is also important to note that, there was a 5° difference in preset pitch angle between the Reynolds-independent control tests and Reynolds-dependent performance characterizations, such that results cannot be directly compared. For this reason, the simulation was repeated for 0.7-0.8 m/s using the same preset pitch angle to provide comparable results between Reynolds-dependent and Reynolds-independent regimes. This synthetic experiment approach was chosen over physical experiments as a simple matter of expediency. As discussed in Section 3.2.2, good agreement was observed between experimental results and the synthetic approach. A lower preset pitch angle for the Reynolds-independent tests was necessary to simulate the overspeed controller. At $\beta = 3^\circ$, the peak of the C_P curve was too broad as it extended out to high tip-speed ratios, such that the reduced efficiency required to maintain power could not be achieved within the range of tip-speed ratios tested. At $\beta = -2^\circ$, the C_P curve narrows sufficiently to maintain power within the same tip-speed ratio range, so $\beta = -2^\circ$ was used for these tests. Though the preset pitch angles differ, we can still investigate, separately, the effect of control strategy on turbine loading within each sets of experiments.

3.2 Results

3.2.1 Characteristic Turbine Performance

Figure 3.1 shows C_P and C_T as a function of tip-speed ratio at an inflow of 0.8 m/s for a subset of blade pitch angles, where $-2°$ is the optimal preset pitch angle. For high tip-speed ratios that are outside the partial stall region (where lift decreases and drag increases), increasing blade pitch towards "feather" (i.e., decreasing the angle of attack) decreases the efficiency and thrust, in line with previously reported experimental results (e.g., [7]). This is reversed for C_P at lower tip-speed ratios, where part of the blade is in stall, as increasing pitch results in reattached flow for part of the blade, producing more lift (i.e., higher efficiency). This result is also in line with previous studies (e.g., [57]).

A contour map of C_P as a function of tip-speed ratio and blade pitch is shown in Fig. 3.6a. A similar map for C_T is shown in Fig. 3.6b, while Fig. 3.6c indicates the operating points where experimental data was collected. We can visualize from the contour maps, interpolated between all pitch characterizations, how we might manipulate β or λ to achieve the efficiency changes required to respond to changing inflow conditions. Furthermore, we can observe the clear limits of overspeed actuation in Fig. 3.1, looking at the $-2°$ case, which corresponds to the pitch angle for overspeed and underspeed control: C_P decreases slowly as λ increases. Thus, excessive rotation rates would be required to maintain constant power as current speed increases.

Finally, we note that C_P exceeds the Betz limit for some combinations of β or λ. This is simply a consequence of the relatively high blockage ratio under which these experiments were conducted [58, 59].

3.2.2 Region III Control: Reynolds-number Independent Regime

Figure 3.7 shows the time series of oscillating inflow for the pitch control test (with the underspeed test being similar except for the stochastic fluctuations caused by turbulence), calculated power output, controlled speed or pitch, and normalized thrust and torque com-

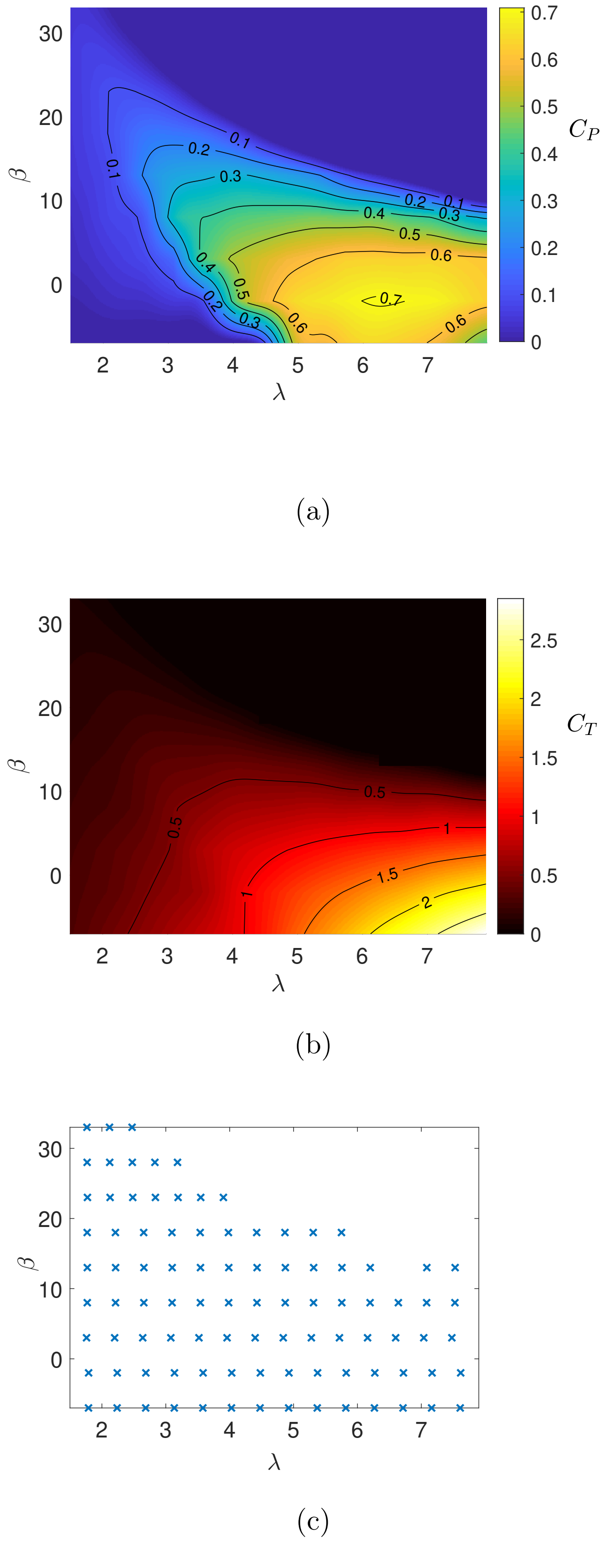

Figure 3.6: (a) C_P and (b) C_T contour maps as a function of tip-speed ratio (λ) and blade pitch (β) in 0.8 m/s flow. (c) indicates operating points where experimental data was collected.

pared for the three controllers. We again note that the overspeed controller results are synthetic, as this could not be achieved in practice given experimental temperature-control limitations. The implementations of pitch and underspeed control succeeded in maintaining power with a standard deviation of 3-4% for both controllers, which is comparable to the 2% deviation observed during the constant inflow experiments over the same tip-speed ratios and with the same filtering. Controller ability to maintain power can be seen visually in the time series of the oscillating inflow velocity (Fig. 3.7a) and power output relative to the rated power (Fig. 3.7c). For comparison, the power output would exceed the rated power by 60 % if no control was employed (i.e., pitch and rotation rate remained constant as inflow velocity increased). The actuated rotational speed or pitch for each control strategy is shown in Fig. 3.7b.

As expected, we observed that operating in an overspeed mode reduces torque but dramatically increases thrust and vice versa for underspeed control. It should be noted that because of the steep drop-off in efficiency at tip-speed ratios below the rated condition (Fig. 3.1a), only slight changes in rotational speed were required for underspeed control and, consequently, rotation rate appears almost constant in the time series in Fig. 3.7b. For the pitch control, since the turbine maintained constant rotational speed and power, torque stayed at its rated value, but as the blades pitched towards feather, rotor thrust was significantly reduced. This is a realization of the characteristic performance shown in Fig. 3.1, where we see that increasing the pitch at a constant tip-speed ratio decreases C_P and C_T. Because of this, pitch control reduces thrust below the rated condition while maintaining constant power and torque. A summary of the maximum changes in torque and thrust from the rated condition for each control case is provided in Table 3.1.

To confirm that the synthetic overspeed control performance is realistic, we compared the experimental underspeed controller with a synthetic underspeed controller using the same methodology used for overspeed. The mean change in torque and thrust for the synthetic underspeed controller remained within 2% of the experimental values. Consequently, the synthetic overspeed results are likely a good approximation of what would be observed ex-

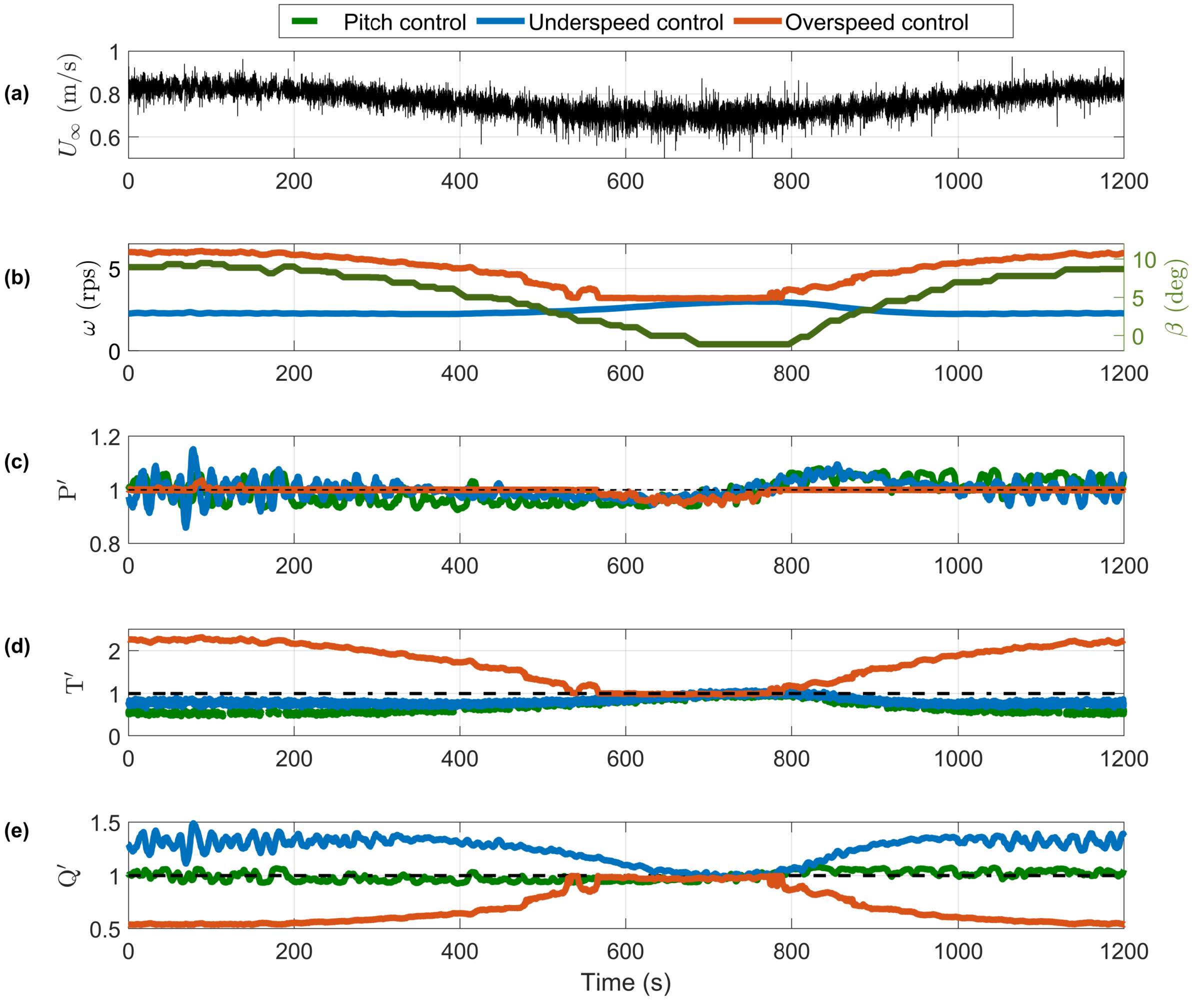

Figure 3.7: Time series for (a) free stream velocity, (b) rotor speed (left axis) for speed control or blade pitch (right axis) for pitch control, (c) power output relative to the rated power (d) normalized rotor thrust, and (e) normalized rotor torque for overspeed, underspeed, and pitch control. The overspeed case is a synthetic output based on the measured free stream velocity during the pitch control case and the performance characterization from Fig. 3.1. For both under- and overspeed control, blade pitch was maintained at $-2°$. For pitch control, rotor speed was maintained at 3.2 rps.

Table 3.1: Maximum changes in torque and thrust from the rated condition for each controller in 0.7-0.8 m/s oscillating inflow. Blade preset pitch angle is $-2°$.

Controller	Maximum change in torque from rated condition	Maximum change in thrust from rated condition
overspeed (synthetic)	-46%	+127%
underspeed (experimental)	+35%	-25%
pitch (experimental)	+5%	-48%

perimentally and the synthetic approach should be similarly effective in the Reynolds-number dependent regime.

3.2.3 Region III Control: Reynolds-number Dependent Regime

Figure 3.8 and Table 3.2 show equivalent results for synthetic underspeed and pitch controllers operating in a Reynolds-number dependent regime. For these cases, performance at maximum efficiency for either 0.4 or 0.5 m/s is taken as the “rated” condition. As in the Reynolds-independent regime, we observe comparable thrust loads, with either strategy bringing thrust $20 - 35$ % below the rated value (Table 3.2). Again, for pitch control, the torque is constant. Underspeed control, however, increases the maximum normalized torque by 75% in 0.4 – 0.5 m/s flow and 68% in 0.5 – 0.6 m/s flow. For comparison to the Reynolds-independent regime, the synthetic 0.7-0.8 m/s case for underspeed and pitch control is also shown in Fig. 3.8 and Table 3.2. Maximum changes in normalized thrust were, again, similar between controllers and inflow cases while the torque averaged 49% above the rated value for the underspeed controller, a smaller load increase than in the Reynolds-dependent regime. As a reminder, the synthetic 0.7-0.8 m/s results in Table 3.2 differ from the experimental results in Table 3.1 because different preset pitch angles were used to define the rated

Table 3.2: Maximum changes in torque and thrust from the rated condition for each controller, simulated for two oscillating inflow cases below Reynolds-independence (0.4-0.5 m/s and 0.5-0.6 m/s) and one case at Reynolds-independence (0.7-0.8 m/s). Blade present pitch angle is +3°.

Inflow Range	Controller	Maximum change in torque from rated condition	Maximum change in thrust from rated condition
0.4-0.5 m/s	Underspeed	+75%	-24%
	Pitch	0%	-35%
0.5-0.6 m/s	Underspeed	+68%	-27%
	Pitch	0%	-31%
0.7-0.8 m/s	Underspeed	+49%	-22%
	Pitch	0%	-32%

condition.

3.3 Discussion

3.3.1 Reynolds Number Effects

In lower flow speeds, turbine performance and hydrodynamic loading are a function of tip-speed ratio, blade pitch, and Reynolds number, so relative changes in thrust and torque with blade pitch or rotational speed are accentuated. For example, a turbine using overspeed control in a Reynolds-independent regime sees an increase in kinetic energy available at higher flow speeds and must increase rotational speed to decrease efficiency and maintain power; however, a turbine using overspeed control in a Reynolds-dependent regime sees both an increase in kinetic energy and an increase in C_P and C_T at higher Reynolds numbers,

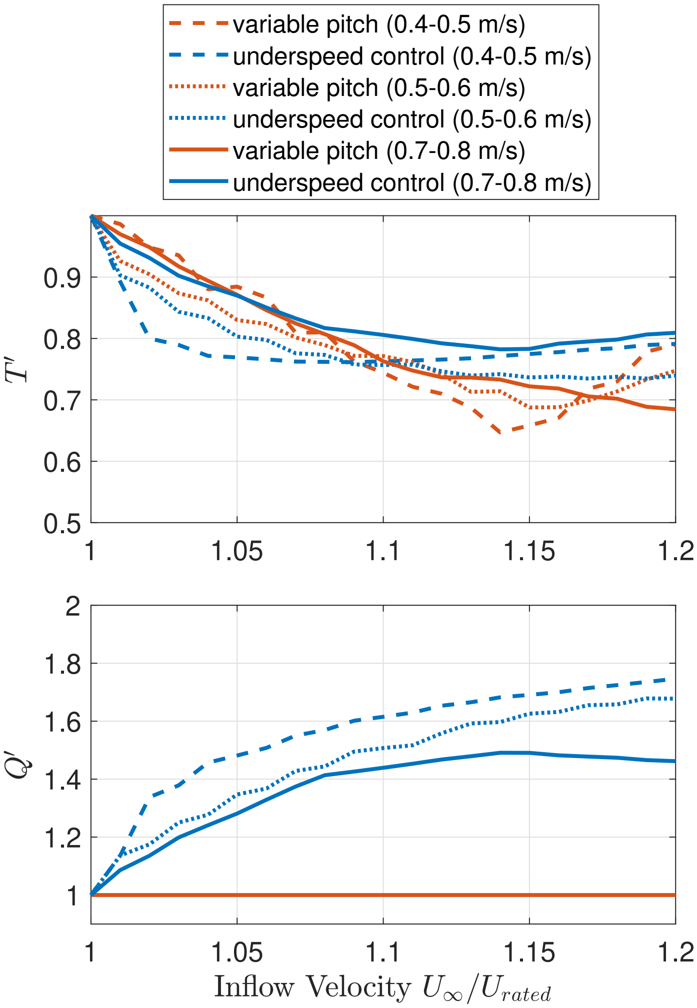

Figure 3.8: Normalized (a) rotor thrust and (b) rotor torque using underspeed and pitch control, simulated in oscillating inflow ranges of 0.4-0.5 m/s, 0.5-0.6 m/s, and 0.7-0.8 m/s.

so the required rotational speed to maintain power must counteract both. These excessive rotational speeds result in exacerbated thrust loads relative to overspeed control in Reynolds-independent regimes.

This means that the advantages and disadvantages of each controller are exaggerated below Reynolds-independence. This increases the relative benefit of pitch control, which can accommodate variations in current in Region III without increasing torque or thrust. For example, in Fig. 3.8 and Table 3.2, we see that while reductions in normalized thrust for the blade pitch and underspeed controllers are comparable for all three inflow ranges, the normalized torque increases consistently for underspeed control as we move further into the Reynolds-dependent regime. Practically, this would increase generator unit costs for underspeed control relative to blade pitch control.

The distinction between Reynolds-independent and Reynolds-dependent experiments presented in this study is imperfect, as the underspeed controller dips below the threshold for Reynolds-independence at inflow speeds that result in Reynolds independence for the other two controllers. Because load reductions/increases for each controller are exaggerated below Reynolds-independence, it is likely that the underspeed controller produces a slightly higher torque and lower thrust in experiments (Table 3.1) than if the inflow velocity was high enough to achieve Reynolds independence for all three controllers. However, power and thrust coefficients within 5% of the Reynolds-independent values occurred above $8 \cdot 10^4$, such that consequences of Reynolds dependence are likely limited. Furthermore, the synthetic pitch controller tested in 0.5-0.6 m/s inflow operates nearly at Reynolds-independence (Fig. 3.5) and, consequently, there is almost no difference in maximum thrust between the 0.5-0.6 m/s and 0.7-0.8 m/s pitch controllers reported in Table 3.2. However, because the underspeed controller remains Reynolds-dependent and the pitch controller always maintains constant torque, this still provides insight into torque reductions relative to underspeed control is as we move further into the Reynolds-dependent regime.

It is important to note that our synthetic evaluation is based on the effects of linear interpolation between a range of constant speed inflow conditions. Curvature between interpolation points is anticipated at lower Reynolds number (Figure 3.5). This likely means that the simulated loads are underpredicted at lower Reynolds numbers since increases in torque and thrust coefficients with Reynolds number become smaller as C_P and C_T approach Reynolds-independence (Fig. 3.5). Consequently, thrust loads may be similarly underpredicted for the pitch and underspeed control. However, the relative benefit of blade pitch control is likely even greater than shown in Table 2 due to the underpredicted torque loads compared to the constant torque maintained during blade pitch control.

3.3.2 Blockage Effects

Turbine performance in this study is affected by the relatively high blockage ratio (35%) in the test section. Blockage limits expansion of the streamlines around the turbine, resulting in higher flow velocity through the rotor plane and, thus, higher thrust and power than in an unconfined channel [60]. Because equivalent unconfined performance depends on the blockage ratio and rotor thrust [61, 59] and the rotor thrust varies between and within each control scheme, the absolute differences between control schemes are specific to this operational setting. This is also an important distinction between current turbines, which can operate in confined flows, and wind turbines, which are unconfined. It is likely that the high blockage ratio in these experiments exacerbated the thrust loads at high tip-speed ratios, further broadening the peak in C_P to the disadvantage of overspeed control. This effect is demonstrated in the blockage-corrected results (produced using the model presented in [62]) for a pitch angle of -2° in 0.8 m/s flow (Fig. 3.9), where we observed a reduction in C_P and C_T over most tip-speed ratios and a narrower peak in C_P. While this does not discount the excessive loading found in overspeed control relative to underspeed and pitch control, similar experiments conducted in unconfined flow would be useful for determining more exact loading estimates.

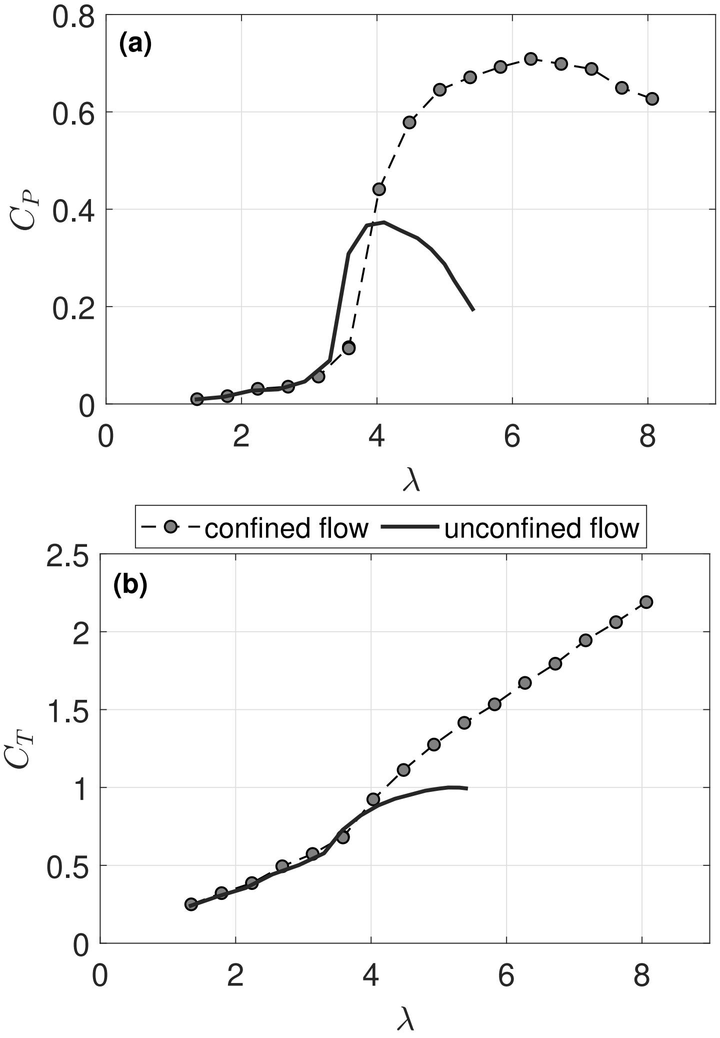

Figure 3.9: Coefficients of (a) performance and (b) thrust as a function of tip-speed ratio, λ, for the turbine in confined flow (35% blockage) and unconfined flow. The confined flow result is based on experimental measurements in 0.8 m/s flow with a pitch angle of $-2°$, while the unconfined flow result is estimated using a blockage correction based on the model presented by [62].

3.3.3 Turbulence Effects

The turbulence intensities, I, observed in this study and reported in Table 2.1 were relatively low (2-4%). Increased turbulence levels generally have negative impacts on turbine performance, including decreased C_P and higher fluctuations in power and thrust [63]. However, at lower Reynolds number, turbulence can improve performance by tripping an early development of a turbulent boundary layer on the blades and prevent the formation of a laminar separation bubble which would otherwise thicken the boundary layer and lead to partial stall and reduced lift.

In this study, at $\lambda = 6$, $U_\infty = 0.6$ m/s, and $I = 2\%$, we were within 5% of Reynolds-independent C_P values, so it is unlikely that the higher turbulence intensities at higher inflow velocities have a significant effect on our experiments. However, advantages of pitch control may be influenced by the higher turbulence intensities at actual tidal energy sites. Specifically, while turbulence intensities may be as low as $5-6\%$ at some sites [64], locations with higher turbulence intensity, such as 10-15% [65, 66], may trip the boundary layer to turbulence and produce Reynolds-independent performance at relatively low Re_c. This would reduce the magnitude of torque and thrust changes reported in Table 3.2 and the relative advantages of pitch control.

3.4 Conclusion

While Region III blade pitch control is standard practice in wind turbine design, it is not uniformly employed by current turbines. Experiments were conducted with a scale-model turbine in oscillating inflow to mimic low-frequency fluctuations above the turbine's rated inflow speed. Proportional underspeed and pitch controllers were implemented experimentally, while overspeed control was emulated in a Reynolds-number independent regime. All three control types were then emulated in Reynolds-number dependent regimes.

Results demonstrate that, regardless of Reynolds-number dependence, pitch control significantly reduces the thrust and torque relative to either speed control strategy. Further, the relative benefit from pitch control increases at lower Reynolds number. Ultimately, controller selection requires considering costs and benefits of each control strategy. The higher turbine loads for overspeed control suggest this control strategy may only be viable for current turbines with specific blade geometries and may be particularly poorly suited to turbines operating in confined flow. The choice between pitch and underspeed control may be more subtle, depending on the specifics of turbine design and variation in operating conditions.

Chapter 4

PASSIVE ADAPTIVE BLADE CHARACTERIZATION & CAUCHY-SCALING

Ch. 3 considers the range of control options when rigid blades are employed. As discussed in Ch. 1.3, the bend-twist coupling of composites can be used to expand the possible control space. Given the lack of specific experimental studies into the effect of positive fiber orientation and bend-twist coupling on turbine performance and deformation response, this chapter provides novel experimental data for blades of varying fiber orientation (0°, 2.5°, 5°, and 10°), including static mechanical testing, measurements of rotor loads during turbine operation in a recirculating flume, calculation of turbine performance, and high-speed video observation of blade deformation over a range of tip-speed ratios in Reynolds-independent flow. In doing so, this work contributes to the body of knowledge on the effect of ply orientation on blade performance and blade deformation during turbine operation.

4.1 Non-dimensional Scaling Laws

While dimensionless scaling relations have been extensively studied for current turbines with rigid blades [67, 68], relatively few studies discuss appropriate hydroelastic scaling for flexible blades with tailored off-axis fiber orientations. Extending laboratory results to full-scale, open-water applications requires an understanding of hydrodynamic and hydroelastic scaling to use the existing data correctly in the design of large systems.

While the body of knowledge for aeroelastic scaling in aircraft applications is vast [69, 70, 71], this does not translate directly to current turbines because of large differences in the solid-to-fluid density ratio and Reynolds numbers. A relatively small number of prior studies investigate hydroelastic scaling for marine propulsion and lifting bodies [72, 73, 74, 75, 76, 77] and wind turbine applications [37, 50, 78].

Cauchy similarity is important when modeling a structure with significant elastic forces [72]. We define the Cauchy number, Ca, as:

$$Ca = \frac{\rho_f {U_\infty}^2}{E}, \tag{4.1}$$

where ρ_f is the density of the fluid, U_∞ is the free-stream velocity, and E is the transverse flexural modulus of the blade (i.e., corresponding to bending primarily in the spanmwise direction).

The relevant non-dimensional parameters identified by Young [76] that govern elastic marine propulsor performance are: advance coefficient (equivalent to the tip-speed ratio in turbine literature), Froude number, Reynolds number, Mach number, cavitation number, bend-twist coupling, elasticity ratio (equivalent to the Cauchy number), density ratio between the solid and fluid, and ratio of effective bending stiffness to torsional stiffness. While matching Froude, Reynolds, and Mach number cannot be achieved simultaneously, Motley and Young [74] and Young [76] recommend prioritizing Mach scaling in cases where gravitational effects are negligible and the boundary layer is fully turbulent (i.e., where performance is Reynolds-independent). However, this requires matching the free-stream velocity and material properties between the model and full-scale prototypes, which can be difficult or impossible to achieve in many small-scale facilities.

A recent study by Young et. al [77] demonstrates, through a numerical model, that when Cauchy similarity is achieved between model and full-scale, the same steady-state loads and deformations are observed across scales, even when the density ratio is not maintained. It is precisely this numerical result that we aim to experimentally demonstrate in this study for a marine current turbine. Consequently, our second objective is to experimentally confirm that scaling with Cauchy number yields similar steady-state blade loading and blade deformations for different flow conditions and blade material properties.

4.2 Methods

4.2.1 Blade Fabrication

The blade design and fabrication process used in this work is similar to that described in [22]. A thicker root was used to manage an undesirable stress concentration identified by Barber *et al.*, and adjustments to the blade fabrication process were implemented to minimize blade-to-blade variability. The exact blade geometry, based on the NACA-44 airfoil series, is provided in Appendix C.1.

Since small-scale composite blades can be difficult to fabricate using conventional methods without excessive stiffness and inaccuracies in fiber orientation [31, 22], a nonconventional layup technique was used for these blades. Figure 4.1 shows the fully fabricated, 17 cm composite blade, consisting of a 7-ply (1.4 mm thick) carbon fiber spar (Hexcel AS4, 12K filament count) which provides the desired bend-twist coupling, cast in a semi-rigid polyurethane (Smooth-cast 45D) which provides the desired hydrofoil cross-section and hydrodynamic behavior. This semi-rigid body allows the material properties of the carbon fiber to dominate the overall mechanical properties of the blade. Four sets of composite, passive adaptive blades with varying fiber angle orientation were fabricated: 0°, 2.5°, 5°, and 10°. The neutral, 0° fiber blades kept a unidirectional fiber orientation along the blade span, intended to induce no twist under load. The remaining sets were fabricated with an off-axis fiber orientation such that the blade pitches towards the feathered position under loading, decreasing the angle of attack (Fig. 1.3). A fifth set of passive adaptive blades was fabricated using a 5-ply (1.0 mm thick) spar and 10° fiber orientation for the Cauchy-scaling experiments outlined in Sec. 4.2.3. Use of fiber orientations greater than 10° is impractical in most current turbine applications, as the bending stiffness decreases drastically for larger ply angles and blades with large bend-twist couplings may not have favorable performance below rated flow conditions. For example, the estimated bending stiffness for a 10° fiber spar in our study is 7.6% less than that of a neutral blade, while a 30° fiber spar would be expected to have a 62% decrease in bending stiffness relative to the neutral blade.

To provide a rigid blade reference, a set of aluminum blades matching the unloaded blade geometry of the composite blades were machined. Since 3-4% shrinkage in chord length relative to the mold dimensions was observed during the curing of the polyurethane, the aluminum blade profile was extracted from computerized tomography (CT) scans of the composite blades.

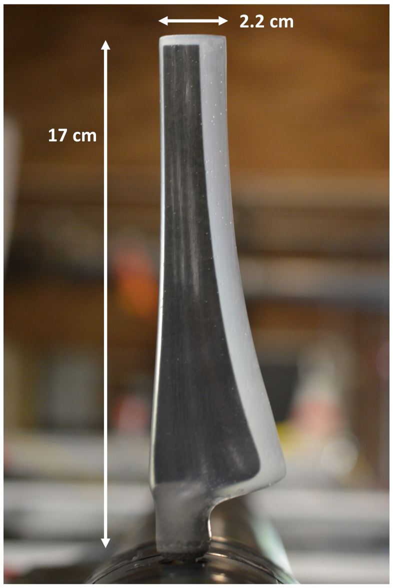

Figure 4.1: Flexible, composite blades composed of a carbon fiber spar (black), to provide the desired bend-twist coupling, and a semi-rigid polyurethane outer (translucent white-grey) to provide the desired blade geometry and hydrodynamic behavior.

4.2.2 Blade Deformation

To improve our understanding of passive adaptive blade deformation during turbine operation, a test was devised to remotely measure the turbine blade's structural response to hydrodynamic loads. A high speed camera (Vision Research, Phantom c641) was positioned below the glass test section of the flume to capture the location and orientation of each passing blade tip (Figure 4.2) at a frame rate of at least 700 fps and a resolution of 1024x1024 or

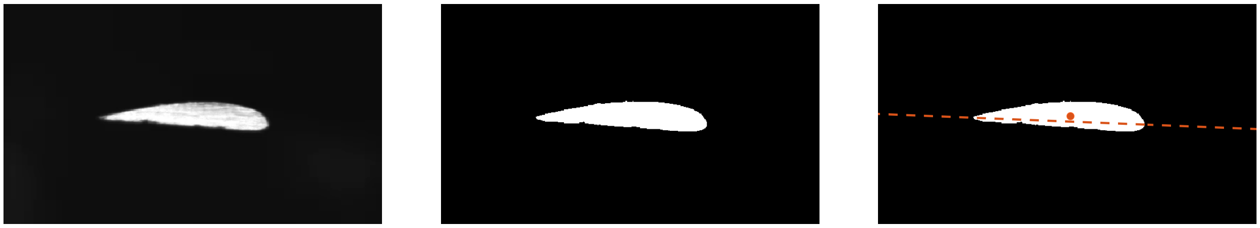

(a) (b) (c)

Figure 4.2: High-speed video of the rotor plane during flume testing was used to calculate tip deflection and twist by (a) identifying a high-contrast object as the blade, (b) binarizing the frame to segment the blade tip from the background, and (c) measuring the position of the centroid and orientation of the major axis in order to calculate tip deflection and twist relative to the unloaded blade.

1024x768 pixels. Blade tips were coated with a reflective chrome paint to increase contrast. Video of at least 15 blade passages was recorded at each tip-speed ratio. During image processing, the frame that most closely aligns the blade in the center of the camera view is compared to an image of the unloaded blade to calculate deflection, $delta$, and twist,$\Delta\phi$, at the blade tip. More specifically, each frame is binarized, converting each pixel above or below a given light intensity threshold to white or black, and the centroid and major axis orientation of the white region, identified as the blade tip, are calculated (Fig. 4.2). The pixel scale is determined by the ratio of the pixel length of the major axis in the reference (stationary) frame to the measured chord length of the physical blade tip. The tip deflection is determined from the displacement of the centroid, while the tip twist is determined from the change in orientation of the major axis, thus fully capturing the coupled deformation shown in Fig. 1.3.

4.2.3 Cauchy Scaling

To understand the effectiveness of Cauchy-scaling in producing similar steady-state performance and blade deformation, we designed two experimental setups with different E and U_∞ that maintained a constant Cauchy number as

$$Ca_A = \frac{\rho_f {U_A}^2}{E_A} = \frac{\rho_f {U_B}^2}{E_B} = Ca_B. \tag{4.2}$$

The first blade used a 7-ply carbon fiber spar and the second blade used a 5-ply carbon fiber spar, both fabricated with a 10° fiber orientation and cast in the same mold to produce identical foil cross-sections. This resulted in two blades with similar bend-twist coupling (Fig. 4.4(c)), but with differing effective elastic moduli, E. While the 7-ply design was an extension of previous work [22], the 5-ply design was selected based on an estimate of bending stiffness matrices for layups of various ply counts using the material properties (E_1, E_2, G_{12}, and ν_{12}) of the carbon fiber listed in Table 4.1. Refer to Appendix E for a full calculation of the bending stiffness matrix and a calculation of the bend-twist coupling parameter, α, as defined in [37].

The choice of inflow velocity for the experiment involved balancing the higher signal-to-noise ratio from higher inflow speeds against higher rotation rates (to maintain λ) that increased vibration in the turbine and support structure. We selected 0.8 m/s for the 7-ply blades, which, as described later in this section, required an inflow speed of 0.55 m/s for the 5-ply blades to maintain Cauchy similarity. To ensure that both tests were conducted in a Reynolds-number independent operational regime, water temperature was increased to 33° C, decreasing viscosity.

Because the material properties of the carbon fiber and urethane are sensitive to temperature, E for both blades was estimated through an in-water zero-inflow load test at 33° C, the same water temperature used for the hydrodynamic tests. With the blade mounted on the turbine and positioned horizontally, calibration weights of 50-100 grams were incrementally added to the blade tip. With the addition of each weight, 3500 samples from the

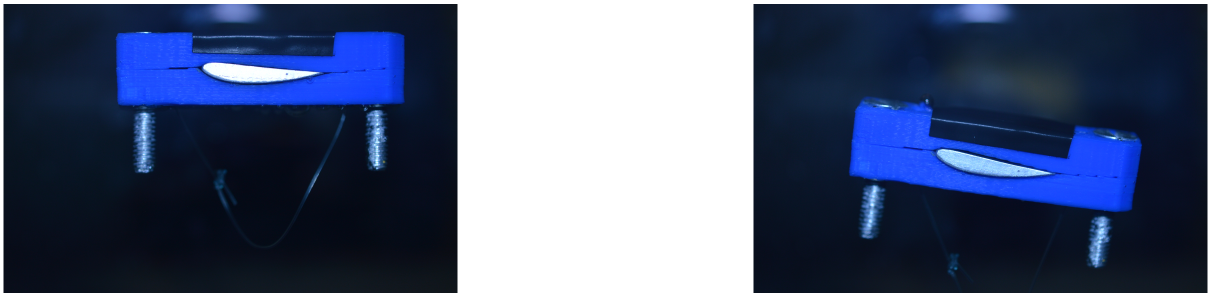

(a) (b)

Figure 4.3: For the in-water static test, deflection and twist are determined from photographs taken in the (a) unloaded and (b) loaded states.

blade load cell recorded the applied force and a photograph was taken to determine the tip deflection and twist relative to the unloaded position (Fig. 4.3). The force and deflection measurements were then used to determine the bending stiffness, treating the blade as a cantilevered beam:

$$EI = \frac{FL^3}{3\delta.}, \tag{4.3}$$

where I is the second moment of inertia, F is the applied load, L is the length of the cantilevered blade, and δ is the deflection at the blade tip. Fig 4.4(a,b) shows twist and deflection as a function of applied load. Because I is a function of blade cross-section and constant for the two blades, a linear regression of the load-deflection response (Fig. 4.4(a)) can be used to estimate the ratio of the elastic moduli for the two blades as:

$$\frac{E_{5ply}}{E_{7ply}} = \frac{(EI)_{5ply}}{(EI)_{7ply}} = \frac{(F/\delta)_{5ply}}{(F/\delta)_{7ply}} = 0.47 \tag{4.4}$$

Consequently, to maintain Ca similarity,

$$U_{5ply} = U_{7ply}\sqrt{\frac{E_{5ply}}{E_{7ply}}} = 0.55\, m/s. \tag{4.5}$$

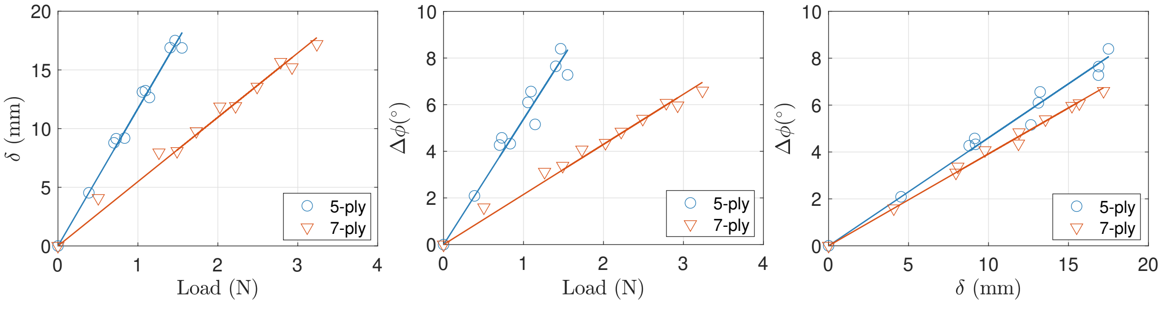

(a) (b) (c)

Figure 4.4: (a) Deflection and (b) twist as a function of applied load for a 7-ply and 5-ply passive adaptive blade with the same 10° fiber orientation. Similarity in (c), twist as a function of deflection, is representative of the matching bend-twist coupling between blades.

Material Property	Value
Longitudinal Young's modulus (parallel to fibers), E_1	115.56 GPa
Transverse Young's modulus (perpendicular to fibers), E_2	9.86 GPa
Shear modulus, G_{12}	4.826 GPa
Poisson's Ratio, ν_{12}	0.335

Table 4.1: Material properties for Hexcel AS4.

Due to the blade-to-blade variability observed in the in-air static mechanical testing of full blades sets (Appendix D) and the need for precise values of bending stiffness and bend-twist coupling to maintain Cauchy number similarity, we used single-bladed tests for this scaling investigation. This allowed us to select one blade from each set that had the closest agreement in bend-twist behavior. This also allowed us to choose inflow velocities that exactly matched the difference in bending stiffness between the blades, rather than an average value that was representative of the three blades in a set.

The comparison of these experiments is carried out under the framework of the non-dimensional parameters for simultaneous hydrodynamic and hydroelastic scaling identified by Young [76]:

- Tip-speed ratio (λ): the same tip-speed ratio range, 2.5-8, is evaluated for the 5-ply and 7-ply blades

- Ratio of bending stiffness to torsional stiffness (EI/GJ) and bend-twist coupling ratio (K_s/EI): Having used the same material at the same fiber orientation for the 5-ply and 7-ply blades, we keep the ratio of effective bending to torsional stiffness and the bend-twist coupling equivalent, with only small variations expected from the use of semi-rigid polyurethane cast. Similarity in the bend-twist coupling is confirmed in Fig. 4.4(c) and Appendix E.

- Froude number and Reynolds number: Froude number could not be matched between tests due to limitations on water height at our facility, and Reynolds number could not be matched due to sensitivity of the blade's material properties to temperature. To stay above Reynolds-independence at both flow speeds, water temperature was increased to the highest possible, 33°C. Re_c ranged from $6.9 \cdot 10^4 - 2.7 \cdot 10^5$, and Fr ranged from 0.23-0.33. Changes in Froude and Reynolds number were not expected to have a significant effect on performance given that good agreement in C_P and C_T has been observed in prior experiments over similar flow conditions [10]. To verify low sensitivity to changes in Fr and Re, we test a rigid blade with the same unloaded geometry at both flow conditions used for the 5-ply and 7-ply tests. The results are discussed in Sec. 4.3.2.

- Density ratio (ρ_s/ρ_f): The density ratio between the solid composite blade and fluid varies between tests due to more polyurethane used in the 5-ply design, but since we are only concerned with scaling the steady-state hydrodynamic and hydroelastic behavior, we neglect density ratio for this study. Practically, up to 20% variation in material density would likely be sufficient even for modeling dynamic behavior [77].

- Cavitation number: Cavitation was not observed in either test case for the 5-ply and 7-ply blades and, thus, cavitation number was considered irrelevant to this experiment.

- Mach number: The turbine was operated in incompressible flow conditions and, thus, Mach number was also considered irrelevant in the context of hydrodynamics.

In summary, physical limitations and assumptions lead us to hold constant four of the nine non-dimensional parameters governing rotor performance in this context: tip-speed ratio, bend-twist coupling ratio, bending to torsional stiffness, and Cauchy number. Since our experiments are conducted in a relatively small channel, we note that blockage ratio is a relevant non-dimensional parameter, and was kept constant between both tests at 35%.

4.3 Results & Discussion

4.3.1 Turbine Performance and Deformation Response for Blades of Varying Fiber Orientation

Figures 4.5(a,b) show coefficients of performance and thrust for each fiber orientation in 0.7 m/s flow. Performance of the rigid, aluminum blades and neutral (0°), composite blades were nearly identical and, therefore, the measurements with rigid blades are not shown here but included in Appendix F. In agreement with [22, 24], we observed that greater bend-twist coupling, produced by further off-axis fibers, corresponded to overall less deflection, more twist, lower C_P, and lower C_T (Fig. 4.5). We observe similar trends from the passive adaptive blades in Figures 4.5(a,b) as we did in Fig. 3.1 for the rigid aluminum blades tested with different preset pitch angles, where the former shed power and load by passively twisting and the latter shed load by actively pitching. Quantitatively, we measure a 10%, 22%, and 38% reduction in C_P from the neutral composite blades at $\lambda = 6$ (peak C_P for the neutral blades) for 2.5°, 5°, and 10° fiber orientations, respectively, and a 8%, 25%, and 38% reduction in corresponding C_T values. Similar to [24, 23], for each blade set, the relative reductions in C_P and C_T are similar. We also observe an overall reduction in peak C_P for blades with a larger bend-twist coupling. This is expected for passive adaptive blades designed with identical geometry in unloaded conditions. We note that prior studies have shown that similar peak C_P values can be achieved for rigid and bend-twist coupled blades by optimizing pre-twist along the blade span [39, 21, 33], but this was not the objective of this study.

Performance and deformation response is observed to be more sensitive to changes in fiber orientation near the neutral, 0° fiber orientation. This is consistent with theoretical and numerical work that predicts a parabolic increase in bend-twist coupling as a function of ply angle, with a peak close to 30° [37, 32]. Conversely, deflection for the 5° and 10° fiber blades were nearly identical. Meanwhile, tip twist varied significantly across all blade sets, even for blade sets with similar deflection. We also note the neutral blades (0° fibers) were still observed to have a small amount of bend-twist behavior (Figure 4.5(d)). Given that this has been observed in previous studies [28, 22], this could be attributed to twist induced by an off-axis center of pressure on the blade. However, variability in spar placement is also likely to contribute to the bend-twist coupling. Blade variability is most recognizable in its impact on twist when comparing, for the 2.5° fiber blade set, the bend-twist behavior measured during static mechanical testing (Appendix D) and the twist in Fig. 4.5(d), both of which show a larger spread in measurements. Interestingly, despite the sensitivity of twist to blade variability, the impact on C_P and C_T is less than our experimental uncertainty, given that there is no noticeable difference in the interquartile range across blade sets. Blade

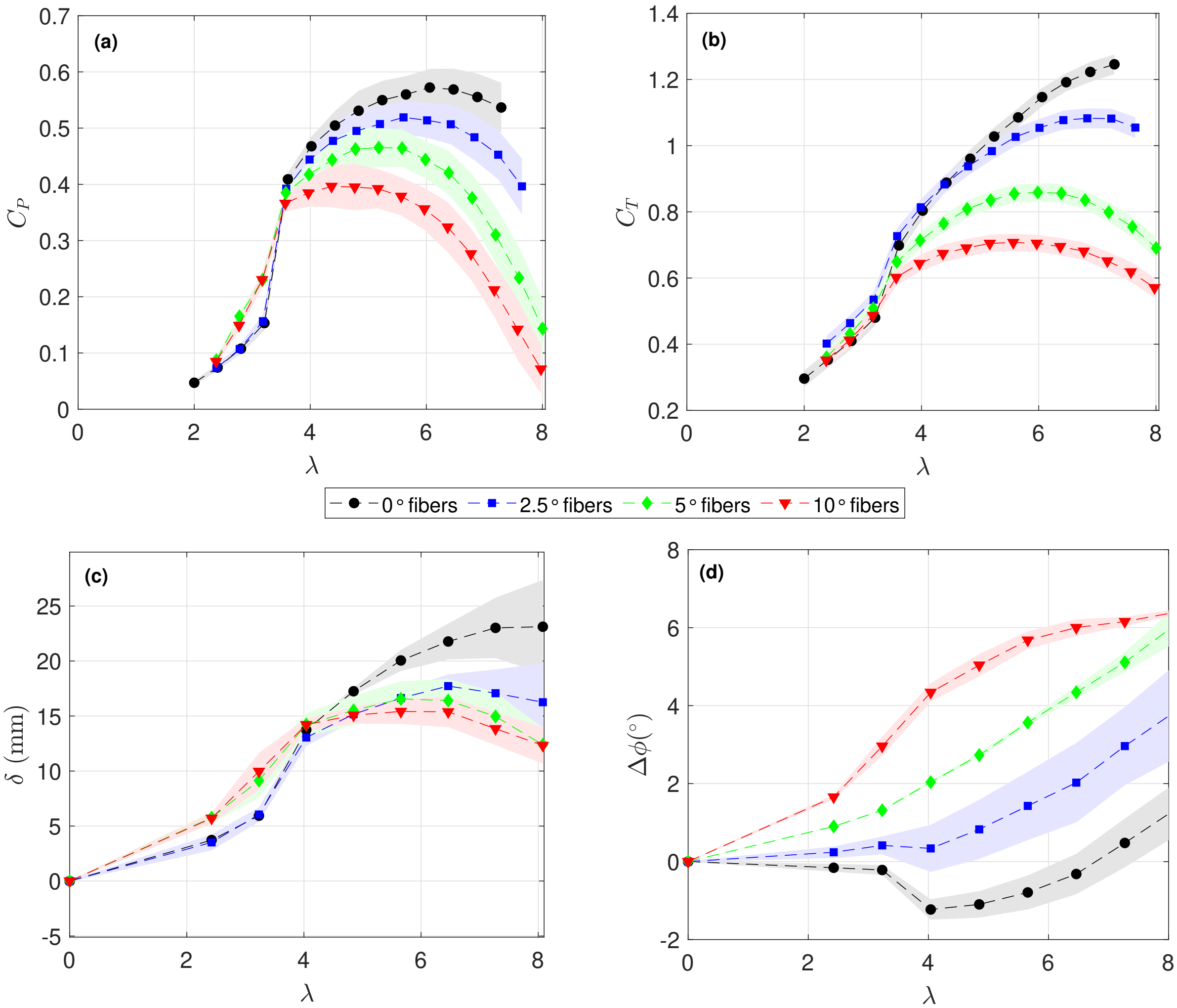

Figure 4.5: Coefficients of (a) performance and (b) thrust as a function of tip speed ratio in 0.7 m/s inflow for each blade set (0°, 2.5°, 5°, and 10° fiber orientation). High-speed video of the passing blades provided measurements of (c) deflection and (d) blade pitch at the tip as a function of tip speed ratio. Shaded regions in each figure represent the interquartile range of measurements.

variability is explored in more detail in Ch. 5.

To reiterate, when the bend-twist coupling is small, there is little or no induced twist to shed load and power. This results in higher efficiency and thrust, and, consequently, greater deflection, none of which are desirable in above-rated flow conditions, where the control objective is to maintain power (i.e., requiring a decrease in efficiency). Conversely, a large load-dependent twist leads to a drastic reduction in C_T at high tip-speed ratios. This is in stark contrast to the high thrust loads observed at high tip-speed ratios when using rigid blades with overspeed control [10], suggesting that when passive pitch control is combined with overspeed control, blade deformation is likely to augment the reduction in efficiency and thrust provided by the overspeed controller and could provide an opportunity for large load reductions and, consequently, reduced material costs and/or increased reliability for marine current turbines. This is further supported by (1) a preliminary result in [21] demonstrating a potential 20% reduction in peak thrust using a passive adaptive strategy with overspeed control over a rigid blade overspeed controller, and (2) the use of a combined passive pitch and overspeed controller by Schottel Hydro [25], although no data on this turbine in above-rated flow conditions has been published. For variable-pitch turbines, the addition of passive pitch control may reduce operating and maintenance costs by reducing the required pitch actuation [35]. Both combined control strategies for applications in above-rated flow conditions are investigated in Chapter 5.

The same trends observed over mid to high tip-speed ratios do not hold true at low tip-speed ratios. Because deformation is load-dependent and blades loads in this tip-speed ratio range are low, only small differences in twist are seen between each blade set (Fig. 4.5(d)). In agreement with [24, 21, 22], this deformation response at low-tip speed ratios appears to be too subtle to significantly affect performance and thrust, though a small increase in C_P is seen for the 5° and 10° fiber blades at $\lambda = 2.4 - 3.6$. Likely due to twist-induced delayed stall, this increase in C_P is consistent with observations over low tip-speed ratios for rigid blades at increased pitch angles (Fig. 3.1). Because of this, passive adaptive blades combined with underspeed control would be ineffective for smoothing low-frequency load fluctuations in above-rated flow conditions.

4.3.2 Cauchy Scaling

Figures 4.6(a,b) show coefficients of performance and thrust for the 5-ply and 7-ply blade in inflow conditions corresponding to Cauchy similarity (Eqn. 4.2). Also shown is the performance of the 7-ply blade at the same inflow velocity as the 5-ply test, which demonstrates the sensitivity of blade performance to a 50% change in Cauchy number. Figures 4.6(c,d) show deflection and twist at the blade tip as a function of tip-speed ratio. As hypothesized, we observe agreement between C_T, δ, and $\Delta\phi$ when Cauchy similarity was maintained, particularly when flow is attached over the entire blade span ($\lambda > 4$), despite dissimilarity in Mach number, Froude number, and density ratio, and for Reynolds numbers that are dissimilar but both within the asymptotic Reynolds-independent regime. More specifically, differences of 0-7% were observed in C_T, δ, and $\Delta\phi$ compared to 50-65% for the 7-ply blade tested at 0.55 m/s and 0.8 m/s. In agreement with the numerical result in [77], our experimental result demonstrates the effectiveness of using Cauchy number to scale passive adaptive marine current turbine blades and model their steady-state hydrodynamics and hydroelastic behaviors in a consistent non-dimensional manner. Confidence in experimental application of scaling laws for passive adaptive blades broadens the impact of past and future lab-scale studies and encourages future work at similar scales, which is often financially accessible to a broader set of research groups.

Unexpectedly, we did not observe a collapse of coefficients of performance between the 5-ply and 7-ply blades 4.6(a). Likely reasons for the disagreement include (1) differences in Reynolds and/or Froude number and (2) a surface defect in the 5-ply blade.

To understand the consequence of changing Reynolds and Froude numbers between 0.55 m/s and 0.80 m/s, we tested a rigid, aluminum blade with the same unloaded geometry at both flow conditions (Fig. 4.7). Excluding the stall region, we observed minimal differences in C_P of 3-8% and differences in C_T of 3-5%. Disagreement over $3.5 < \lambda < 4.5$ is due to partial stall, where flow remains attached over part of the foil and bladespan, while agreement

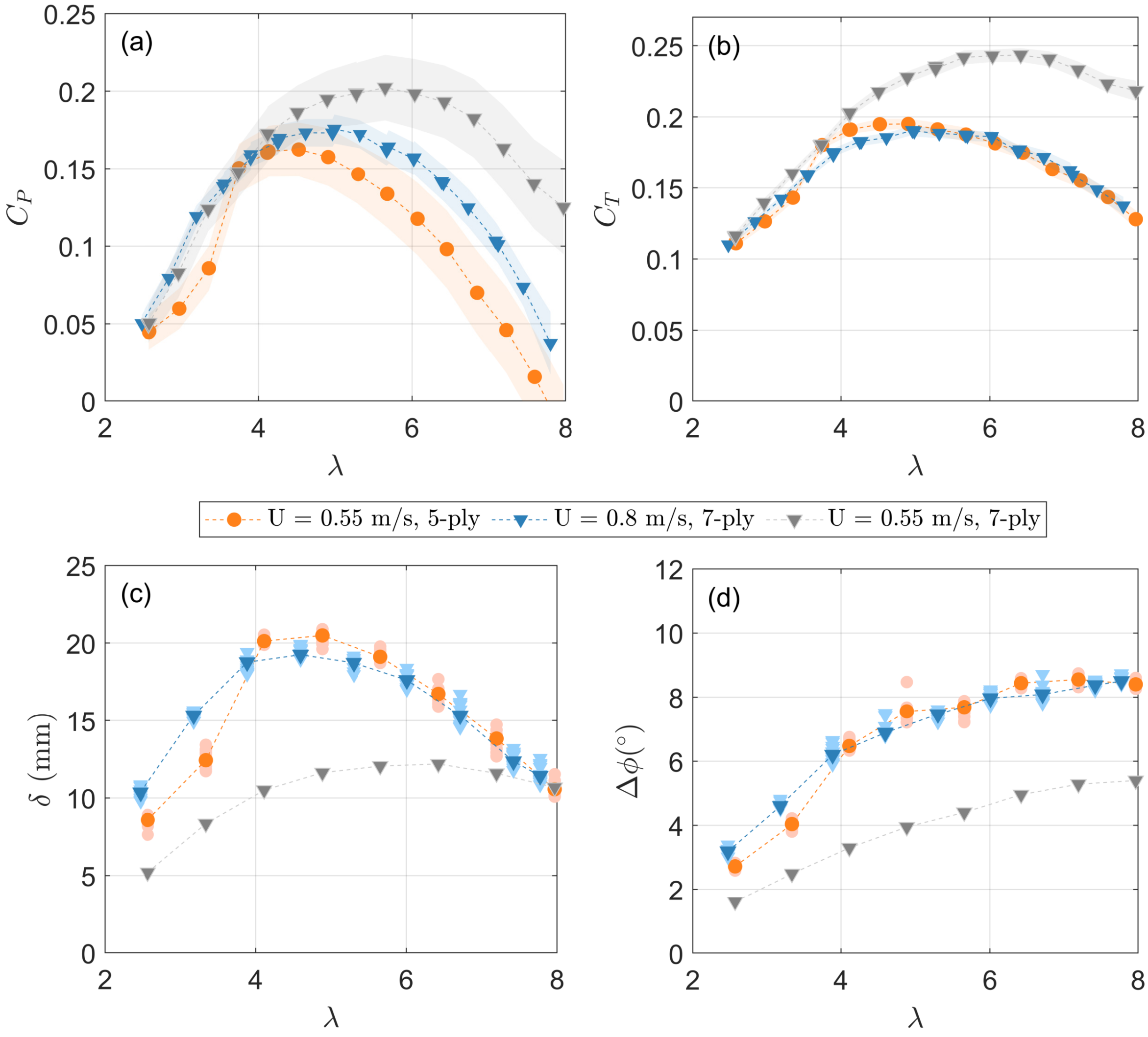

Figure 4.6: Coefficients of (a) performance and (b) thrust as a function of tip speed ratio for a 7-ply and 5-ply composite blade in Cauchy-scaled flow conditions. The 7-ply blade is shown at both flow conditions to provide a reference. High-speed video of the passing blades provided measurements of (c) deflection and (d) blade pitch at the tip as a function of tip speed ratio. Shaded regions in (a,b) represent the interquartile range of measurements while the light orange and blue markers in (c,d) represent measurements from individual blade passages.

resumes over $\lambda < 3.5$ when the blade is in full stall. But for $\lambda > 4.5$, C_P and C_T are generally insensitive to changes in the Reynolds and Froude numbers. Because the differences in C_P are small in comparison to the disagreement between the composite blades, we do not believe that the C_P differences in the Cauchy similitude experiment can be attributed to variation in the Reynolds and/or Froude numbers. We hypothesize that the source of the disagreement in C_P is a small (7 mm) surface defect in the urethane on the 5-ply blade near the mid-span and mid-chord of the blade. The defect, which created an uneven surface, may have caused early flow separation and, consequently, decreased power production, while having little effect on thrust. The experiment will be repeated to confirm this hypothesis.

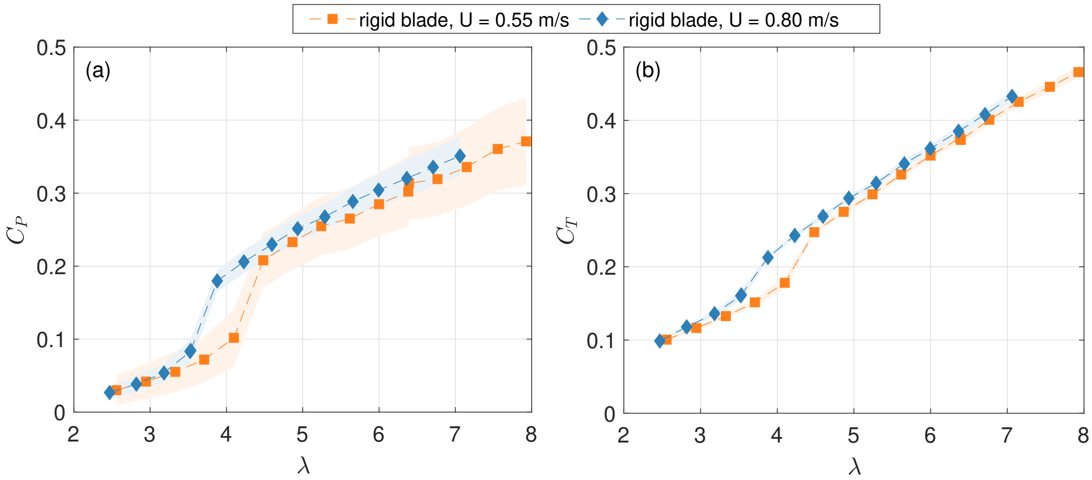

Figure 4.7: Coefficients of (a) performance and (b) thrust as a function of tip speed ratio for a rigid blade with the same unloaded geometry of the 5- and 7-ply composite blades. Shaded regions represent the interquartile range, which is smaller than the size of the markers in (b).

4.4 Conclusion

We fabricated 17 cm composite, passive adaptive turbine blades with 0°, 2.5°, 5°, and 10° fiber orientations, then tested these in a recirculating flume using a 0.45-m diameter axial-flow current turbine. To summarize our observations of blade loading and deformation from the first part of our study:

- At $\lambda = 6$ (maximum C_P for an equivalent rigid or neutral composite blade), a 10%, 22%, and 38% reduction in C_P was calculated for 2.5°, 5°, and 10° fiber blades relative to the neutral, 0° fiber blades.
- At $\lambda = 6$, a 8%, 25%, and 38% reduction in C_T was calculated for 2.5°, 5°, and 10° fiber blades relative to the neutral, 0° fiber blades.
- Even a small bend-twist coupling limited thrust at high tip-speed ratios, making passive adaptive blades an attractive choice for use with an overspeed controller in order to regulate power in above-rated flow conditions.

In the second part of our study, we fabricated an additional 10° fiber blade with a decreased bending stiffness to explore the effectiveness of Cauchy-scaled passive adaptive blade experiments for modeling the blade's steady-state hydrodynamic and hydroelastic response. We successfully demonstrated agreement in thrust coefficient, blade deflection, and blade twist between blades with equivalent bend-twist coupling, but with different bending stiffness, and tested in different flow conditions such that Cauchy number was held constant between experiments. While we observed moderate disagreement in the power coefficient, we believe that the most likely explanation is a surface defect on one blade. Given this, Cauchy-scaling appears a viable approach to extending studies of passive adaptive blades at laboratory-scale to larger-scale applications.

A worthwhile next step is to repeat the Cauchy-scaled experiments presented in this chapter to confirm the ability to scale C_P. We plan to recast the blade with the visible surface defect, and repeat the experiments in the fall of 2022 before submitting this work for publication. A more challenging, but valuable, area of anticipated experimental study would be investigating scaling of both the steady-state and dynamic passive adaptive blade response. Ideally, this experiment could be conducted for different sized blades to simultaneously validate the effectiveness of Cauchy-scaling passive adaptive blades of different geometric scales.

Chapter 5

PASSIVE BLADE PITCH CONTROL

Using the knowledge gained about passive adaptive blade response in Ch. 4, we now expand the rigid blade results presented in Ch. 3 to consider the role of passive pitch strategies in reducing loads relative to other Region III control strategies. We present a comprehensive experimental comparison between four Region III control strategies implemented in quasi-steady inflow fluctuating above the rated speed for a variable-speed, variable-pitch turbine: (1) passive adaptive blades combined with overspeed control, (2) passive adaptive blades combined with active pitch control, (3) rigid blades combined with underspeed control, and (4) rigid blades combined with active pitch control. We compare measured turbine loads across each case, along with observations of *in situ* blade deformation, using methods from Sec. 4.2.2, to interpret the performance of each strategy. A version of this chapter will be submitted for publication in the *Journal of Ocean Engineering and Marine Energy.*

5.1 Methods

5.1.1 Controllers

In total, four control strategies were experimentally implemented:

- passive adaptive blades with overspeed control
- passive adaptive blades with active pitch control
- rigid blades with underspeed control
- rigid blades with active pitch control

The 5° fiber blade set from Ch. 4 was used for the controllers using passive adaptive blades. Each controller was implemented in a Reynolds-independent regime, assuming a rated flow speed of 0.7 m/s as the flow was increased linearly from 0.7 to 0.8 m/s over 10 minutes. The relatively long period was chosen to mimic low-frequency fluctuations like those observed during a tidal cycle. Consequently, our experimental results are not indicative of trade-offs that may be associated with controller implementation under high frequency load fluctuations (e.g., coherent turbulence [26] or wave-current interaction [24]). We note the exclusion of two control strategies from experimental implementation: (1) passive adaptive blades with underspeed control and (2) rigid blades with overspeed control. The reasons for these omissions are discussed in Secs. 5.2.1 and 5.3.1.

Each controller used the calculated power ($Q\omega$) as an input to determine an appropriate change in blade pitch or rotation rate to maintain a constant power output (Fig. 3.3). To reduce noise on the input signal to the controller, a moving average filter of 1000 samples (i.e., 20 seconds or 30-80 revolutions, depending on rotation rate) was applied to the calculated mechanical power. This relatively long averaging window ensured the controller would respond only to low-frequency flow fluctuations.

The active pitch controllers changed blade pitch white holding rotation rate constant, while the speed controllers changed the turbine rotation rate while holding blade pitch constant. The initial rotation rates selected for the flexible and rigid blades correspond to the peaks in the $C_P(\lambda)$ curves in Fig. 5.1(a). Different preset pitch angles were used between the flexible and rigid blades to achieve matching peaks in efficiency (52%) at the rated inflow speed, which ensures that both blade types achieve the same power output at the rated flow condition. Despite the identical blade geometry, moderate deformation at the rated flow condition changes the response of the passive adaptive blades relative to the rigid blades. Note from Fig. 5.1 that the difference in β also resulted in a 0.4 difference in the optimal tip-speed ratio between the rigid and flexible blades. In practice, identical performance could be achieved at the rated condition by incorporating varying degrees of pre-twist along the span of the passive adaptive blade such that when the blade is loaded at the rated speed, the deformed blade is identical in geometry and preset pitch angle to the rigid blade [21, 33]. The proportional gains selected for each controller were tuned in an *ad hoc* manner to yield acceptable performance (i.e., deviation of the measured power output from the rated power that is comparable to the deviation from the mean observed during constant inflow experiments). To more easily compare rotor loads between each control case, the thrust and torque measurements were normalized by their values at the rated operating condition.

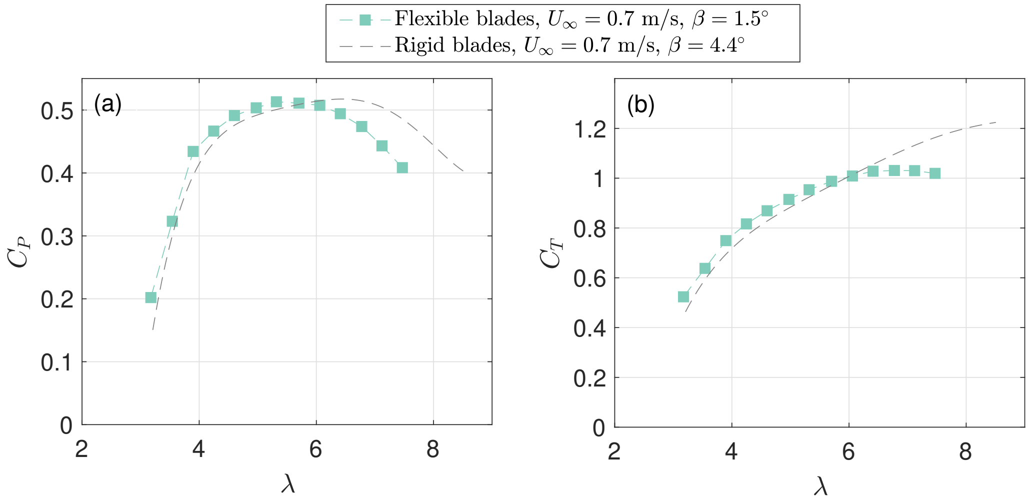

Figure 5.1: Coefficients of (a) performance and (b) thrust in 0.7 m/s flow for the flexible and rigid blades. The preset pitch angles of both blades sets were adjusted to achieve matching peaks in efficiency and power output. Pitch angle, β is given relative to the plane of rotation.

5.2 Results

5.2.1 Comparison of Turbine Loads Between Controllers

Figure 5.2 shows, for the four control tests, the time series of linearly increasing inflow and the associated changes in tip-speed ratio, controlled rotation rate or blade pitch, and thrust and torque normalized by the rated condition. Overspeed control with the rigid blades was not tested due to experimental limitations on rotation rate described in [10], while overspeed control with the flexible blades was feasible since the twist of the flexible blades resulted in reduced rotation rate requirements to achieve the desired decrease in efficiency. Underspeed control with the flexible blades was also excluded from experimental tests since operating at low tip-speed ratios results in low thrust loads and, consequently, limited blade deformation, which we discuss further in Sec. 5.3.1. Each controller succeeded in maintaining a constant power output with a standard deviation of 2-3% relative to the rated power, which is comparable to the 1-2% relative standard deviation observed during constant inflow experiments over the same tip-speed ratios with the same temporal filtering. For comparison, the power output would exceed the rated power by 45% if rigid blades were used and no control action was taken to regulate power output. As a reminder, while Figs. 5.2(b,c,d) show changes in λ, β, and ω from the rated condition, the initial tip-speed ratios (5.7, 6.1), blade pitches (1.5°, 4.4°), and rotation rates (2.8 rps, 3.0 rps) at the rated speed of 0.7 m/s correspond to the peaks in efficiency in Fig. 5.1(a) for the flexible and rigid blades. The trajectories through $C_P(\lambda)$ and $C_T(\lambda)$ space as inflow increases are described in more detail for each control test in Secs. 5.3.1 and 5.3.2.

For controllers employing active pitch, we observe no significant differences in $\Delta\lambda$, $\Delta\beta$, T', or Q', regardless of whether rigid or flexible blades are used. Recall that $\Delta\beta$ refers to the change in pitch angle via the blade motors and does not include any change in twist of the flexible blades. This experimental result supports a computational study by Motley and Barber [18], which predicted identical thrust loads in Region III for both passive adaptive blades and rigid blades combined with active pitch control due to a decrease in the load-dependent twist of the passive adaptive blade. In contrast, we observe a 12% increase in normalized thrust and a 36% decrease in normalized torque for the flexible blades combined with overspeed control. This is in stark contrast to the 127% increase in thrust observed in Ch. 3 for a set of rigid blades with similar geometry tested with overspeed control [10]. While the rigid blades with underspeed control avoid an increase in normalized thrust, Fig. 5.2(f) shows that this comes at the cost of a 50% increase in torque from the rated condition for this turbine. Performance of both passive pitch controllers is discussed further in Secs.

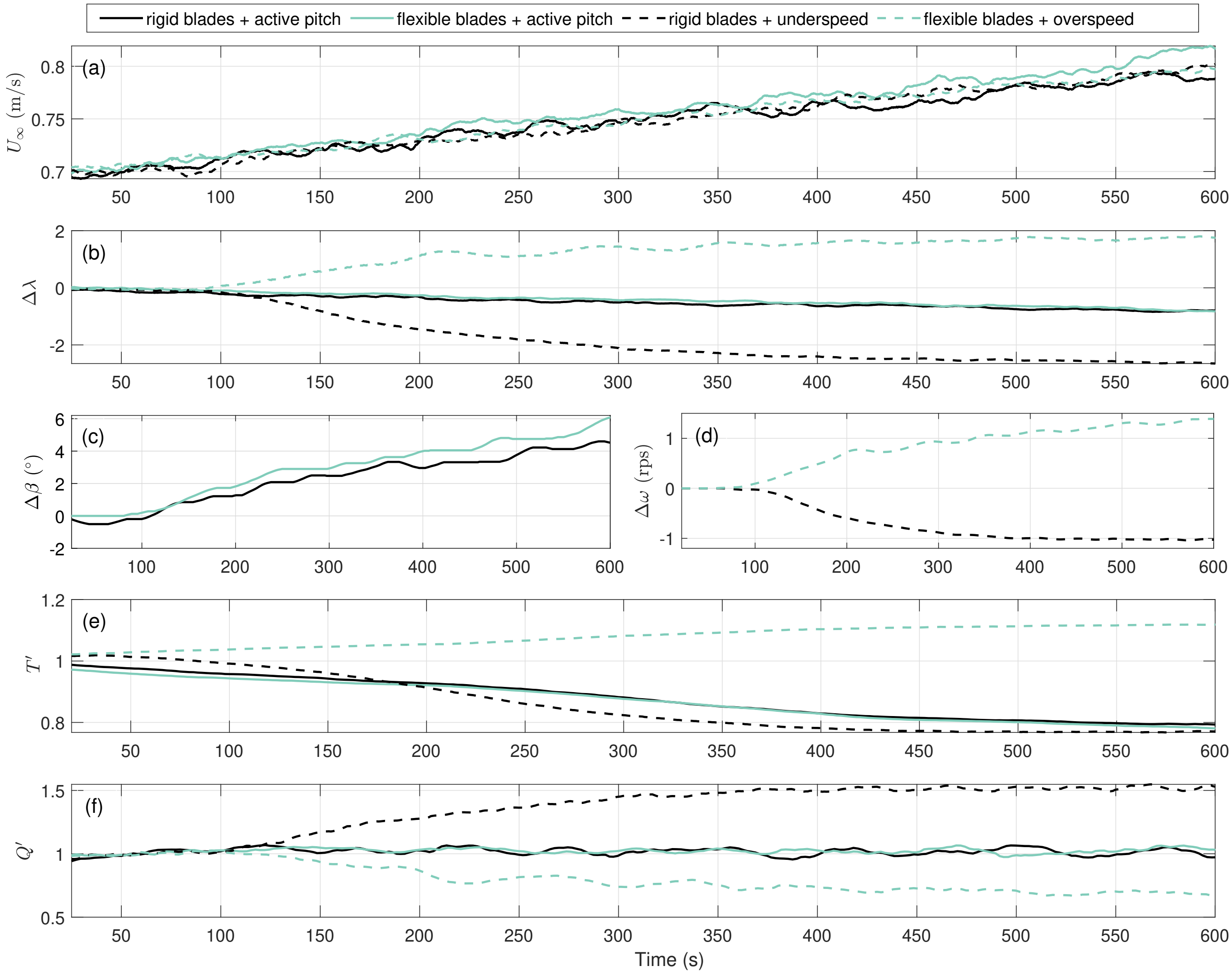

Figure 5.2: Four control strategies were implemented in linearly increasing inflow from the rated speed of 0.7 m/s to 0.8 m/s over 10 minutes. Shown for each controller is the time series of (a) free-stream velocity, U_∞, (b) change in tip-speed ratio from the tip-speed ratio corresponding to peak efficiency, $\Delta\lambda$, (c,d) change in blade pitch or rotation rate depending on whether active pitch or speed control is being used, (e) thrust normalized by the rated condition, and (f) torque normalized by the rated condition. The minor deviations in inflow velocity between the tests are associated with low-frequency resonance between the pumps and test section.

5.3.1 and 5.3.2.

5.2.2 Comparison of Blade Deformation Between Controllers

Following the method described in Sec. 4.2.2, the tip deflection, δ, and tip twist, $\Delta\phi$, of the passive adaptive blades observed during each control case is reported in Fig. 5.3. Each data point is an average over 45 blade passages. Note that the twist values shown in Fig. 5.3(b) for the active pitch control case describe only the load-dependent twist of the blade tip. Pitching of the blades due to motor actuation alone is captured in Fig. 5.2(c).

We observed blade deflection and twist increase with inflow velocity when flexible blades were combined with overspeed control. Conversely, we observed deflection decrease with increasing inflow when flexible blades were combined with active pitch control. This corresponded to a slight decrease in twist over the course of the control test, in agreement with the simulations in [18].

5.3 Discussion

5.3.1 Passive Adaptive Blades with Overspeed Control

We have demonstrated the effectiveness of a passive pitch control strategy combined with overspeed control in both power regulation and load reduction while operating in Region III. To better understand blade behavior during the control test, we show C_P, C_T, δ, and $\Delta\phi$ as a function of tip-speed ratio in the left panel of Fig. 5.4 for the passive adaptive blades in both 0.7 m/s flow and 0.8 m/s flow. When the flexible blades are used with overspeed control in linearly increasing inflow from 0.7 to 0.8 m/s flow, blade performance and blade deformation is understood to shift between these characteristic curves corresponding to the initial and final operating conditions. With the flexible blades, we see lower C_P and C_T relative to the rigid blades at high tip-speed ratios for both flow speeds and a trend of decreasing C_P and C_T with higher U_∞ as the blades deflect. This is caused by the increased twist (Fig. 5.4(d)) at higher λ and U_∞, which decreases the angle of attack. The sharper drop-off in C_P and

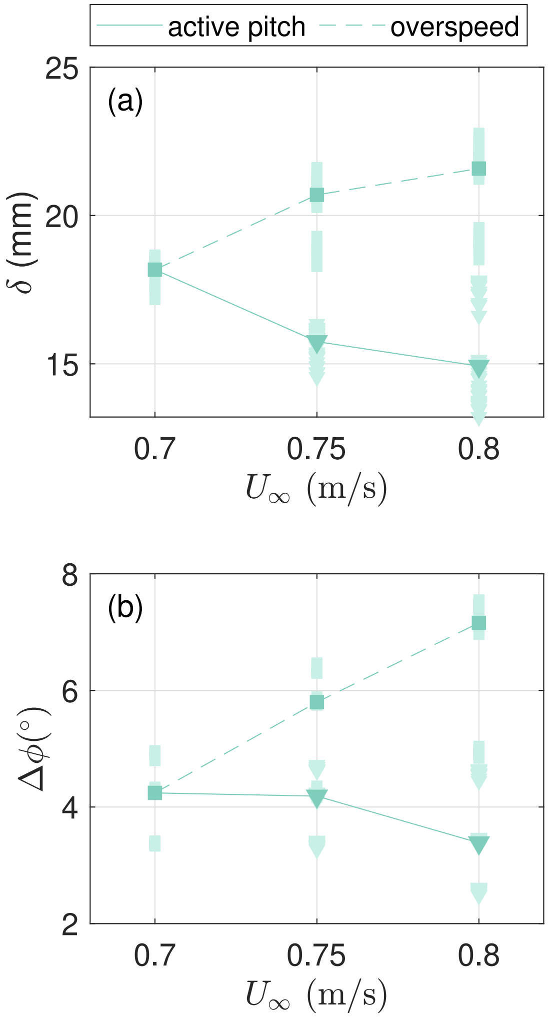

Figure 5.3: (a) Deflection and (b) twist of the composite blades observed when implementing passive adaptive blades with active pitch control and passive adaptive blades with overspeed control in linearly increasing inflow from the rated speed of 0.7 m/s to 0.8 m/s. Deflection and twist measurements from individual blade passages are plotted in light teal while the darker colored plots referenced in the legend indicate the average measurement.

C_T relative to the rigid blades results in smaller increases in ω required from the overspeed controller, thus improving load reduction benefits in Region III for passive adaptive blades (Fig. 10(e,f)).

Relative to our prior study with rigid blades [10], passive adaptive blades with overspeed control achieves the desired power regulation with 50% less thrust. For comparison, a preliminary computational result presented in [21], albeit with blades of differing geometry based on S814 airfoils, indicated a 20% reduction in thrust for their bend-twist coupled blades relative to their rigid blades combined with overspeed when inflow was 30% above the rated condition. It is not surprising that our result indicates a greater load reduction for a smaller increase in flow speed given the high blockage ratio (35%) at our facility, the effects of which are discussed in Sec. 5.3.4.

Quantitatively, load reduction benefits of a passive pitch control strategy combined with overspeed control may vary from those observed in this study as function of blade geometry. The rigid blade performance in Fig. 5.4(a) (solid grey line) has a broad peak in C_P, which requires relatively high tip-speed ratios to maintain constant power as inflow increases. This makes the same control strategy implemented with a passive adaptive blade much more advantageous for reductions in thrust. The stiffness and bend-twist coupling of the passive adaptive blade design is also impactful to blade loads in Region III. A blade that is too load-dependent can not be optimized for the same peak efficiency of a rigid blade of the same scale but may see more desirable load reductions in Region III, while a blade that is too stiff will not sufficiently deform to shed power. Since the flexible and rigid blades used in these tests shared the same unloaded blade geometry, an experiment using an optimized passive adaptive blade design may yield different load reduction benefits.

Due to the bend-twist coupling, we generally expect an increase in deflection to correspond to an increase in twist. But Fig. 5.4(c,d) shows that increased tip deflection does not map directly to increased tip twist. In fact, the observed deflection is not uniquely defined by inflow speed and tip-speed and, at high tip-speed ratios, tip twist continues to increase, even as tip deflection decreases, as was also seen in the deformation evaluation in [29]. We

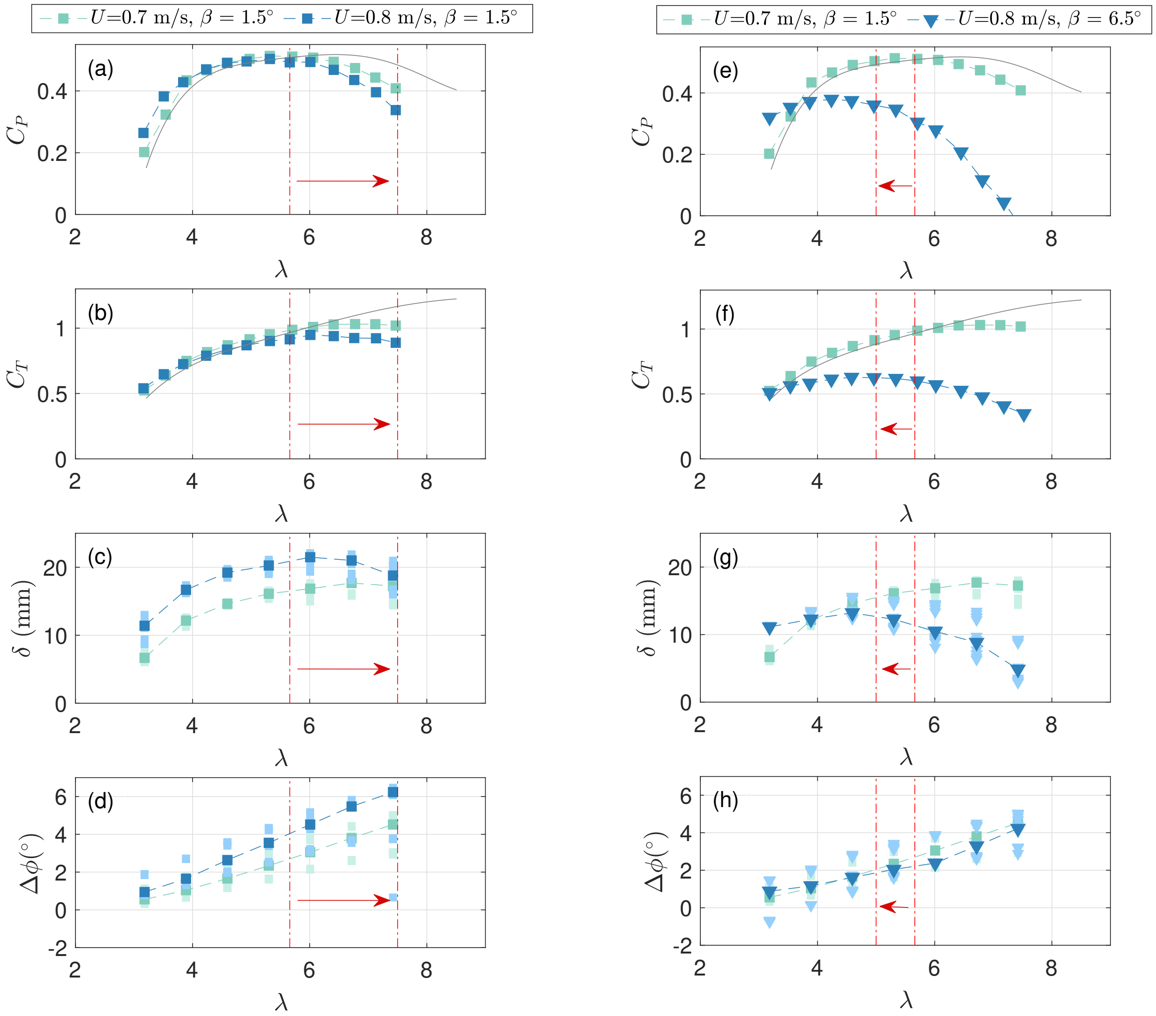

Figure 5.4: As the overspeed controller (left) and active pitch controller (right) combined with passive adaptive blades are implemented in linearly increasing inflow from the rated speed of 0.7 m/s to 0.8 m/s, blade performance and deformation can be understood to shift between the characteristic curves corresponding to the initial and final operating conditions: (a,e) coefficient of performance, (b,f) coefficient of thrust, (c,g) tip deflection, and (d,h) tip twist as a function of tip-speed ratio. Deflection and twist measurements from individual blade passages are plotted in light blue and light teal while the darker colored plots referenced in the legend indicate the average measurement. Rigid blade performance, tested with $\beta = 4.4°$ to achieve equivalent peak performance, are shown in solid grey. Rigid blade performance is independent of velocity in the 0.7 m/s to 0.8 m/s range.

hypothesize this is because the location of the spanwise and chordwise center of pressure on the blade is a function of tip-speed ratio which, in turn, affects the magnitude of tip deflection and twist. Further studies that resolve deflection and twist along the entire blade span, as well as pressure contours, would be needed to explore and confirm this hypothesis.

Finally, we emphasize the similarity in C_P and C_T at low-tip speed ratios between rigid and flexible blades (Fig. 5.4(a)). This is because, at lower tip-speed ratios, thrust loads are insufficient to appreciably deform the blade. For this reason, a passive pitch strategy combined with underspeed control would be ineffective in Region III and was, therefore, not experimentally tested. Furthermore, the slight increase in twist observed at low tip-speed ratios (Fig. 5.4(d)) from 0.7 m/s to 0.8 m/s actually increases C_P (Fig. 5.4(a)). This is because increasing twist decreases the angle of attack, thereby delaying stall and, contrary to Region III control objectives, increasing efficiency.

5.3.2 Passive Adaptive Blades with Active Pitch Control

For low-frequency fluctuations above the rated flow speed, we observed that the combination of passive and active blade pitch control is ineffective at reducing thrust, torque, or pitch actuation relative to active pitch control with rigid blades. To better understand the underlying reasons for this, we show C_P, C_T, δ, and $\Delta\phi$ as a function of tip-speed ratio in the right panel of Fig. 5.4 for the passive adaptive blades in both 0.7 m/s and 0.8 m/s flow. When the flexible blades were used with active pitch control in linearly increasing inflow, blade performance and blade deformation is understood to shift between these characteristic curves corresponding to the initial (0.7 m/s, $\beta = 1.5°$) and final (0.8 m/s, $\beta = 6.5°$) operating conditions. Over the highlighted tip-speed ratio range ($\lambda = 5.7$ to $\lambda = 5.0$), corresponding to the control test, we observe a decrease in deflection and twist, as is consistent with Fig. 5.3. Since the flexible blades experience relatively low thrust loads over tip-speed ratios below that corresponding to peak C_P, they do not twist sufficiently for power shedding and the active pitch controller is engaged to shed power. More specifically, when the blades are actively pitched, C_P and C_T drastically drop (Fig. 5.4(e,f)) and the tip deflection and twist of the flexible blades decrease in response to the lower thrust load. In conclusion, a combined passive and active pitch control strategy can still regulate power with load reductions (Fig. 5.2) but it does not make use of the bend-twist coupling for power shedding over the low-frequency load fluctuations considered in this study and is, therefore, equivalent to using active pitch control with rigid blades. However, we recognize that it would be worthwhile to study this combined control strategy for its effectiveness in smoothing both low- and high-frequency loads. That is, a strategy where the active pitch controller regulates power over longer time scales and the twist in the passive adaptive blades can potentially respond to cyclic or stochastic loads (e.g., due to shear flow, tower shadow, or turbulence). Such a controller was studied computationally for a wind turbine by Botasso *et al.* [35] which showed a reduced actuation rate from the blade motors when experiencing high frequency fluctuations (i.e., with a period, $T = 5$ seconds). This is significant given that the desired pitch rates for active pitch controllers used with rigid blades may not be attainable for marine current turbines.

5.3.3 Effects of Reynolds Number

Re_c, as defined in Eqn. 2.1, ranged from $4.9 \cdot 10^4$ to $9.9 \cdot 10^4$ for the control tests. Reynolds-independence was confirmed above $Re_c > 5 \cdot 10^4$ by comparing rigid blade performance at 0.7 m/s and 0.8 m/s. In many lab-scale experiments, differences in Reynolds number can be neglected when operating at or above a critical Reynolds number, beyond which flow behavior is dominated by inertial forces and relatively independent of viscosity. While each controller was implemented in a Reynolds-independent regime, we briefly consider the potential for load reductions using passive adaptive blades combined with overspeed control when operating in a Reynolds-dependent regime. For rigid blades, increasing the free-stream flow (i.e., increasing the Reynolds number) when the turbine is operating below Reynolds-independence will increase the overall efficiency and thrust, though efficiency is more sensitive than thrust to changes in Reynolds number [59]. A passive adaptive blade will experience a similar effect in increasing inflow, depending on its bend-twist coupling and stiffness. The greater twist caused by the increase in thrust load from the free-stream flow will act to decrease efficiency and thrust while the increase in Reynolds-number will act to increase efficiency and thrust. Consequently, while a combined passive and overspeed control strategy implemented in a Reynolds-independent regime must increase blade twist and rotation rate to counter an increase in kinetic energy at higher flow rates and maintain power, the same control strategy implemented in a Reynolds-dependent regime must account for both the increase in kinetic energy and the increase in C_P expected at higher Reynolds numbers. This will likely require increased rotation rates from the overspeed controller to augment the decrease in angle of attack provided by the passive twist and, thus, higher thrust loads relative to a controller implemented in a Reynolds-independent regime.

We note that Figure 5.4(a,b) could be interpreted as the passive adaptive blades being in a "Reynolds-dependent" regime since the increase in U_∞ corresponds to an increase in Re_c and does change the characteristic performance. However, given that the rigid blades over the same range of U_∞ are Reynolds-independent [10], the differences in C_P and C_T for the flexible blades are likely caused by changes in the Cauchy number. The difference in Cauchy number at 0.7 and 0.8 m/s (27%), due to a change in dynamic pressure on the blade, is expected to change the blade deformation and, consequently, C_P and C_T.

5.3.4 Effects of Blockage

When a turbine's rotor swept area is large relative to the cross-sectional area of the channel, more flow is forced through and around the rotor plane. This phenomena increases C_P and C_T relative to the same rotor in unconfined flow. Blockage corrections are commonly used to estimate unconfined turbine performance from confined performance data. Here, we apply the blockage correction presented by Houlsby *et al.* in [62] to our experimental data (Fig. 5.4(a,b)). As shown in Fig. 5.5, the blockage correction significantly decreases C_P and C_T relative to the experiments in confined flow. Based on the corrected data, in unconfined flow, our Region III controllers would need to reduce turbine efficiency from 35% (at the onset of Region III operation) to 24% to compensate for a 14% increase in inflow (i.e., 0.7 m/s to 0.8

m/s). This would require an increase from $\lambda = 4.5$ to $\lambda = 6.7$ for the flexible blade overspeed controller and an increase from $\lambda = 4.5$ to $\lambda = 7.2$ for the rigid blade overspeed controller. The combination of the lower tip-speed ratio requirement and lower thrust coefficient for the flexible blade overspeed controller means that the thrust would be 27% lower than for the rigid blades (compared to the 50% reduction observed in confined experiments). This result is more in line with the load reductions predicted by Murray *et al.* [21]. Overall, this suggests that significant load reduction is still likely in unconfined flow, but also that passive pitch control strategies may be more advantageous when turbines are operating in confined flow. However, given the range of uncertainty in blockage corrections [59], a similar experiment to that presented here in unconfined flow would be necessary to confirm this result.

We note that blockage corrections assume C_P and C_T are independent of U_∞. However, this is not the case for bend-twist coupled blades due to changes in the Cauchy number. The Houlsby *et al.* correction, like others assessed in [59], uses actuator disk theory to estimate the unconfined free-stream velocity (U') that would produce the same velocity through the rotor plane as U_∞ in confined flow. The power and thrust coefficients that could be expected in unconfined flow are then determined by

$$C_P{}' = C_P \left(\frac{U_\infty}{U'}\right)^3 \tag{5.1}$$

$$C_T{}' = C_T \left(\frac{U_\infty}{U'}\right)^2 \tag{5.2}$$

Since increasing the free-stream velocity will increase twist, thereby decreasing C_P and C_T, a larger unconfined flow speed, U', than that predicted by the blockage correction would be needed to produce the same thrust through the rotor plane in unconfined flow. It follows from Eqns. 5.1 and 5.2, that an underpredicted U' yields an overprediction of unconfined C_P' and C_T' values for passive adaptive blades. This indicates that we would likely observe greater load reductions in unconfined flow when using passive adaptive blades than those suggested by the blockage corrected performance in Fig. 5.5. Experiments conducted in confined and unconfined flow would be greatly beneficial in assessing the significance of the blockage correction error for bend-twist coupled blades.

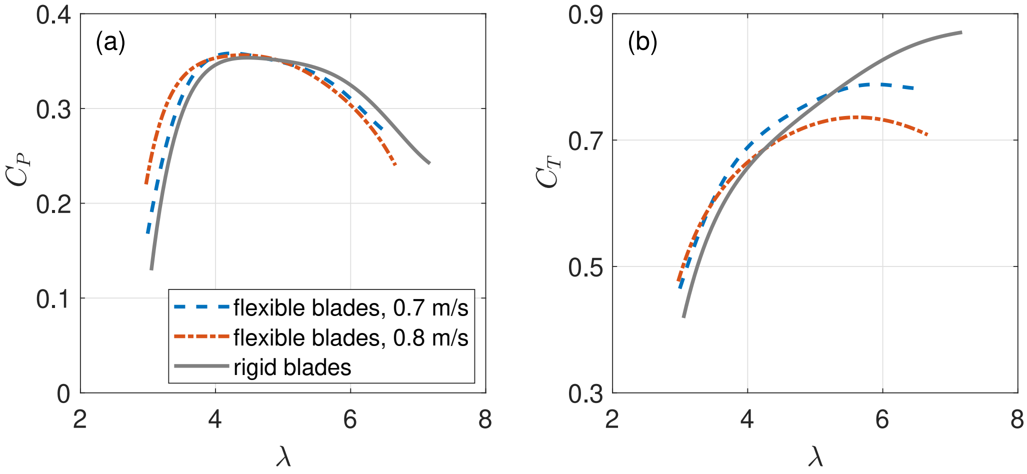

Figure 5.5: Blockage-corrected characteristic performance for (a) power and (b) thrust coefficients as a function of tip-speed ratio.

5.3.5 Blade Variability

While design choices were made to improve repeatability between blades, manual aspects of the fabrication resulted in some amount of variability between blades (Appendix B). The CT scans used to design the rigid aluminum blades were also used to observe error in spar positioning during root placement and casting, which contributes to error in the fiber angle orientation and resulting bend-twist coupling. Figure 5.6 shows CT scans for a set of 0° fiber blades near the blade tip and calculations of horizontal and vertical variations in spar placement within the polyurethane cast. The maximum variation in horizontal placement observed here corresponds to a 5° error in spar alignment with the blade's axis of rotation. We considered the potential effect on trailing edge deformation if variation in spar placement caused differences in the stiffness of the trailing edge but could see no measurable difference in camber.

This blade variability is apparent in the deviation between average deflection/twist and individual deflection/twist measurements from each blade passage (Fig. 5.4(c,d,g,h)). At any given tip-speed ratio, we observe individual measurements are clustered into groups of three, which we presume correspond to each of the three blades. We observe a spread of <1 mm in deflection and $< 0.2°$ in twist around each cluster corresponding to a blade. The spread within a cluster is significantly less than the overall spread in deflection and twist at each tip-speed ratio, confirming that the uncertainty in these measurements is dominated by blade-to-blade variability in fabrication, not measurement error. At the highest tip-speed ratio tested, the spread in deflection and twist measurements reached 5 mm and 2.1°, respectively.

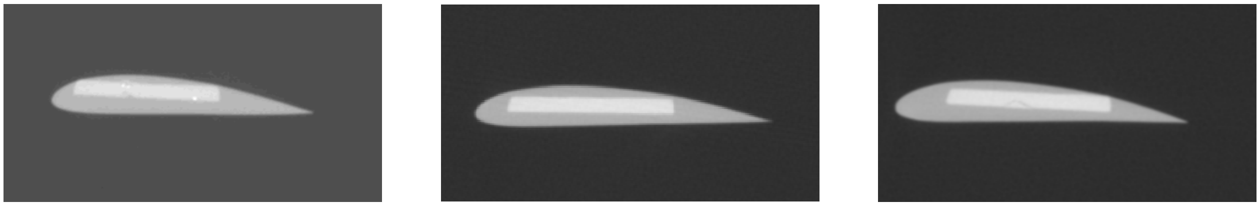

(a) Blade 1 shows errors in horizontal and vertical spar placement of 0.52mm and 0.46mm, respectively.

(b) Blade 2 shows errors in horizontal and vertical spar placement of 0.10mm and 0.05mm, respectively.

(c) Blade 3 shows errors in horizontal and vertical spar placement of 1.48mm and 0.27mm, respectively.

Figure 5.6: CT scans of three 0° fiber blades showing variations in spar placement within the polyurethane cast.

5.4 Conclusion

We comprehensively demonstrated the implementation, and quantified the performance, of active and passive Region III control strategies for an axial-flow marine current turbine. The experimental results show that using flexible, passive adaptive turbine blades combined with overspeed control offers power regulation at reduced rotor loads relative to fixed-pitch, rigid blade control strategies. Overall, active pitch control achieves the necessary power regulation in Region III with the lowest thrust and torque on the rotor. However, a strategy combining passive adaptive blades with overspeed control produced only moderate increases in thrust with a substantial decrease in rotor complexity and potential failure modes.

This study also detailed a technique for obtaining measurements of blade deformation during turbine operation, data rarely available in published studies of passive adaptive turbine blades. An important consideration for material selection and achieving appreciable power shedding, we reported deflection and twist at the blade tip over a range of flow speeds and tip-speed ratios relevant to the passive pitch control strategies implemented in this study. Further exploration of passive pitch control and its application was recommended through experimental studies of high-frequency load mitigation, chordwise and spanwise pressure distributions, and an assessment of blockage corrections for passive adaptive blades.

Chapter 6

CONCLUSIONS & FUTURE WORK

6.1 Conclusions

A significant improvement in the reliability of current turbine technology is critical to reducing operation and maintenance costs and accelerating adoption of this technology. Avoiding blade and generator failure requires a comprehensive understanding and accurate predication of hydrodynamic forces and torques, respectively. Maximum loads are observed when turbines are operating in strong currents, above the rated speed of the turbine (also known as "Region III"). Consequently, this work focuses on developing a better understanding of expected turbine loads in Region III operation, which is dependent on which control strategy is implemented for power regulation. We consider overspeed control, underspeed control, and active pitch control used with rigid and passive adaptive blades, comparing loading in each scenario to inform a discussion of trade-offs.

Chapter 1 includes background information on operating regions and corresponding control objectives, active blade pitch control, and passive adaptive blade pitch control. Chapter 2 presents experimental methods used throughout Chapters 3-5, including details of the testing facility, turbine instrumentation, and non-dimensional characterization of turbine performance. Chapter 3 experimentally compares turbine loads between Region III control strategies using rigid blades, including overspeed and underspeed control and active blade pitch control. Results demonstrate the drawbacks of overspeed and underspeed control. For the former, this leads to more than double the thrust during the rated flow condition and, for the latter, a 35% increase in torque relative to the rated flow condition. Both control strategies require over-designing turbine components (blades or generator) to manage the load increases in Region III. Meanwhile, the active blade pitch controller demonstrates constant torque and large decreases in thrust in Region III. These load reduction benefits correspond to reduced component/material costs and potentially a longer lifespan for the turbine, albeit using a more complex system. The underspeed and active pitch controllers were also implemented at lower flow speeds to investigate how Reynolds number may affect the choice of controller. Results show that the relative benefit of active pitch control increases at lower Reynolds number, since Region III loads with speed control are exacerbated below Reynolds-independence while active pitch control can accommodate any variation in flow speed without increasing torque or thrust.

Prior to conducting a similar investigation to Ch. 3, but augmented with passive pitch control, we first study the effect of fiber orientation on turbine performance to inform the design of the passive pitch controller. This is one objective of Ch. 4, along with exploring appropriate scaling parameters for modeling the hydrodynamic and hydroelastic behavior of passive adaptive turbine blades. We fabricate 4 sets of bend-twist coupled blades using 0°, 2.5°, 5°, and 10° fiber orientations and test each blade set in the flume while measuring force and torque on the rotor and recording blade deformation with a high-speed camera. We observe the neutral, 0° fiber blade set shares identical C_P and C_T with rigid blades of the same geometry, while a larger ply angle results in larger reductions in C_P and C_T. Performance is more sensitive to changes in fiber orientation near 0°, with even the 2.5° fiber blades achieving appreciable load reductions at high tip-speed ratios. Chapter 4 also presents experimental results of two Cauchy-scaled flume tests using two 10° fiber blades with different stiffness, tested at two different inflow speeds. Agreement in C_T, deflection, and twist confirms that when Cauchy similarity is met, the steady-state hydrodynamic and hydroelastic behavior can be accurately modeled between scales. This outcome broadens the impact of previous lab-scale studies of passive adaptive blades and encourages future work at similar scales by increasing confidence in the experimental application of scaling laws.

Leveraging the results of Ch. 4, the objective of Chapter 5 is to experimentally implement two Region III passive pitch controllers and compare turbine loads with previously tested rigid blade control strategies to better understand trade-offs associated with each strategy.

For low-frequency load fluctuations above the turbine's rated speed, the passive adaptive blades experience no difference in measured thrust or torque on the rotor compared to the rigid blades when active pitch control is utilized. While either active pitch controller (using rigid or flexible blades) results in the largest load reductions across all tested controllers, the passive adaptive blades used with overspeed control result in reduced torque and a small 12% increase in thrust relative to loads at the rated flow condition. This encouraging result suggests that a combined strategy using overspeed and passive pitch control can be an effective method for regulating power in Region III, with only small increases in thrust while removing the need for an active pitch mechanism. This may be particularly compelling in applications where reliability is a paramount consideration.

We have demonstrated a clear advantage for implementing an active or passive blade pitch control strategy in Region III for thrust and torque. We also note, that in the experiments presented here, we increased the water velocity to 15-25% above the turbine's rated speed, while tidal sites may regularly see velocities more than 50% above the rated speed (e.g., [79]). Larger excursions would likely amplify the differences between controllers. However, active blade pitch control comes with the cost and complexity of the design and maintenance of pitch control mechanisms. While it is likely less costly than overspeed control, which increases design loads for the blades and support structures, active pitch control may be similar in cost to underspeed control which requires only a moderate increase in generator size to accommodate elevated electrical current as a consequence of higher torque. If appropriately designed, passive adaptive blade strategies may offer the largest cost reductions in both materials and maintenance. The range of flow speeds a turbine encounters will determine the benefit of pitch control relative to speed control. For example, in some river or ocean current environments, relatively limited excursions around rated speed might be anticipated, though flood and drought conditions may still impact design specifications. We also note that industrial accreditation schemes often require turbines to survive control system failures (i.e., pitch or speed control failure resulting in higher than expected thrust, torque, and/or power). Future work should evaluate the implications of control failure modes on design conditions, not just the implications under normal operating conditions.

While this thesis examined control strategies in low-frequency flow variations and their ability to reduce maximum loads, controller performance in high-frequency variations was not examined and may also influence the choice of Region III controller. The potential for active pitch controllers to respond to such high-frequency fluctuations (e.g., from turbulence, waves, shear flow, tower shadow) is dependent on frequency, maximum pitch rate and acceleration of the motors, and required power draw, among other design specifications and flow conditions. The potential for passive pitch controllers to respond to high-frequency loads is dependent on frequency, blade-to-fluid density ratio, and blade material properties.

Another factor in choice of controller is blade geometric profile and the resulting $C_P(\lambda)$ curve. In this thesis, our specific blade geometry resulted in a broad performance peak, which requires relatively large changes in tip-speed ratio to maintain constant power with a rigid blade speed controller. The exact load reductions/increases for a speed/pitch controller will depend on the blade geometry and corresponding performance curves. In applications with a narrow peak in C_P, the observed thrust loads for a rigid blade overspeed controller may be reasonable enough to consider it a viable option against active pitch control, though implementing overspeed control with passive adaptive blades would offer an opportunity to further reduce thrust and, consequently, material costs. Furthermore, broad peaks in C_P reduce the demands for Region II control.

6.2 Future Work

Our investigations of blade pitch control strategies and non-dimensional scaling of passive adaptive blades invite a number of directions for future work that are recommended to move current turbine technology further towards adoption. Opportunities for future work include:

1. *High-frequency loads*: The investigation of active and passive blade pitch control presented in this thesis is limited to low-frequency fluctuations above the turbine's rated speed. Mitigating fatigue loads is also important to increasing reliability, so a valuable

next step to this work would be to investigate the effectiveness of active and passive blade pitch control as strategies for smoothing high-frequency loads, such as the cyclic loads induced by tower shadow or shear flow. Understanding the range of frequencies either pitch control strategy can respond to would be a key development in managing fatigue loads and extending the lifespan of individual components. This would require a data acquisition system capable of time-resolved load measurements.

2. *Low- and high-frequency load trade-offs*: The active pitch controller implemented with passive adaptive blades in Ch. 5 was only tested in low-frequency load fluctuations above the turbine's rated speed. Following knowledge development around the frequency ranges suitable for active and passive blade pitch control, recommended above in (1), an assessment of this combined control strategy tested in flow with both high- and low-frequency fluctuations could provide avenues for further load reductions, considering both maximum and fatigue loads.

3. *Blockage effects*: All the experiments presented in this thesis were conducted in a recirculating flume with 35% blockage. While blockage corrections were used to inform some discussions, these corrections are not exact [59] and typically assume that C_P and C_T are independent of U_∞, which is not the case for passive adaptive blades or operation in a Reynolds-dependent regime. An assessment of blockage corrections for passive adaptive blades would be valuable for the application of lab-scale experiments, albeit difficult due to the need for access to facilities of various size to hold all non-dimensional parameters other than blockage constant.

4. *Cauchy scaling*: One recommendation for future work is made to develop confidence in the experimental application of non-dimensional scaling laws for passive adaptive blades, beyond what is presented in Ch. 4.The Cauchy-experiments used blades of the same geometric scale, but given that scaling between model and prototype typically includes different geometric scales, we recommend additional experiments that include

scaling of passive adaptive blades between lab- and field-scale systems. The completion of the field-scale axial-flow turbine by the University of Washington Applied Physics Laboratory presents a potential opportunity to conduct such an experiment. A comprehensive experiment would employ non-dimensional scaling laws to successfully model both steady-state and dynamic hydrodynamic and hydroelastic behavior.

5. *Deformation mechanisms*: Blade deformation of passive adaptive blades is rarely captured during turbine operation, making the reported deflection and twist across various flow speeds, tip-speed ratios, preset pitch angles, and ply angles a valuable contribution towards fully understanding the behavior of bend-twist coupled blades. However, to better understand the physical deformation observed here, an investigation into the chordwise and spanwise pressure distributions across passive adaptive blades during turbine operation is recommended. This would also provide a more detailed knowledge of stress concentrations across the blades under different operating conditions, which is also important to material selection and fatigue analysis.

BIBLIOGRAPHY

[1] S. Walker and P.R. Thies. “A review of component and system reliability in tidal turbine deployments”. In: *Renewable and Sustainable Energy Reviews* 151 (2021). DOI: `10.1016/j.rser.2021.111495`.

[2] H. Chen et al. “Attraction, Challenge and Current Status of Marine Current Energy”. In: *IEEE Access* 6 (2018), pp. 12665–12685. DOI: `10.1109/ACCESS.2018.2795708`.

[3] G. Godin. “On the predictability of current”. In: *The International Hydrographic Review* 60 (1983), pp. 119–126.

[4] S. Draycott et al. “Assessing extreme loads on a tidal turbine using focused wave groups in energetic currents”. In: *Renewable Energy* 135 (2019), pp. 1013–1024.

[5] S. Ordonez-Sanchez et al. “Effects of wave-current interactions on the performance of tidal stream turbines”. In: *3rd Asian Wave and Tidal Energy Conference*. Singapore, Oct. 2016.

[6] M. Arnold, F. Biskup, and P. Wen Cheng. “Load reduction potential of variable speed control approaches for fixed pitch tidal turbines”. In: *International Journal of Marine Energy* 15 (2016), pp. 175–190.

[7] A.S. Bahaj et al. “Power and thrust measurements of marine current turbines under various hydrodynamic flow conditions in a cavitation tunnel and a towing tank”. In: *Renewable Energy* 32 (2007), pp. 407–426.

[8] N. Kaufmann, T.H. Carolus, and R. Starzmann. “An enhanced and validated performance and cavitation prediction model for horizontal axis tidal turbines”. In: *International Journal of Marine Energy* 19 (2017), pp. 145–163. DOI: `10.1016/j.ijome.2017.07.003`.

[9] A. Wimshurst, C. Vogel, and R. Willden. "Cavitation limits on tidal turbine performance." In: *Ocean Engineering* 152 (2018), pp. 223–233.

[10] K.D. Van Ness et al. "Experimental comparison of speed and pitch control strategies for horizontal-axis current turbines". In: *Journal of Ocean Engineering and Marine Energy* 7 (2020), pp. 83–96.

[11] J.F. Manwell, J.G. McGowan, and A.L. Rogers. *Wind Energy Explained: Theory, Design, and Application.* Ed. by Wiley. 2002.

[12] M.S. Chowdhury et al. "Current trends and prospects of tidal energy technology". In: *Environment, Development, and Sustainability* 23 (2021), pp. 8179–8194.

[13] Z. Zhou et al. "Developments in large marine current turbine technologies - a review". In: *Renewable and Sustainable Energy Reviews* 71 (2017), pp. 852–858.

[14] Y. Gu et al. "Blade pitch system for tidal current turbines with reduced variation pitch control strategy based on tidal current velocity preview". In: *Renewable Energy* 115 (2018), pp. 149–158.

[15] B. Whitby and C.E. Ugalde-Loo. "Performance of pitch and stall regulated tidal stream turbines". In: *IEEE Transaction on Sustainable Energy* 5 (2014), pp. 64–72.

[16] J.H. Laks, L.Y. Pao, and A.D. Wright. "Control of Wind Turbine: Past, Present, Future". In: *IEEE Explore* (2009).

[17] E.A. Bossanyi, P.A. Fleming, and A.D. Wright. "Validation of Individual Pitch Control by Field Tests on Two- and Three-Bladed Wind Turbines". In: *IEEE Transactions on Control Systems Technology,* 21.4 (2013), pp. 1067–1078.

[18] M.R. Motley and R. Barber. "Passive control of marine hydrokinetic turbine blades". In: *Composite Structures* 110 (2014), pp. 133–139.

[19] Y.L. Young and M.R. Motley. "Influence of material and loading uncertainties on the hydroelastic performance of advanced material propellers". In: *Proceedings of the 2nd International Symposium on Marine Propulsors*. Hamburg, Germany, June 2011.

[20] R.F. Nicholls-Lee, S.R. Turnock, and S.W. Boyd. “Application of bend–twist coupled blades for horizontal axis tidal turbines”. In: *Renewable Energy* 50 (2013), pp. 541–550.

[21] R.E. Murray et al. “Passively adaptive tidal turbine blades: design tool development and initial verification”. In: *International Journal of Marine Energy* 14 (2016), pp. 101–114.

[22] R.B. Barber et al. “Flume-scale testing of an adaptive pitch marine hydrokinertic turbine”. In: *Composite Structures* 168 (2017), pp. 465–473.

[23] R.E. Murray et al. “Towing tank and flume testing of passively adaptive composite tidal turbine blades”. In: *Proceedings of the European Wave and Tidal Energy Conference*. Cork, Ireland, 2017.

[24] K.E. Porter et al. “Flume testing of passively adaptive composite tidal turbine blades under combined wave and current loading”. In: *Journal of Fluids and Structures* 93 (2020). DOI: `10.1016/j.jfluidstructs.2019.102825`.

[25] P. Jeffcoate et al. “Field measurements of a full scale tidal turbine”. In: *International Journal of Marine Energy* 12 (2015), pp. 3–20.

[26] A. Arredondo-Galeana et al. “Unsteady load mitigation through a passive trailing-edge flap”. In: *Journal of Fluids and Structures* 106 (2021). DOI: `10.1016/j.jfluidstructs.2021.103352`.

[27] Y.L. Young et al. “Load-dependent bend-twist coupling effects on the steady-state hydroelastic response of composite hydrofoils”. In: *Composite Structures* 189 (2018), pp. 398–418.

[28] G.A. Zarruk et al. “Experimental study of the steady fluid–structure interaction of flexible hydrofoils”. In: *Journal of Fluids and Structures* 51 (2014), pp. 326–343.

[29] H. Wada et al. “Deformation evaluation of elastic composite blade models for a tidal power generation by fluid-structure interaction analysis”. In: *Proceedings of the 18th International Conference on Composite Materials*. Jeju, Korea, Aug. 2011.

[30] G. Pisetta, R. Le Mestre, and I.M. Viola. “Morphing blades for tidal turbines: A theoretical study”. In: *Renewable Energy* 183 (2022), pp. 802–819.

[31] R.E. Murray et al. “Design of a passively adaptive rotor blade for optimized performance of a horizontal-axis tidal turbine”. In: *Proceedings of the 10th European Wave and Tidal Energy Conference*. Aalborg, Denmark, Aug. 2013.

[32] D.T. Akcabay and Y.L. Young. “Steady and dynamic hydroelastic behavior of composite lifting surfaces”. In: *Composite Structures* 227 (2019). DOI: `10.1016/j.compstruct.2019.111240`.

[33] M. Capellaro and P.W. Cheng. “An iterative method to optimize the twist angle of a wind turbine rotor blade”. In: *Wind Engineering* 38.5 (2014), pp. 489–498.

[34] S.M. Barr and J.W. Jaworksi. “Optimization of tow-steered composite wind turbine blades for static aeroelastic performance”. In: *Renewable Energy* 139 (2019), pp. 859–872. DOI: `10.1016/j.renene.2019.02.125`.

[35] C.L. Bottasso et al. “Optimization-based study of bend–twist coupled rotor blades for passive and integrated passive/active load alleviation”. In: *Wind Energy* 16.8 (2013), pp. 1149–1166.

[36] R.E. Murray, D.A. Doman, and M.J. Pegg. “Finite element modeling and effects of material uncertainties in a composite laminate with bend-twist coupling”. In: *Composite Structures* 121 (2015), pp. 362–376.

[37] C.H. Ong and S.W. Tsai. *Elastic tailoring of a composite D-spar*. Tech. rep. Report No: SAND98-1750. Sandia National Laboratories, 1998.

[38] A.T. Lee and R.G.J. Flay. “Compliant blades for passive power control of wind turbines”. In: *Wind Engineering* 24.2 (2000), pp. 3–11.

[39] D.W. Lobitz and P.S. Veers. “Load mitigation with bending/twist-coupled blades on rotors using modern control strategies”. In: *Wind Energy* 6.2 (2002), pp. 105–117.

[40] Y.L. Young. "Fluid–structure interaction analysis of flexible composite marine propellers". In: *Journal of Fluids and Structures* 24.6 (2008), pp. 799–818.

[41] S. Gowing, P. Coffin, and C. Dai. "Hydrofoil cavitation improvements with elastically coupled composite materials". In: *Proceedings of the 25th American Towing Tank Conference*. Iowa City, IA, USA, 1998.

[42] J.P. Blasques, C. Berggreen, and P. Andersen. "Hydro-elastic analysis and optimization of a composite marine propeller". In: *Marine Structures* 23.1 (2010), pp. 22–38.

[43] S.B. Heinzen, Jr. Hall C.E., and A. Gopalarathnam. "Development and testing of a passive variable-pitch propeller". In: *Journal of Aircraft* 52.3 (2015), pp. 748–763.

[44] Y.L. Young et al. "Adaptive composite marine propulsors and turbines: progress and challenges". In: *Applied Mechanics Review* 68.6 (2016). DOI: `10.1115/1.4034659`.

[45] N.M. Karaolis, P.J. Musgrove, and G. Jeronimidis. "Active and passive aerodynamic power control using asymmetric fibre reinforced laminates for wind turbine blades". In: *Proceedings of the 10th British Wind Energy Association Conference*. Ed. by D.J. Milbrow. London, England, Mar. 1988.

[46] R.M. van den Berg, P.A. Joosse, and B.J.C. Visser. "Passive power control by self twisting blades". In: *Proceedings of the European Wind Energy Association Conference and Exhibition*. Thessaloniki, Greece, Oct. 1994.

[47] D.W. Lobitz and P.S. Veers. "Aeroelastic behavior of twist-coupled HAWT blades". In: *ASME Wind Energy Symposium*. Reno, NV, USA, Jan. 1998.

[48] L. Wang, L. Xiongwei, and A. Kolios. "State of the art in the aeroelasticity of wind turbine blades: aeroelastic modelling". In: *Renewable and Sustainable Energy Reviews* 64 (2016), pp. 195–210. DOI: `10.1016/j.rser.2016.06.007`.

[49] P. Berring et al. "Torsional performance of wind turbine blades-part 1: experimental investigation". In: *Proceedings of the 16th International Conference on Composite Materials*. Kyoto, Japan, 2007.

[50] D.T. Griffith and T.D. Ashwill. *The Sandia 100-meter All-glass Baseline Wind Turbine Blade*. Tech. rep. Report No: SNL100-00. Sandia National Laboratories, 2011.

[51] F. Campagnolo, C.L. Bottasso, and P. Bettini. “Design, manufacturing and characterization of aero-elastically scaled wind turbine blades for testing active and passive load alleviation techniques within a ABL wind tunnel”. In: *Journal of Physics: Conference Series* 524 (2014).

[52] R. Starzmann et al. “A Stepwise approach towards the development and full-scale testing of a marine hydrokinetic turbine”. In: *Proceedings of the 1st Marine Energy Technology Symposium (METS13)*. Washington, D.C., Apr. 2013.

[53] G. Starzmann and P. Jeffcoate. “Field performance testing of a floating tidal energy platform - part 1: power performance”. In: *Proceedings of the 4th Asian Wave and Tidal Energy Conference*. Taipei, Taiwan, 2018.

[54] R.E. Murray et al. “Towing tank testing of passively adaptive composite tidal turbine blades and comparison to design tool”. In: *Renewable Energy* 121 (2018), pp. 362–376.

[55] A. Copping et al. “Maritime renewable energy markets: Power from the sea”. In: *Maritime Technology Society Journal* 52.5 (2018), pp. 99–109.

[56] D. Forbush, R. Cavagnaro, and B. Polagye. “Power-tracking control for cross-flow turbines”. In: *Journal of Renewable and Sustainable Energy* 11 (2019).

[57] B. Gaurier et al. “Tidal energy “Round Robin” tests comparisons between towing tank and circulating tank results”. In: *International Journal of Marine Energy* 12 (2015), pp. 87–109.

[58] C. Garrett and P. Cummins. “The efficiency of a turbine in a tidal channel”. In: *Journal of Fluid Mechanics* 588 (2007), pp. 243–251.

[59] H. Ross and B. Polagye. “An experimental assessment of analytical blockage corrections for turbines”. In: *Renewable Energy* 152 (2020), pp. 1328–1341.

[60] J.I. Whelan, J.M.R. Graham, and J. Peiro. “A free-surface and blockage correction for tidal turbines”. In: *Journal of Fluid Mechanics* 624 (2009), pp. 281–291.

[61] M.J. Barnsley and J.F. Wellicome. *Final Report on the 2nd phase of development and testing of a horizontal axis wind turbine test rig for the investigation of stall regulation aerodynamics*. Tech. rep. Technical report E.5A/CON5103/1746. 1990.

[62] G.T. Houlsby, S. Draper, and M.L.G. Oldfield. *Application of linear momentum actuator disc theory to open channel flow*. Tech. rep. No. OUEL 2296/08. University of Oxford, 2008.

[63] P. Mycek et al. “Experimental study of the turbulence intensity effects on marine current turbines behaviour. Part 1: One single turbine”. In: *Renewable Energy* 66 (2014), pp. 729–746.

[64] I.A. Milne et al. “The characterization of the hydrodynamic loads on tidal turbines due to turbulence”. In: *Renewable and Sustainable Energy Reviews* 56 (2016), pp. 851–864. DOI: `10.1016/j.rser.2015.11.095`.

[65] B. Gunawan, V.S. Neary, and J. Colby. “Tidal energy site resource assessment in the East River tidal strait, near Roosevelt Island, New York, New York”. In: *Renewable Energy* 71 (2014), pp. 509–517. DOI: `10.1016/j.renene.2014.06.002`.

[66] J. Thomson et al. “Measurements of Turbulence at Two Tidal Energy Sites in Puget Sound, WA”. In: *IEEE Journal of Oceanic Engineering* 37.3 (2012), pp. 363–374.

[67] A. Mason-Jones et al. “Non-dimensional scaling of tidal stream turbines”. In: *Energy* 44.1 (2012), pp. 820–829. DOI: `10.1016/j.energy.2012.05.010`.

[68] C.L. Bottasso, F. Campagnolo, and V. Petrovic. “Wind tunnel testing of scaled wind turbine models: Beyond aerodynamics”. In: *Journal of Wind Engineering and Industrial Aerodynamics* 127 (2014), pp. 11–28.

[69] P.P. Friedmann. “Aeroelastic scaling for rotary-wing aircraft with applications”. In: *Journal of Fluids and Structures* 19.5 (2004), pp. 635–650.

[70] C.H. Wolowicz, J.S. Bowman, and Jr. Gilbert W.P. *Similitude requirements and scaling relationships as applied to model testing.* Tech. rep. Technical Paper 1435. NASA, 1979.

[71] Z. Wan and C.E.S. Cesnik. "Geometrically nonlinear aeroelastic scaling for very flexible aircraft". In: *AIAA Journal* 52.10 (2014). DOI: `10.2514/1.J052855`.

[72] S.K. Chakrabarti. *The Theory and Practice of Hydrodynamics and Vibration.* World Scientific, 2002, pp. 144–146.

[73] S.A. Hughes. *Physical models and laboratory techniques in coastal engineering.* World Scientific, 1993.

[74] M.R. Motley and Y.L. Young. "Scaling of the Transient Hydroelastic Response and Failure Mechanisms of Self-Adaptive Composite Marine Propellers". In: *Internation Journal of Rotating Machinery* 2012 (2012). DOI: `10.1155/2012/632856`.

[75] Y.L. Young et al. "Ventilation of lifting bodies: Review of the physics and discussion of scaling effects". In: *Applied Mechanics Reviews* 69.1 (2017). DOI: `10.1115/1.4035360`.

[76] Y.L. Young. "Dynamic hydroelastic scaling of self-adaptive composite marine rotors". In: *Composite Structures* 92 (2010), pp. 96–106.

[77] G.W. Ng et al. "Scaling the dynamic response and stability of composite hydrodynamic lifting surfaces". In: *Composite Structures* 285 (2022). DOI: `10.1016/j.compstruct.2021.115148`.

[78] K. Cox and A. Echtermeyer. "Structural design and analysis of a 10MW wind turbine blade". In: *Energy Procedia* 25 (2012), pp. 194–201.

[79] M. Lewis et al. "Power variability of tidal-stream energy and implications for electricity supply". In: *Energy* 183 (2019), pp. 1061–1074.

[80] J.R. Vinson and R.L. Sierakowski. *The Behavior of Structures Composed of Composite Materials.* Kluwer Academic Publishers, 2008.

Appendix A

PERFORMANCE CONTOUR MAPS

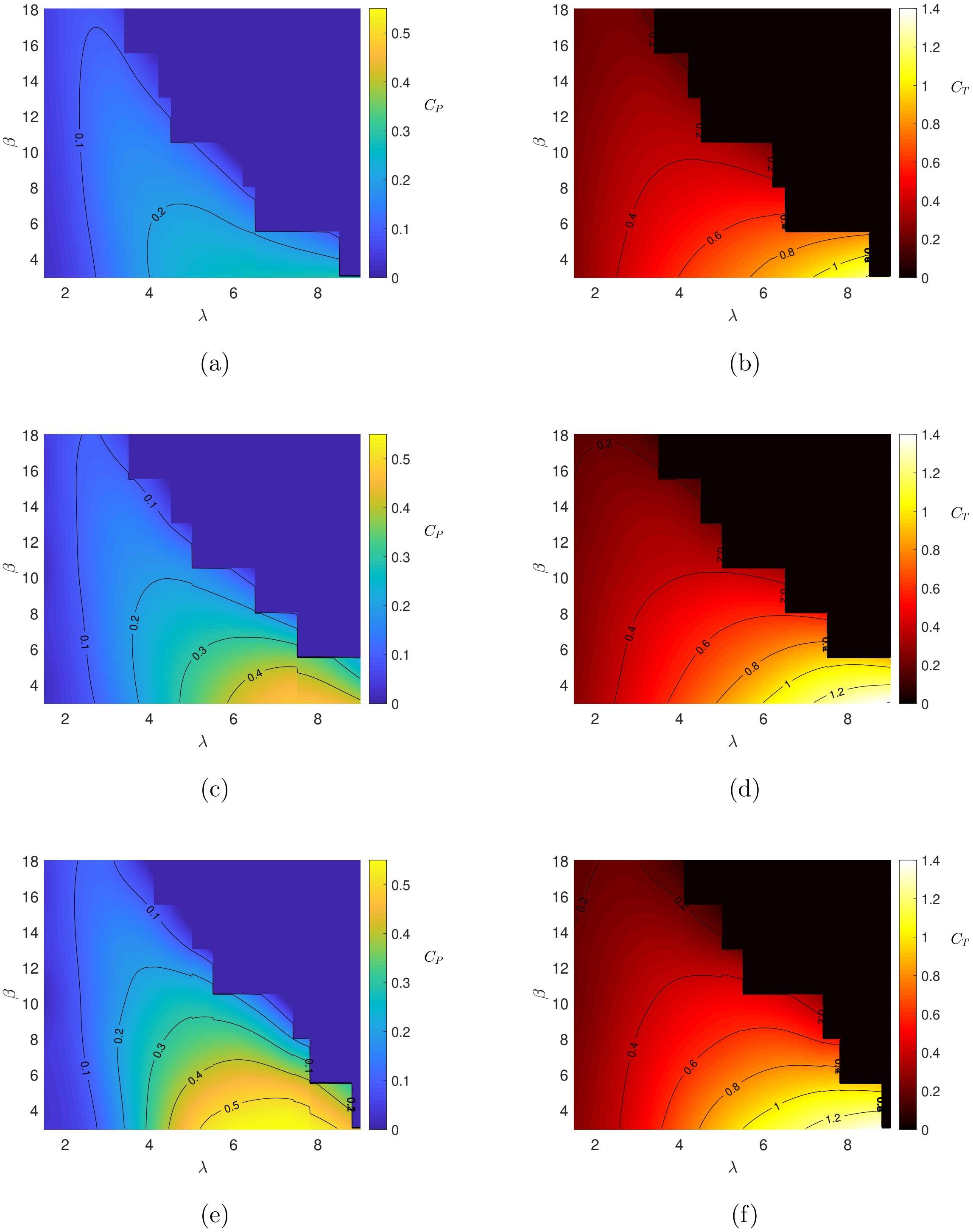

(a) (b) (c) (d) (e) (f)

Figure A.1: C_P (left column) and C_T (right column) contour maps as a function of tip-speed ratio (λ) and blade pitch (β) in (a,b) 0.4 m/s flow, (c,d) 0.5 m/s flow, and (e,f) 0.6 m/s flow.

Appendix B

STEP-BY-STEP BLADE FABRICATION

The blade fabrication steps were as follows:

1. Seven 76x178-mm plies were cut from Hexcel AS4, 12K filament count carbon fiber using a 2D CNC fabric cutter (Autometrix Advantage) to achieve a precise and repeatable fiber orientation of 5° for each ply. A larger or smaller bend-twist coupling could be achieved by increasing or decreasing the fiber angle orientation during this step.

2. The plies were laid up on a curved, CNC-machined, aluminum mold that follows the chord line of the blade (Fig. B.1a). Plies were cured in an autoclave using the cure cycle provided by Hexcel for the epoxy matrix (HexPly 8552).

3. Mounted on a CNC-machined wooden block of the same curvature, the spar profile was cut from the cured carbon fiber slab using a water jet (FLOW Industries) to produce precise and repeatable spar geometry (Figure B.1b). The spar shape was smaller than the final blade outline to prevent the carbon fiber from protruding through the leading and trailing edge where blade thickness was smaller than the thickness of the carbon fiber spar.

4. A blade root adaptor, used for mounting the blade to the turbine rotor, was 3D printed in titanium (Figure B.1c). The threaded hole for the set screw was drilled and tapped by hand after the print. Titanium was chosen over aluminum or steel to avoid galvanic corrosion with the carbon fiber. The carbon fiber spar was fixed to the blade root adaptor with an epoxy adhesive (Fig. B.1d).

5. An aluminum blade mold was CNC machined with the desired blade geometry and two cavities for filling the mold and venting air. A threaded rod in the end cap of the mold aligned the root adaptor and spar with the blade profile of the mold so the spar was repeatably centered along the chord line (Figure B.1e). After spraying the mold with a mold release (Ease Release 200, Mann Release Technologies), a two-part semi-rigid polyurethane (Smooth-cast 45D) was mixed and degassed before filling the mold. The polyurethane was allowed to cure under pressure (85psi) in an autoclave to minimize air bubbles and surface defects.

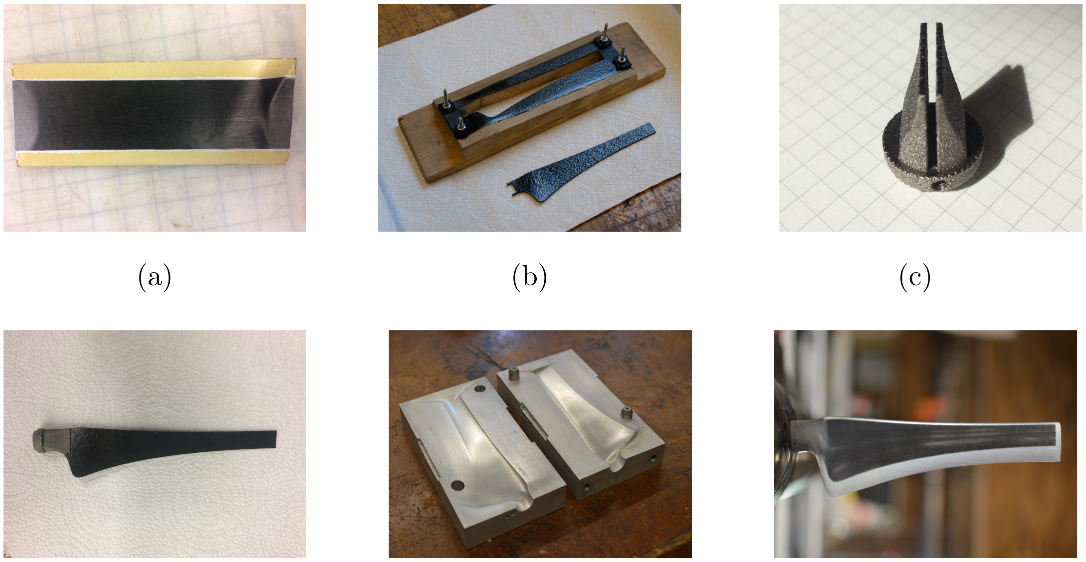

(a) (b) (c)

(d) (e) (f)

Figure B.1: Various steps of blade fabrication including the (a) layup of 7 plies (76mm by 178mm) of Hexcel AS4, 12K filament count carbon fiber onto a mold surface to be cured in an autoclave, (b) spar profile cut from the water jet, (c) titanium blade root adaptor to hold the carbon fiber spar, (d) spare mounted in the blade root, (e) aluminum blade mold to cast the spar in polyurethane, and (f) final composite blade consisting of a carbon fiber spar with a titanium root cast in polyurethane. The carbon fiber provides the desired bend-twist coupling while the polyurethane provides the desired blade geometry.

Discussed in Sec. 5.3.5, we identified four potential sources of blade-to-blade variation in the fabrication process, where items 1-3 affect the bend-twist coupling of the blade and item 4 affects turbine efficiency:

1. Error in fiber angle orientation during the layup of each ply. Since 7 plies were used for the layup, this does allow for some variation in the application of each ply to average out within a single blade.

2. Error in spar alignment in the titanium blade root. Since the spar is manually fixed to the blade root with epoxy, imperfect alignment of the spar tabs with the edges of the blade root would shift the spar closer or further from the leading edge of the blade.

3. Error in spar alignment in the casting mold . While a set screw in the end cap of the mold was meant to align the spar in the center of the blade during casting, there was noticeable slack that meant the spar could be shifted chordwise or flapwise during the pour (Fig. 5.6).

4. Surface deformations during casting. Slight surface blemishes (uneven finish, small air bubbles) were difficult to avoid entirely and vary between blades. Casting under pressure mitigated surface defects but did not eliminate them entirely.

Appendix C

COMPOSITE BLADE GEOMETRY

Table C.1: Blade geometry, where r is the local radius, R is the turbine radius, c is the local chord, and t is the local thickness.

r/R	c/r	t/c	Pre-Twist(°)
0.244	0.318	1.000	14.60
0.262	0.303	1.000	14.60
0.300	0.271	0.963	14.60
0.330	0.484	0.350	14.56
0.355	0.554	0.223	14.02
0.381	0.499	0.208	13.01
0.410	0.438	0.201	11.46
0.441	0.385	0.193	10.03
0.474	0.334	0.185	9.32
0.510	0.288	0.177	8.48
0.548	0.247	0.167	7.81
0.590	0.212	0.167	7.05
0.635	0.183	0.159	6.25
0.684	0.159	0.147	5.69
0.736	0.140	0.147	5.21
0.790	0.126	0.148	4.66
0.902	0.106	0.149	3.66
0.959	0.100	0.150	3.17
1.000	0.096	0.154	3.31

Appendix D

STATIC MECHANICAL TESTING

A static load test was conducted to experimentally determine bend (δ) and twist ($\Delta\phi$) of the blade tip in response to applied loads. Figure D.1 shows the configuration for the benchtop test. An actuator, positioned at the quarter-chord near the blade tip, deflected the blade while a six-axis load cell (Nano25, ATI Industrial Automation) at the blade root measured the reaction force. A laser displacement sensor (optoncdt 2300-20, Micro-Epsilon) aligned with the actuator measured deflection of the quarter-chord at the blade tip. Ten discrete displacements over 15 mm were applied by the actuator to estimate a best fit bending stiffness.

The first laser displacement sensor was used in combination with a second (optoncdt 1700-500, Micro-Epsilon) to measure twist at the blade tip during deflection. The first remained positioned at the quarter-chord and the second was positioned 63.5 mm aft of the quarter chord. Both laser displacement sensors register the laser beam reflection off of a cross-beam attached to the blade tip, parallel to the chord, that provides an opaque surface for better reflection and lower uncertainty in twist measurements. The difference between the laser readings was used to calculate $\Delta\phi$:

$$\Delta\phi = \tan^{-1}(d/x), \tag{D.1}$$

where d and x are described in Fig. D.1. Results from the mechanical tests with each blade set are shown in Fig. D.2.

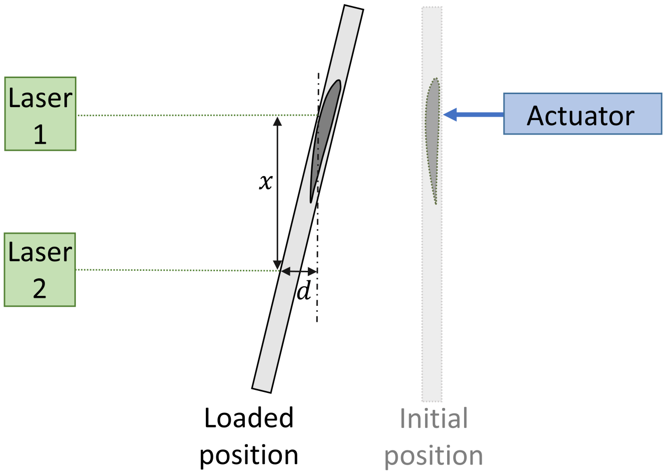

Figure D.1: Top-view schematic of the static mechanical test, where x is the distance between the laser displacement sensors (63.5 mm) and d is the difference between the displacement measurements. The load applied by the actuator is measured by a load cell at the blade root.

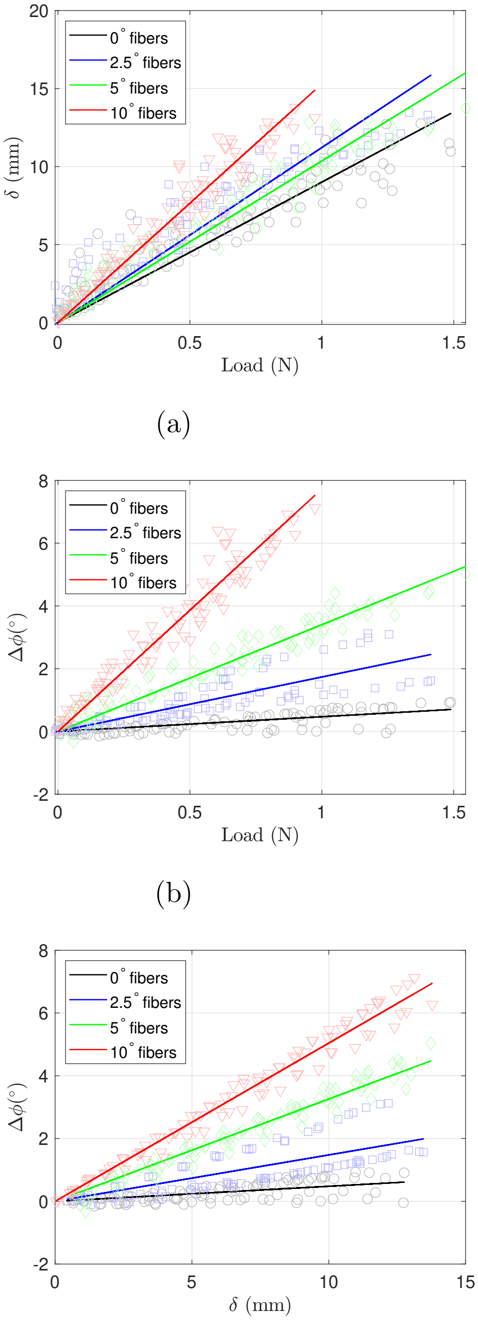

(a)

(b)

(c)

Figure D.2: (a) Deflection and (b) twist as a function of applied load for passive adaptive blades with 0°, 2.5°, 5°, and 10° fiber orientation. The resulting bend-twist coupling is reflected in (c) twist as a function of deflection.

Appendix E

CALCULATION OF BENDING STIFFNESS MATRIX AND BEND-TWIST COUPLING

According to classical lamination theory [80], the stiffness matrix, Q, of the carbon fiber was calculated:

$$Q = \begin{bmatrix} \frac{E_1^2}{E_1-\nu_{12}^2 E_2} & \frac{\nu_{12}E_1E_2}{E_1-\nu_{12}^2 E_2} & 0 \\ \frac{E_1E_2}{E_1-\nu_{12}^2 E_2} & \frac{E_1E_2}{E_1-\nu_{12}^2 E_2} & 0 \\ 0 & 0 & G_{12} \end{bmatrix} \tag{E.1}$$

The stiffness matrix for each ply, $\bar{Q}$, was calculated from Eqn.E.1 and the fiber angle orientation, 10°:

$$\overline{Q} = \begin{bmatrix} \overline{Q}_{11} & \overline{Q}_{12} & \overline{Q}_{16} \\ \overline{Q}_{21} & \overline{Q}_{22} & \overline{Q}_{26} \\ \overline{Q}_{61} & \overline{Q}_{62} & \overline{Q}_{66} \end{bmatrix} \tag{E.2}$$

where the elements of $\overline{Q}$ are as follows:

$$\overline{Q}_{11} = Q_{11}\cos^4\theta + 2(Q_{12}+2Q_{66})\cos^2\theta\sin^2\theta + Q_{22}\sin^4\theta \tag{E.3}$$

$$\overline{Q}_{12} = Q_{12}\cos^4\theta + \sin^4\theta + (Q_{11}+Q_{22}-4Q_{66})\cos^2\theta\sin^2\theta \tag{E.4}$$

$$\overline{Q}_{16} = (Q_{11}-Q_{12}-2Q_{66})\cos^3\theta\sin\theta - (Q_{22}-Q_{12}-2Q_{66})\cos\theta\sin^3\theta \tag{E.5}$$

$$\overline{Q}_{21} = Q_{12}(\cos^4\theta + \sin^4\theta) + (Q_{11}+Q_{22}-4Q_{66})\cos^2\theta\sin^2\theta \tag{E.6}$$

$$\overline{Q}_{22} = Q_{11}\sin^4\theta + 2(Q_{12}+2Q_{66})\cos^2\theta\sin^2\theta + Q_{22}\cos^4\theta \tag{E.7}$$

$$\overline{Q}_{26} = (Q_{11}-Q_{12}-2Q_{66})\cos\theta\sin^3\theta - (Q_{22}-Q_{12}-2Q_{66})\cos^3 theta\sin\theta \tag{E.8}$$

$$\overline{Q}_{61} = (Q_{11}-Q_{12}-2Q_{66})\cos^3\theta\sin\theta - (Q_{22}-Q_{12}-2Q_{66})\cos\theta\sin^3\theta \tag{E.9}$$

$$\overline{Q}_{62} = (Q_{11}-Q_{12}-2Q_{66})\cos\theta\sin^3\theta - (Q_{22}-Q_{12}-2Q_{66})\cos^3 theta\sin\theta \tag{E.10}$$

$$\overline{Q}_{66} = (Q_{11} + Q_{22} - 2Q_{12} - 2Q_{66})\cos^2\theta\sin^2\theta + Q_{66}(\cos^4\theta + \sin^4\theta) \tag{E.11}$$

Note the stiffness matrix for each ply is identical since the layup is unidirectional. Finally, the bending stiffness matrix, D, was calculated using the position and thickness of each ply and Eqn. E.2

$$D_{ij} = \frac{1}{3}\sum_{k=1}^{n} \overline{Q}_{ij_k}(z_k^3 - z_{k-1}^3) \tag{E.12}$$

where k corresponds to each ply in the layup and z is the distance from the center of the ply to the centerline of the stack. The bending stiffness of the carbon fiber spar can then be determined from matrix D

$$EI = D_{11} - \frac{D_{12}^2}{D_{22}} \tag{E.13}$$

and was used to determine ply count in the second blade fabrication for the Cauchy-scaling experiments.

Furthermore, the bend-twist coupling parameter, α, can be computed from matrix $\overline{Q}$ since the stack is unidirectional [37]:

$$\alpha = \frac{-\overline{Q}_{16}}{\sqrt{\overline{Q}_{11}\overline{Q}_{66}}}; \tag{E.14}$$

This results in a calculated bend-twist coupling parameter for the 0°, 2.5°, 5°, and 10° fiber blades of 0, -0.187, -0.352, and -0.587.

Appendix F

COMPARISON OF RIGID, ALUMINUM BLADES WITH NEUTRAL, COMPOSITE BLADES

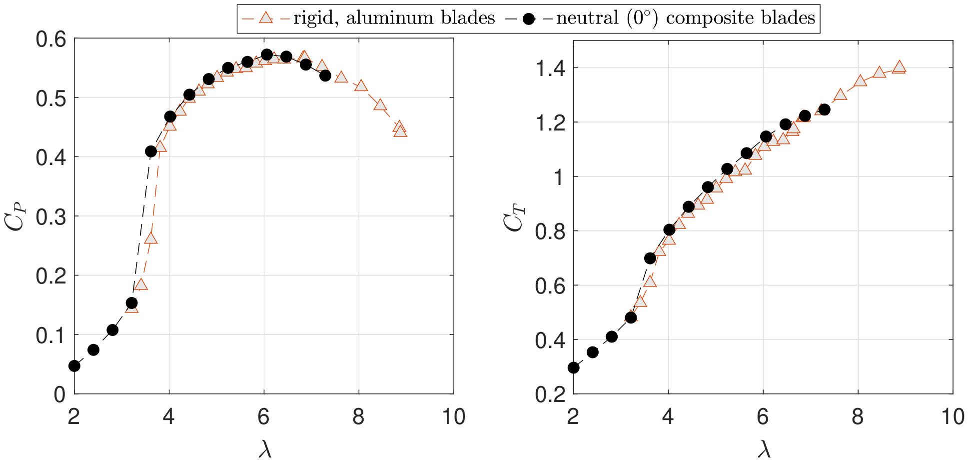

Figure F.1: Coefficients of (a) power and (b) thrust for the rigid, aluminum blades and neutral (0°), composite blades.